VNIVERSITAT DE VALÈNCIA

DEPARTAMENT DE FÍSICA APLICADA I ELECTROMAGNETISME

Programa de doctorado en Física 3126 RD 99/2011

Tesis para el título de doctor por la Universitat de València

---

1.5 μm ultrafast fiber lasers of repetition rates from single shot to GHz range

---

Autor:
Héctor Muñoz Marco

Director:
Dr. Pere Pérez Millán

Tutor Académico:
Dr. Antonio Díez Cremades

Julio, 2021

Declaration of Authorship / Declaración de Autoría

El Dr. Pere Pérez Millán, CTO de la empresa FYLA LASER S.L. como director de la tesis y el Dr. Antonio Díez Cremades, catedrático del Departamento de Física Aplicada y Electromagnetismo de la Universitat de València como tutor académico, informan de que la presente memoria titulada "1.5 μm ultrafast fiber lasers of repetition rates from single shot to GHz range", ha sido realizada bajo nuestra dirección y tutorización en la empresa FYLA LASER S.L. por Héctor Muñoz Marco y constituye su Tesis para optar al título de Doctor por la Universidad de Valencia, una vez cursados los estudios en el Doctorado en Física.

"Work is to find out for yourself and discover it by yourself."

Oda Nobunaga

Contents

UNIVERSIDAD DE VALENCIA

Abstract

Departmento de física aplicada y electromagnetismo de la Universidad de Valencia

Doctor por la Universitat de València

1.5 μm ultrafast fiber lasers of repetition rates from single shot to GHz range

by Héctor Muñoz-Marco

This thesis focuses on the theoretical and experimental study of the passive mode locking method based on semiconductor saturable absorber mirrors (SESAM). This method is used to develop lasers of ultra-short pulsed emission (pulse duration from femtosconds to few picoseconds) in the 1.5 μm band that cover a wide range of scientific and industrial applications. The application requirements in terms of repetition rate are diverse for this type of lasers. Low repetition rates from single shot to several kilohertz are used in sample analysis applications where response times are in the order of milliseconds, such as the two photon absorption transient current technique. Mid repetition rates from megahertz to few hundreds of megahertz are typically used in supercontinuum generation, terahertz waves generation, multi-photon microscopy and ultrafast spectroscopy. High repetition rates, above one gigahertz, are required in optical communication applications such as photonic radar, photonic analog-to-digital conversion, and wireless photonic communication. In this thesis, architectures have been developed that allow covering the entire range of repetition rates, from single shot to gigahertz.

The first part of the thesis is dedicated to developing the mathematical model based on the Non-Linear-Schrödinger Equation that has been used in the design phase of the lasers and its numerical implementation through the Split-Step Fourier method. This model includes fiber pulse propagation, gain equation for erbium emission active media and semiconductor saturable mirror operation.

Next, the theoretical model is adapted to design GHz range passively mode-locked fiber lasers. The modeled cavities of the lasers are configured by a highly doped and polarization- maintaining single fiber of a single type. For different pulse repetition rates, ranging from one GHz to ten GHz, gain parameters and pump threshold for a stable mode-locked laser emission are studied. Pulse time width, spectral width and SESAM properties are defined to achieve stable emission. To experimentally validate the theoretical model, 1.0 GHz and 2.2 GHz laser cavities have been built up and

amplified. A stable and robust operation for both frequencies was obtained and the experimental measurements have been found to match the theoretical predictions. Enhanced environmental stability has been achieved using a cavity temperature control system and an antivibration enclosure, ending in a robust and marketable prototype.

Finally the thesis addresses the design and development of low repetition rate ultrafast fiber lasers from single shot to tens of megahertz. In particular, a system developed to fulfil the specific optical excitation requirements of the Two-Photon Absorption Transient Current Technique, TPA-TCT, is described. This technique is used for localized characterization of radiation semiconductor detectors. The system is composed of three modules: a pulsed laser source, a pulse management module and a dispersion management module. Such modules are designed to provide the following configurability of the properties of the pulsed signal delivered at the output of the complete system: variation of the pulse energy between 10 nJ and 0.1 pJ, variation of the pulse repetition rate from 8.0 MHz to single shot and variation of the pulse duration between 300 and 600 fs. Besides, the system provides analysis elements such as reference signals, real-time measurement of pulse repetition rate and energy, autocorrelation of the pulse in the sample plane and electro-mechanic commutation of the pulsed signal with response time below 2 ms. Finally, the validity of the system as excitation source in the TPA-TCT is demonstrated by measuring spatially resolved excited electric charge in a semiconductor charge.

Resumen

Esta tesis se centra en el estudio teórico y experimental del método de bloqueo de modos pasivo basado en espejos absorbentes saturables de semiconductor (SESAM). Este método se utiliza para desarrollar láseres de emisión pulsada ultracorta (duración de pulso desde femtosegundos hasta unos pocos picosegundos) en la banda de 1,5 μm que cubren una amplia gama de aplicaciones científicas e industriales. Los requisitos de frecuencia de repetición de pulsos son diversos para este tipo de láseres, en función de su aplicación. Bajas frecuencias de repetición, desde un solo disparo hasta varios kilohercios, se utilizan en aplicaciones de análisis de muestras donde los tiempos de respuesta son del orden de milisegundos, como la técnica de corriente transitoria de absorción de dos fotones. Frecuencias de repetición medias, desde megahercios hasta unos pocos cientos de megahercios, se utilizan típicamente en la generación de supercontinuo, generación de ondas de terahercios, microscopía multifotón y espectroscopía ultrarrápida. Finalmente, se requieren altas frecuencias de repetición, por encima del gigahercio, en aplicaciones de comunicación óptica como el radar fotónico, la conversión fotónica analógica a digital y la comunicación fotónica inalámbrica. En esta tesis se han desarrollado arquitecturas que permiten cubrir todo el rango de frecuencias de repetición, desde un solo disparo hasta gigahercios. Está estructurada en cinco capítulos. El primero, es una introducción que pone en contexto la investigación a través de un breve análisis del estado del arte. El segundo capítulo recoge los conceptos que se han utilizado para elaborar el modelo teórico que permite simular cavidades láser con el fin de diseñar osciladores que proporcionen los pulsos deseados con una estructura de bloqueo de modos. Los capítulos tercero y cuarto recogen las dos principales arquitecturas láser desarrolladas a lo largo de esta tesis: láseres de frecuencias de repetición en el rango de los gigahercios (capítulo tres) y láseres de frecuencia de repetición desde disparo único a decenas de megahercios (capítulo cuatro). Finalmente, el capítulo cinco habla de la proyección futura de la investigación realizada

en este trabajo. La tesis ha sido llevada a cabo en el marco de un doctorado industrial en la empresa FYLA LASER S.L., dando como resultado prototipos láser que han sido, posteriormente, comercializados como productos de vanguardia tecnológica.

La óptica ultrarrápida ha sido un campo de investigación en auge durante las últimas décadas y, en la actualidad, los sistemas láser de pulso ultracorto presentan numerosas aplicaciones en áreas de investigación fundamental, así como en medicina e industria. Los sistemas láser ultrarrápidos se utilizan para estudios de resolución temporal en química, metrología de frecuencia óptica, generación de terahercios, espectroscopía, microscopía no lineal, tomografía óptica de coherencia, técnicas de corriente transitoria de absorción de fotones, conversión fotónica de analógico a digital y comunicaciones inalámbricas fotónicas. Ejemplos de aplicación relacionada con la medicina son la cirugía ocular con láser y los taladros dentales. Por otro lado, en la industria, los láseres ultrarrápidos se utilizan para micromecanizado y marcado. La piedra angular de la óptica ultrarrápida es el láser de bloqueo de modos. A lo largo de las dos últimas décadas, el desarrollo de estos láseres ha sido un área de investigación en sí misma.

Tradicionalmente, los láseres de estado sólido de bloqueo de modos (láseres basados en cristales no lineales como los láseres de titanio zafiro (Ti:Sapphire) o los de cristal de granate de aluminio de itrio dopado con neodimio (Nd:Yag)) han dominado el mercado. Sin embargo, este tipo de láser requiere entornos estables de laboratorio con mesas ópticas que minimicen las vibraciones y temperatura ambiente estabilizada. Además, los láseres de estado sólido tienen un alto consumo de energía y, a menudo, precisan un mantenimiento costoso. Para que la óptica ultrarrápida gane terreno en mercados comerciales mucho más amplios y pueda ser industrializada, es necesario encontrar soluciones a estas limitaciones.

En comparación con los láseres de gas y de estado sólido, los láseres de fibra óptica son más compactos dado que las fibras ópticas se pueden doblar y enrollar fácilmente. El potencial de fabricar sistemas láser compactos

y resistentes con bajo consumo de energía a un precio relativamente asequible hace que los láseres de fibra óptica amplificados sean una alternativa muy prometedora a los láseres de estado sólido clásicos.

Las propiedades clave que hacen que las fibras dopadas de tierras raras sean atractivas como medios activos láser son: la elevada ganancia del medio activo debido a la sencillez de obtener un medio activo muy largo, el amplio ancho de banda de los espectros de emisión y absorción y la excelente calidad de haz. En los láseres de fibra óptica de bloqueo de modos, el medio activo es el núcleo de una fibra óptica dopada con iones de elementos de tierras raras. Dichos elementos (iones) son típicamente erbio (Er^{3+}), neodimio (Nd^{3+}), iterbio (Yb^{3+}), tulio (Th^{3+}) o praseodimio (Pr^{3+}).

En esta tesis, se estudian láseres cuyo medio activo se basa en fibra dopada con erbio, y en fibra co-dopada con erbio e iterbio. Los medios activos de láser de fibra pueden bombearse directamente mediante diodos láser de onda continua. El enorme progreso y desarrollo tecnológico de los láseres de diodo de alta potencia ofrece una ventaja competitiva en comparación con los láseres de estado sólido clásicos. En un sentido amplio, un láser de fibra es capaz de convertir la salida de baja calidad de un diodo láser de bombeo de onda continua en una luz temporal y espacialmente coherente de alta intensidad. Además, la salida del láser de fibra puede tomar varios formatos temporales, según el régimen de operación: Q-switch, onda continua o bloqueo de modos, siendo este último el régimen objeto de estudio en esta tesis.

El bloqueo de modo de un láser se refiere al bloqueo de las relaciones de fase entre muchos modos longitudinales vecinos de la cavidad láser. El bloqueo de tales relaciones de fase permite una variación periódica de la potencia de salida del láser que es estable en el tiempo y tiene una periodicidad dada por el tiempo de ida y vuelta en la cavidad. Si se bloquean un número considerable de modos longitudinales individuales de forma que sus diferencias de fase sean suficientemente pequeñas, se produce un pulso corto que puede tener una potencia de pico significativamente mayor

que la potencia media del láser. El origen del bloqueo de modos se comprende mejor en el dominio del tiempo. Un láser en estado estable es un sistema de retroalimentación, donde la ganancia de la señal óptica en el medio activo por viaje de ida y vuelta se equilibra con las pérdidas. Si se introduce en la cavidad un elemento que produce una mayor pérdida a menores potencias, el láser puede favorecer una superposición de modos longitudinales correspondientes a un pulso corto con alta potencia pico. Otro requisito para obtener un bloqueo de modos estable es que el pulso se reproduzca después de un viaje de ida y vuelta (dentro de un desplazamiento de fase total en todos los modos longitudinales). Las relaciones de fase entre los diferentes modos se ven afectadas por efectos como la dispersión, la ganancia de ancho de banda y los cambios de fase no lineales. Aunque se puede construir un número infinito de pulsos distintos como diferentes superposiciones de modos longitudinales, generalmente solo un pulso único especificado por su forma, duración, potencia máxima y fase es una solución estable de la cavidad y, por lo tanto, se pueden diseñar las características del pulso de salida controlando y adaptando los parámetros físicos de los elementos láser que los comprenden. Existen varios mecanismos, tanto activos como pasivos, para conseguir que los modos en la cavidad entren en fase y se produzca el bloqueo. Concretamente, en esta tesis se estudian láseres de bloqueo de modo pasivo basados en espejos absorbentes saturables de semiconductor (SESAM) como elemento de bloqueo de modos.

Ratios de repetición en el rango de los Gigahercios

Los láseres pulsados de femtosegundos y picosegundos con altas tasas de repetición (centenares de megahercios a decenas de gigahercios) son de interés en diferentes aplicaciones. Algunas de ellas son: conversión analógica-digital asistida por fotones (PADC), espectroscopía ultrarrápida, biomedicina óptica y comunicaciones de ultra alto ancho de banda en multiplexación por división de longitud de onda. En referencia a los PADC, se sabe desde la década de 1970 que se pueden usar pulsos ópticos cortos

(de duración $< 100\ ps$) para mejorar la velocidad de los interruptores de muestreo electrónicos a través de un diseño optoelectrónico. El pulso óptico proporciona una fluctuación pulso a pulso más baja que la electrónica y tiempos de subida más rápidos. Los láseres disponibles actualmente capaces de ofrecer tasas de repetición de pulsos en el rango de GHz no son muy robustos y proporcionan señales de baja calidad. Esto ha hecho imposible la implementación de sistemas PADC confiables, que ahora es una posibilidad abierta debido al tipo de láser presentado en esta tesis. Una solución interesante para obtener altas tasas de repetición en una configuración de modo bloqueado es utilizar cavidades lineales de Fabry-Pérot. Uno de los parámetros más importantes cuando se hace referencia a los peines láser basados en tecnología de bloqueo de modos en PADC es su estabilidad a largo plazo. Aunque se han logrado osciladores Fabry-Pérot de un gigahercio, el umbral de daño térmico del espejo absorbente saturable basado en semiconductor (SESAM) se alcanza produciendo un daño progresivo en la superficie del SESAM y eventualmente cambiando las propiedades del láser. En este punto, surge la necesidad de un modelo teórico para estudiar cavidades de láser de fibra de bloqueo de modos pasivo a frecuencias de GHz.

En esta tesis doctoral se ha desarrollado un modelo teórico basado en la Ecuación de Schrödinger No Lineal (NLSE). Se han estudiado diferentes frecuencias de repetición cambiando la longitud total de la cavidad (1.0 GHz, 2.2 GHz, 5.0 GHz y 10.0 GHz). Algunos de los parámetros clave caracterizados para cada una de las frecuencias estudiadas son el umbral de potencia del bombeo de onda continua y las condiciones de ganancia para que se produzca la emisión de pulsos en régimen de bloqueo de modos estable. Además, también han sido incluidas en el modelo teórico las propiedades del absorbente saturable (tiempo de relajación, fluencia, absorbancia y longitud de onda de reflexión) que influyen directamente en la duración del pulso y su ancho espectral. La cavidad del oscilador se ha modelado utilizando una única fibra especialmente seleccionada para absorber la potencia de la señal óptica de bombeo de onda continua y la

luz láser que llega al SESAM, lo que le permite trabajar por debajo de su umbral de daño térmico, $< 1\ mJ/cm^2$. Para alcanzar los valores de absorción requeridos de cientos de decibelios por metro (dB/m), se ha utilizado una fibra codopada con erbio e iterbio que también proporciona las propiedades de dispersión necesarias para generar una solución solitónica de la ecuación de Schrödinger no lineal. Teniendo en cuenta todos estos parámetros, se ha conseguido modelizar una emisión de bloqueo de modos estable.

Además, todas las etapas láser (bombeo y cavidad) tienen una configuración mantenedora de polarización (PM) compacta que, correctamente alineada, hace que el láser funcione en un régimen de polarización lineal, mejorando la estabilidad debido a la inexistencia de acoplamiento entre modos de polarización. Los láseres de fibra de 2 GHz y las cavidades con frecuencias superiores a 10 GHz se lograron anteriormente utilizando arquitecturas complejas o fibras ópticas especialmente diseñadas. Sin embargo, en esta tesis, el enfoque es obtener láseres de fibra de GHz optimizados, robustos, compactos y repetibles utilizando componentes comerciales. Al integrar láseres de fibra de modo bloqueado en aplicaciones prácticas como PADC, es necesario garantizar la estabilidad a largo plazo de la fuente láser en un entorno de condiciones no controladas (es decir, en un entorno de no laboratorio). Para confirmar experimentalmente la fiabilidad del modelo, se han conseguido fuentes de luz pulsadas robustas, estables y ultracortas para 1.0 y 2.2 GHz. Finalmente, se ha desarrollado un diseño mecánico para mejorar la estabilidad ambiental del láser, introduciendo un sistema de control de temperatura de la cavidad y un encofrado anti-vibratorio.

Frecuencias de repetición desde disparo único a decenas de Megahercios

Los láseres de femtosegundos de bajas frecuencias de repetición de pulsos, desde un solo disparo hasta decenas de megahercios, se utilizan en aplicaciones de inspección, como la técnica de corriente transitoria de absorción de dos fotones (TPA-TCT) donde se necesita una potencia de pico de

pulso alta pero un tiempo prolongado entre pulsos. La técnica de corriente transitoria (TCT) es un método ampliamente utilizado para caracterizar detectores de radiación de semiconductores. Entre otras ventajas, permite determinar la eficiencia de recolección de carga, el voltaje de agotamiento total, el signo de la carga espacial y el tiempo efectivo de atrapamiento de los portadores en los defectos generados por radiación; lo que la ha posicionado como una de las técnicas preferidas a la hora de estudiar la degradación de detectores que operan en entornos de alta radiación. La técnica de corriente transitoria se ha establecido como una herramienta estándar para la caracterización de detectores de partículas de silicio irradiadas y no irradiadas. En esta técnica, la luz láser se utiliza para generar pares de huecos de electrones dentro del material del detector. Posteriormente, se mide la corriente de deriva resultante del movimiento de los portadores de carga generados en el detector de silicio polarizado.

Con el objetivo de lograr una caracterización completamente tridimensional de los detectores de silicio, se puede utilizar la absorción de luz no lineal de dos fotones (TPA). Esta actualización de la técnica de corriente transitoria busca aprovechar el proceso de absorción de dos fotones manteniendo la longitud de onda de emisión de los pulsos del láser en la banda prohibida del silicio (por debajo de 1,12 eV). Sin embargo, la alta potencia de pico de los pulsos ultracortos permite poder hacer un mapeado preciso generando pares de hueco y electrón mediante la absorción instantánea de dos fotones tan sólo en el punto en el que se enfoque el haz láser. El punto focal del láser se puede mover dentro del detector de silicio en los tres ejes espaciales para lograr una resolución tridimensional.

La técnica de corriente transitoria basada en la absorción de dos fotones se ha validado en detectores de silicio utilizando un láser de estado sólido de titanio - zafiro (Ti: Sapphire) como fuente de luz y un amplificador paramétrico óptico, OPA, para cambiar la longitud de onda de emisión a 1,3 μ m. Sin embargo, el uso de esta fuente de luz tiene varias limitaciones y desventajas. En primer lugar, un láser de titanio - zafiro (la fuente de

pulsos de femtosegundos más utilizada) no emite en longitudes de onda donde el silicio es transparente, lo que dificulta el mapeo 3D. Para cambiar la longitud de onda, se debe usar un OPA, lo que reduce la eficiencia del sistema y agrega complejidad a la configuración experimental. En segundo lugar, la energía por pulso es demasiado alta, sobredimensionada para los requisitos de energía de la TPA-TCT. Esto agrega el riesgo de causar daño térmico a los cristales del OPA y requiere, en la mayoría de los casos, que todo el sistema se enfríe con agua. En tercer lugar, para lograr una tasa de repetición lo suficientemente baja que permita analizar el efecto de un solo pulso en el detector de silicio, es necesario utilizar celdas Pockel que funcionan a alto voltaje, lo que introduce ruido eléctrico en las medidas realizadas. Finalmente, las fuentes láser de femtosegundos basadas en titanio - zafiro adaptadas con un OPA tienen altos costes, dificultades de alineación y mantenimiento debido a su estructura láser de espacio libre y vida útil limitada.

En esta tesis se presenta el desarrollo y la aplicación de un láser de fibra a la técnica TPA-TCT, diseñado para superar las limitaciones que muestra el láser de estado sólido de titanio - zafiro. Esta fuente láser tiene todas las ventajas de una arquitectura de fibra óptica: robustez, excelente disipación térmica, alta eficiencia y salida de fibra. Su libertad de diseño permite cumplir con los requisitos del TPA-TCT. Al ser un láser con un medio activo dopado con erbio, la longitud de onda de emisión es de 1550 nm, dentro de la región de transparencia del silicio. Como ya se ha comentado, esto permite el mapeo 3D de las muestras. Los pulsos de salida tienen un ancho temporal de menos de 300 fs y más de 10 nJ de energía por pulso, lo que posibilita una excitación eficiente de dos fotones. El sistema completo no presenta ningún elemento que requiera de un alto voltaje, por lo que el ruido eléctrico en los equipos de medida es inexistente. Finalmente, el sistema láser presenta una desviación estándar en potencia promedio y amplitud pulso a pulso por debajo del 1 %, lo que facilita obtener medidas directas evitando correcciones matemáticas, reduciendo el error derivado en los datos finales. Adicionalmente, se ha desarrollado un módulo de

gestión de pulsos para satisfacer las necesidades específicas de la TPA-TCT. El módulo incluye, en primer lugar, un selector de pulsos basado en tecnología de modulación acústoóptica. Este dispositivo permite disminuir la frecuencia de repetición de la señal pulsada, desde 8.0 MHz hasta disparo único, sin introducir ruido eléctrico ni alterar las propiedades del pulso óptico. En segundo lugar, un filtro de densidad neutra variable que hace posible una selección continua de energía de pulso desde 10 nJ hasta 10 pJ. Finalmente, un disparador de salida sincronizado, una señal fotodetectada con una amplitud proporcional a la energía del pulso de salida y un obturador electromecánico, para facilitar el procedimiento de medición. En el marco de esta tesis, se ha desarrollado un primer prototipo y se ha utilizado para realizar pruebas de validación como fuente de excitación en la TPA-TCT.

Doctorado Industrial

Un aspecto importante de esta tesis es su carácter industrial, lo que significa que los láseres que se desarrollan en ella deben poder ser industrializados y comercializables. Para lograr un producto industrializado, debe pasar todos los niveles de disponibilidad de la tecnología (TRL), que constituyen un método para estimar la madurez de la tecnología durante la fase de desarrollo de un producto. Estos niveles fueron creados por la NASA durante la década de 1970 y su uso permite discusiones consistentes y uniformes sobre la madurez técnica en diferentes tipos de tecnología. Los TRL se basan en una escala del 1 al 9, siendo 9 la tecnología más madura. Según la definición de la Comisión Europea, los niveles de disponibilidad de la tecnología son:

TRL 1 - Principios básicos observados;

TRL 2 - Concepto tecnológico formulado;

TRL 3 - Prueba de concepto experimental;

TRL 4 - Tecnología validada en laboratorio;

TRL 5 - Tecnología validada en un entorno relevante (entorno industrialmente relevante en el caso de tecnologías habilitadoras clave);

TRL 6 - Tecnología demostrada en un entorno relevante (entorno industrialmente relevante en el caso de tecnologías habilitadoras clave);

TRL 7 - Demostración del prototipo del sistema en el entorno operativo;

TRL 8 - Sistema completo y cualificado;

TRL 9 - Sistema real probado en el entorno operativo (fabricación competitiva en el caso de tecnologías habilitadoras clave; o en el espacio).

Por lo general, las tesis doctorales que estudian fenómenos experimentales o desarrollan soluciones para ser utilizadas en aplicaciones específicas avanzan tecnológicamente hasta el nivel TRL3, como máximo hasta el nivel TRL4. En esta tesis, los modelos láser presentados pasan por todos los niveles de TRL, alcanzando el nivel TRL9, lo que refleja el carácter industrial de la misma. Además, el desarrollo se centra en conseguir una nueva tecnología, adaptada a las aplicaciones, que sea a su vez robusta, reproducible y comercializable.

Trabajo Futuro

El desarrollo y los resultados del trabajo que se presenta en esta tesis plantean un conjunto de nuevas ideas y propuestas que podrían llevarse a cabo en un futuro próximo. Las propiedades de los láseres de fibra óptica estudiadas en la sección de frecuencias de repetición en el rango de los gigahercios son adecuadas para aplicaciones de baja potencia. Sin embargo, las aplicaciones más prometedoras desde el punto de vista de las perspectivas comerciales, como las comunicaciones fotónicas de larga distancia, las comunicaciones ópticas inalámbricas y la PADC, necesitan láseres de fibra que entreguen mayor potencia de pico, mayor potencia media y menor duración de pulso. En ese sentido, los conceptos y técnicas estudiados en este volumen para cavidades ultracortas podrían extenderse para implementar

etapas amplificadoras de alta potencia utilizando fibras de dispersión y coeficiente no lineal que permitan ampliar el espectro y comprimir el pulso durante el proceso de amplificación. Trabajando en esta dirección, actualmente se ha conseguido construir un prototipo para lograr un haz emisor con las siguientes características: longitud de onda central de emisión de 1535 nm, pulsos de <100 fs, potencia promedio> 1.0 W y tasa de repetición> 1 GHz, con resultados prometedores. Para mejorar aún más las aplicaciones de telecomunicaciones, también es importante centrar la longitud de onda central de la emisión láser alrededor de 1550 nm. Debido a la relación entre la absorción y la ganancia en el núcleo de las fibras activas, estas tienden a emitir a longitudes de onda más cortas cuanto más corta es la fibra activa. Las cavidades que emiten naturalmente con frecuencia de repetición de gigahercios tienen solo unos pocos centímetros de largo (10,3 cm a una frecuencia de repetición de 1 GHz y 4,7 cm a una frecuencia de repetición de 2,2 GHz), por lo que la longitud de onda central de emisión se desplaza hacia longitudes de onda cortas, en este caso, 1535 nm. Para lograr una emisión a longitudes de onda más largas, la solución más directa sería actuar sobre la función de reflexión de uno de los espejos, obligando a la cavidad a emitir a la longitud de onda deseada. Una primera aproximación es utilizar un espejo absorbente de semiconductor resonante (RSAM) cuyo espectro de reflexión sea más afilado alrededor de 1550 nm. Por otro lado, también es posible actuar sobre el espectro de reflectancia del segundo espejo de la cavidad centrando su función de reflexión en 1550 $\pm$ 10 nm.

Aunque es muy versátil, el láser presentado en la sección referente a frecuencias de repetición desde disparo único a decenas de megahercios se podría mejorar para proporcionar una estructura de fibra completa y pulsos más cortos. Esto aumentaría su aplicabilidad en la técnica de corriente transitoria basada en la absorción de dos fotones. La estructura "todo-fibra" simplificará el sistema de medición reduciendo el número de elementos ópticos entre la salida del láser y la muestra. Los pulsos más cortos producirán un aumento en la eficiencia de la absorción de dos fotones,

aumentando el rango dinámico del sistema. Para lograr pulsos más cortos es necesario mantener la coherencia pulso a pulso a través de las etapas de estiramiento y amplificación para que el pulso pueda comprimirse hasta el límite de la transformada de Fourier de su espectro. Una propuesta que se está investigando actualmente en FYLA es reemplazar la etapa de estiramiento basada en una fibra de alta dispersión normal con un par de redes de Bragg dispersivas. Además, estas redes se pueden controlar por temperatura para ajustar la dispersión neta del sistema. Esta configuración se conoce como TPSR (reflector extensible de pulso sintonizable). Se espera que esta etapa de estiramiento mantenga la coherencia pulso a pulso mejor que el estiramiento producido por la fibra utilizada en esta tesis (PM2000D). En esta configuración, se evitan los empalmes entre diferentes fibras (PM2000D empalmada a PM1550-XP) y el camino óptico total recorrido por el pulso es mucho más corto (40 m vs 1-2 m). Por otra parte, la capacidad de sintonización del TPSR mueve el sistema hacia la solución totalmente de fibra, ya que esta configuración reemplaza al compresor de espacio libre y se puede calibrar para lograr variaciones en la duración del pulso entre 100 y 300 fs.

Otra actualización que se está investigando para lograr un sistema más robusto es incluir un selector de pulsos acustoóptico con entrada y salida en fibra. Esto permitirá controlar la frecuencia de repetición del equipo después de la etapa de amplificación y también, cambiando la potencia de la señal de RF de control, modificar las pérdidas introducidas por el selector de pulsos, variando así la energía del pulso a la salida del láser. Estas mejoras harían posible eliminar el módulo de gestión de pulsos de espacio libre (LPM), dando como resultado un sistema más compacto, robusto y portátil.

Acknowledgements

A menudo se tiende a pensar que la escritura de una tesis doctoral es el fruto de un extenso, intenso y profundo período formativo, y eso no puede ser menos erróneo. Sin embargo, el tiempo de vida invertido a lo largo de la tesis la convierten en un camino de crecimiento personal además de un excelente reto intelectual e investigador. Los viajes de este carácter rara vez se resuelven en soledad y este caso no es una excepción. Ha habido muchísimas personas a mi lado acompañándome en este largo, fascinante y complejo recorrido.

En el plano profesional estoy convencido de que este trabajo no hubiese llegado a ser lo que es sin la guía brillante de mi director de tesis, el Dr. Pere Pérez, que escuchó y ordenó pacientemente mis enmarañadas ideas (y mi estilo de escritura) llevando por buen camino la labor emprendida. Además, le agradezco su calidad humana y profesional de las que, tras cicno años, sigo aprendiendo cada día. Al Dr. Antonio Díez, mi tutor académico, por introducirme en el apasionante mundo del electromagnetismo cuando todavía era un joven estudiante de grado. Al Dr. Miguel V. Andrés por guiarme en mi trabajo de fin de grado y enseñarme los primeros secretos de las fibras ópticas, que sirvieron de preámbulo de esta tesis doctoral. A la Dra. Martina Delgado, que me proporcionó las habilidades con los equipos de laboratorio, incluso electrocutándose en el proceso. A Victoria Gea, por su inspiradora presencia al iluminar el denso y frondoso camino de la burocracia universitaria y estatal.

Una tesis centrada principalmente en la elaboración de láseres de fibra óptica necesita de la colaboración constante y profesionalizada de un equipo que sea experto en el diseño y fabricación de fibras ópticas. Agradezco de forma especial y sincera a nuestros colaboradores en XLim, los doctores Philippe Roy, Raphael Jamier y Roman Douliat por acogerme en su centro de investigación y tratarme con toda la hospitalidad que cualquier persona pudiera desear (cena francesa y jacuzzi incluidos).

El desarrollo de láseres destinados a aplicaciones tecnológicas de vanguardia sería imposible de conseguir sin un equipo con experiencia en dichas aplicaciones que realice pruebas de concepto, sugiera mejoras y apoye el trabajo realizado en esta tesis. Quiero expresar también mi más sincero agradecimiento a los doctores Michael Moll, Marcos Fernández, Raúl Montero e Iván Vila por confiar en este proyecto y darle todo su apoyo. También agradezco enérgicamente a Mortiz Wiehe, cuya tesis doctoral paralela a la mía presenta un trabajo complementario de gran interés.

Tengo que dejar constancia de mi agradecimiento hacia todo el equipo de FYLA no sólo por el apoyo técnico y emocional a lo largo de esta tesis sino también por el entusiasmo y la frustración compartidas durante los experimentos y proyectos que forman parte de este trabajo. Al Dr. Salvador Torres por sus milimétricos consejos de alineamiento. A Aitor García por pelearse con cables y placas. A Azahara Almagro por amenizar los viajes en coche y su férreo sentido del humor. A Gaia María Santina Sardiello por vender más prototipos de los que podíamos construir y porque el "bullying" siempre es mejor cuando ella está de tu parte. Al Doctor Abreu por ser un maestro del python y ayudarme a automatizar el osciloscopio y a Iñaki Aporta que, aunque su paso por FYLA fue breve, siempre le llevaré en el corazón.

Como ya he dicho, la tesis doctoral no es sólo un recorrido técnico y científico sino también de crecimiento personal y, en muchas ocasiones, compañeros se convierten en amistades que uno sabe que van a durar eternamente. Es por ello que tengo una deuda especial con Viorel Otgon que me ha acompañado en los picos y en los valles de este viaje. Hemos ido a congresos, cursos, ferias, entregas, bodas, fiestas y hemos compartido alegrías, penas e incontables cervezas. Hemos visto el CERN desde dentro tras conducir doce horas seguidas, hemos ido al gimnasio y a la sauna. También hemos roto fibras, diodos y componentes electronicos. Y, por si fuera poco, hemos fabricado algún láser. Gracias, Amigo.

En el plano personal, mi camino ha estado acompañado por aquellos que

llevan apoyándome desde siempre. Muchas veces, la costumbre de su soporte constante e incondicional les hace pasar desapercibidos pero, en mi caso, son los que más merecen mis palabras de gratitud.

En primer lugar, me gustaría mencionar a mis amigos de la infancia, mis amigos de Cartagena. Hace ya muchos años que no residimos en la misma ciudad, pero cada vez que nos vemos parece que el tiempo se detenga y eso me ha permitido recuperar el aliento que necesitaba para acabar con éxito esta tesis. A Sandra Blaya por entretenerme con sus dramas. A Victor Capelli por encontrar trabajo en Valencia y poder apoyarme desde cerca. A Pete por ser un ejemplo a seguir doctoralmente hablando. A Carmen Iñiguez por las cervecicas en el Charro. A Alejandro Olivo por tener siempre algo con lo que actualizar mi playlist y a Daniel Ballesta porque más que un amigo, es un hermano.

En segundo lugar debo reconocer que el ejemplo académico de mi madre, el impulso creativo de mi padre y el sentido del humor de mi hermana, junto con la comprensión y el apoyo moral recibidos por parte de todos ellos han sido fundamentales para mí a lo largo de estos años.

Seguidamente me gustaría agradecer el apoyo en la distancia recibido por Nerea Dasilva, compañera de rugby, doctorado y survivals por sus correcciones a mi inglés, en ocasiones chapucero, y por brindarme ayuda siempre que la he necesitado. A Eugenia Llopis, por regresar a mi vida de modo más sano y volver a ser una buena amiga. A mis compañeros de la carrera, Leticia Carrión y Daniel Pérez, por el llanto a tres bandas en estos años de doctorado. A Gonzo, mi amor gallego, por las tardes de rol y los fines de semana en Madrid a base de helado y burritos picantes. A Macarena, mi psicóloga, por acompañarme en este camino de crecimiento personal y a Marcos González, por ser mi camarada de mágicas: el encuentro.

También me gustaría agradecer a todos mis compañeros del Tatami Rugby Club haberme dado la posibilidad de despejar la mente, a veces con golpes y otras veces con cervezas.

Ha habido un factor imposible de predecir que ha enmarcado la etapa final de este recorrido, el Sars-CoV-2. Desde el prisma de la realización de esta tesis, debo estarle agradecido también, ya que me ha proporcionado el aislamiento y la concentración necesarias para poder redactar y recopilar el trabajo realizado.

No podría terminar estas páginas de agradecimiento sin mencionar a mi prometida, mi compañera de vida, Àngela Escribano. Ella ha seguido de cerca todo mi progreso académico y personal. Ha sido la piedra angular de mi bienestar emocional en todos estos años de doctorado y ha crecido conmigo, haciendo lo imposible por apoyarme y ayudarme en esta apasionante aventura que con estas líneas llega a su fin.

Gracias a todos,

Héctor Muñoz

We tend to think that a PhD is the result of a detailed, intense and deep training period, and it actually is. But, because of the hours and time invested, writing a PhD gives place to a lot of personal growth, in addition to being both an intellectual and research-wise challenge. In fact, such challenges can be rarely overcome in solitude, and this case is no exception. There have been a lot of people by my side during this long, fascinating and hard path.

Professionally, this PhD wouldn't be what it is today without the guidance of my thesis supervisor, Dr. Pere Pérez. He listened to me patiently and organized the chaos that was in my head (as well as my writing style) putting me and this PhD on the right track. I also want to thank him because of his human and professional quality, since, after five years, I continue to learn from him. I want to thank Dr. Antonio Díez, my academic tutor, for introducing me to the fascinating world of electromagnetism when I was still an undergraduate. Thanks to Dr. Miguel V. Andrés for guiding me throughout my public dissertation and for teaching me the secrets hiding behind optical fibers, since they were the preamble of this PhD. Thanks to Dra. Martina Delgado, who provided me the skills with lab equipment, even if she had to electrocute herself during the process. To Victoria Gea for throwing some light to state and university bureaucracy.

Since this PhD focuses on the fabrication of optic fiber lasers, it needs the constant collaboration of an expert team in design and fabrication of optic fibers. Special thanks to our colleagues in XLim, doctors Pilippe Roy, Raphael Jamier y Roman Douliat for making their research center a home and for offering me the hospitality anyone would have wished (typically French dinner and jacuzzi included).

Developing lasers for cutting-edge technological applications would be impossible without a team with experience in such applications that has also run concept tests, suggested improvements and supported the work made throughout this PhD. I would also like to express my sincere thanks to doctors Michael Moll, Marcos Fernández, Raúl Montero and Iván Vila

for trusting and supporting this project with all their hearts. Thanks also to Mortiz Wiehe, whose doctoral thesis, parallel to my own, presents a complementary work of great interest.

I couldn't finish without thanking the whole FYLA's team, not only for their both technical and emotional support throughout my PhD, but also for the enthusiasm and frustration shared in each experiment and project that are now part of this work. Thanks to Dr. Salvador Torres for his millimetric alignment tips. To Aitor García for struggling with cables and PCBs. To Azahara Almagro for making road trips less boring and her strong sense of humor. To Gaia María Santina Sardiello for selling more prototypes that we could built and because bullying is always better when she's on your team. To Doctor Abreu who is a master of python and for helping to automatize the oscilloscope. And to Iñaki Aporta who, despite being in FYLA for a short period of time, will always have a place in my heart.

As I've said before, a PhD is not only a technical and scientific journey, but also a personal one. And on many occasions, colleagues become life-long friends. That is why I owe a special thanks to Viorel Otgon, who has been by my side through the highs and lows of this journey. We have been together in congresses, courses, fairs, deadlines, weddings, parties, we have shared both happiness and sorrow and so many beers that I cannot even count them. We have seen CERN from its insides after driving non-stop for over twelve hours. We have also gone to the gym and the sauna. We have broken fibers, diodes and other several electric components. And, as if all that wasn't enough, we have even built some lasers. Thank you, my friend.

On a personal level, this journey has been filled with all the people that have always supported me. A lot of times, this support goes unnoticed because I am used to it by now. But in my opinion, they are the most deserving of my words of gratitude.

Firstly, I would like to thank my childhood friends, the ones I have back

in Cartagena. It's been many years since we all lived in the same town, but every time we get together is as if the time stopped, and they have given me the final push I needed to finish successfully this PhD. Thanks to Sandra Blaya for making her dramas the greatest show ever. To Victor Capelli for finding a job in Valencia and being closer enough to support me. To Pete for being a role model PhD-wise. To Carmen Iñiguez for all those beers at El Charro. To Alejandro Olivo for having the best songs to keep my playlists up to date, and to Daniel Ballesta for being not so much a friend, but a brother.

Secondly, I have to admit that my mother being an academic role-model for me, my father's creativity and my sister's sense of humor, alongside with their constant understanding and moral support, have been essential for me throughout these years.

Next, I would also like to thank Nerea Dasilva (rugby, PhD and survival mate) for her distant support, for her corrections to my sometimes-sloppy English and for helping me any time I needed it. To Eugenia Llopis, for coming back into my life in a much healthier way and for being a great friend. To my university classmates, Leticia Carrión and Daniel Pérez, for sharing a lot of tears throughout these years. To Gonzo, my Galician love, for those afternoons of roleplay and those weekends in Madrid based on ice cream and spicy burritos. To Macarena, my therapist, for being by my side through this process of personal growth. And to Marcos González for being my comrade in "Magic: The Gathering".

I would like to thank my rugby teammates in Tatami Rugby Club for giving me the chance to clear my mind, either through hits or beers.

Obviously, there has been an impossible-to-predict factor that has framed the final stage of this journey, that is Sars-COv-2. I also have to be grateful for this virus since it has giving me the isolation and focus needed in order to draft and compile the work done.

I do not want to finish without mentioning my fiancée, my life partner, Àngela Escribano. She has followed my academic and personal progress closely. She has been the cornerstone of my emotional wellbeing during these years. She has grown by my side, doing everything she could to support me and help me through this adventure that ends right here, with these words.

Thank you all,

Héctor Muñoz

Para mi abuela Isabel y mi abuelo Pepe…

Chapter 1

Introduction

Ultra-fast optics have been a very rich research field for decades, and today ultrashort-pulsed laser systems find numerous applications in areas of fundamental research as well as for medical and industrial applications. Ultra-fast laser systems are used for time resolved studies in chemistry [1], optical frequency metrology [2], terahertz generation [3], two photon and CARS spectroscopy and microscopy [4], optical coherence tomography [5], two photon absorption transient current techniques [6, 7] , photonic analog-to-digital conversion [8] and photonic wireless communications [9, 10]. Medical related applications are eye laser surgery and dentist drills [11]. In the industry, ultrafast lasers are used for micro-machining and marking [12, 13]. The corner stone of ultrafast optics is the mode-locked laser, and developments of mode-locked lasers have been a huge research field in itself.

Traditionally, classical solid-state mode-locked lasers (lasers based on laser crystals like the Ti:Sapphire and the Nd:YAG lasers) have dominated the market. However, solid-state lasers require stable laboratory-like environments with optical tables and stabilized room temperature. Furthermore, solid-state lasers have a high power consumption, and often require maintenance. If ultrafast optics are to gain grounds on much wider commercial markets, solutions to these limitations must be found.

Compared to gas and solid state lasers, fiber lasers are more compact as fibers can be easily bent and coiled [14, 15]. The potential of making compact, rugged laser systems with low power consumption at relative low price make amplified fiber lasers a very promising alternative to classical solid state lasers.

The key properties that make rare-earth doped fibers attractive as laser gain media are the high single pass gain combined with broad gain bandwidths and excellent beam quality. These qualities make fibers attractive as gain media in mode-locked lasers. The active medium is the core of an optical fiber doped with ions of rare earth elements [16]. Such elements (ions) are: erbium (Er3+), neodymium (Nd3+), ytterbium (Yb3+), thulium (Th3+) or praseodymium (Pr3+) among others. The fiber laser active media can be directly pumped by laser diodes. The huge progress and technological development of high power diode lasers, gives a competitive edge compared to classical solid state lasers. In a broad sense, a fiber laser is capable of converting the poor quality output of a continuous wave pump laser diode into a high-brightness spatially coherent light. Moreover, the output of the fiber laser can take several temporal formats, depending on the operation regime: Q-switch, continuous wave or mode-locked, the latter being the regime under study in this thesis.

Mode-locking of a laser refers to a locking of the phase relations between many neighboring longitudinal modes of the laser cavity [17, 18]. Locking of such phase relations enables a periodic variation in the laser output power which is stable over time, and with a periodicity given by the round trip time of the cavity. If sufficient longitudinal modes are locked together with only small phase differences between the individual modes, a short pulse results which may have a significantly larger peak power than the average power of the laser. The origin of mode-locking is best understood in the time domain. A laser in steady state is a feedback system, where the gain per round trip is balanced by the losses. If an element that produces a higher loss at lower powers is introduced in the cavity, the laser may favour

a superposition of longitudinal modes corresponding to a short pulse with high peak power. There are various active and passive elements to achieve this regime.

A further requirement for obtaining stable mode-locking is that the pulse reproduces itself after one round trip (within a total phase-shift on all the longitudinal modes). The phase relations between different modes are affected by effects such as dispersion, gain bandwidth and nonlinear phase shifts. Although an infinite number of different pulses can be constructed as different superpositions of longitudinal modes, usually only a single pulse specified by its shape, duration, peak power and chirp is a stable solution of the cavity, and thus the output pulse characteristics can be designed and controlled by changing the physical parameters of the comprising laser elements.

Various mechanisms, both active and passive [19], exist for mode-locking lasers. In this thesis, passive mode locked lasers based on semiconductor saturable absorber mirrors (SESAM) as mode locking element are studied.

1.1 Ghz-range repetition rates

Femtosecond and picosecond pulsed lasers with high repetition rates (tens of megahertz to tens of gigahertz) are commonly used in different applications. Some of them are photonic-assisted analog-to-digital conversion (PADC) [8, 20], ultrafast spectroscopy [21], optical biomedicine [22–24] and ultrahigh-bit-rate communications such as wavelength-division multiplexing [25, 26] . In reference to PADC's, it has been known since the 1970s [27–31] that short optical pulses ($< 100\ ps$) can be used to enhance the speed of electronic sampling switches through an optoelectronic design. The optical pulse provides lower pulse-to-pulse jitter than electronics and faster rise times. Currently available lasers capable to deliver GHz-range pulse repetition rates are not quite robust and provide low quality signals. This made impossible implementing a reliable PADC system, which is now an open

possibility due to the kind of laser presented in this thesis. An interesting solution to obtain high-repetition rates in a mode-locked configuration is to use linear Fabry–Pérot cavities [16, 28, 32–34]. One of the most important parameters when referring to mode-locked laser combs in PADC is their long term stability. A 1 GHz single fiber Fabry-Pérot oscillator has been achieved previously [32], however, the thermal damage threshold of the SESAM (Semiconductor Saturable Absorber Mirror) is reached producing progressive damage in the SESAM surface and eventually changing laser properties. At this point, the necessity of a theoretical model to study GHz-rate passively mode-locked fiber laser cavities appears.

In this phd thesis, a theoretical model based in the Non-Linear Schrödinger Equation (NLSE) has been developed. Different repetition rates have been studied changing the cavity total length (1.0 GHz, 2.2 GHz, 5.0 GHz and 10.0 GHz). Some of the key parameters characterized for each of the frequencies studied are pump power threshold and gain conditions for stable mode locked emission, SESAM properties, pulse time width and spectral width. The oscillator cavity has been modeled by using a single fiber specially selected to absorb the power of the continuous wave pumping optical signal and the laser light reaching the SESAM, allowing it to work below its thermal damage threshold , $< 1\ mJ/cm^2$. To reach the required absorption values of hundreds of dB/m, a co doped Erbium/Ytterbium fiber has been used, which also provides the dispersion properties needed to generate a solitonic solution of the NLSE, resulting in a stable mode-locked emission. Moreover, all the laser stages (pump and cavity) have a complete PM configuration that, correctly aligned, makes the laser work in a single-polarization regime, enhancing the stability due to the lack of mode competition compared to previous publications. 2 GHz all-fiber lasers [35] and cavities with frequencies above 10 GHz [36] have been previously achieved using complex architectures or specially designed optical fibers. However, in this thesis, the focus is obtaining optimized, robust, compact and repeatable GHz all-fiber lasers using commercial components. When integrating mode-locked fiber lasers in practical applications such as PADC,

it is mandatory to guarantee the long term and environmental stability of the laser source. To confirm experimentally the reliability of the model, robust, stable and ultra-short pulsed light sources have been achieved for 1.0 and 2.2 GHz. Finally, a mechanical design has been developed to enhance the environmental stability of the laser, introducing a cavity temperature control system and an antivibration enclosure.

1.2 Single-shot to MHz range repetition rates

Femtosecond lasers of low repetition rates, from single shot to tens of megahertz, are used in inspection applications, such as the two photon absorption transient current technique (TPA-TCT), where high peak power but long time between pulses is needed. The Transient Current Technique (TCT) is a widely used method for characterizing radiation detectors. Among other advantages, it allows the determination of the efficiency of charge collection, the full depletion voltage, the sign of the space charge or the effective trapping time of the carriers in the defects generated by radiation; which has positioned it as one of the preferred techniques when studying the degradation of detectors operating in high radiation environments [37–40].

TCT has been established as a standard tool for the characterization of unirradiated and irradiated silicon particle detectors. In TCT, laser light is used to generate electron hole pairs inside the detector material. The drift current, resulting from the movement of the generated charge carriers in the biased silicon detector is measured. To achieve a fully three-dimensional characterization of silicon detectors nonlinear two-photon absorption (TPA) of light can be used. To exploit the process of two photon absorption, a laser with photon energies smaller than the band-gap energy in silicon (1.12 eV) has to be used. With high enough intensities at the focal point of the laser, electron-hole pairs can be created by the simultaneous absorption of two photons [6]. The focal point of the laser can be moved

inside the silicon detector in all three spatial axes to achieve a three dimensional resolution [41].

The TPA-TCT technique has been validated on silicon detectors using a Ti: Sapphire solid-state laser as the light source [6] and an Optical Parametric Amplifier, OPA, to shift the emission wavelength to the 1.3 μm range. However, the use of this light source has several limitations and disadvantages. Firstly, a Ti:sapphire laser (the most commonly used source of femtosecond pulses) does not emit at wavelengths where silicon is transparent, which makes correct 3D mapping difficult. To shift the wavelength an OPA must be used, which reduces the efficiency of the system and adds complexity to the experimental setup. Second, the energy per pulse is too high, oversized for the energy requirements of TPA-TCT. This adds the risk of causing thermal damage to the crystals and requires, in most cases, the entire system to be cooled by water. Third, to achieve a repetition rate low enough to analyze the effect of a single pulse on the silicon detector, it is necessary to use pockel cells that work at high voltage though introducing electronic noise into the measurements. Finally, femtosecond laser sources based in Ti:Sa and OPA have high costs, alignment and maintenance difficulties due to their free space laser structure and limited service life.

In this thesis we present the development and application of a fiber laser to the TPA-TCT , designed to overcome the limitations presented by the Ti: Sapphire solid-state laser. This laser source has all the advantages of a fiber optic architecture: robustness, excellent thermal dissipation, high efficiency and fiber output delivery. Its freedom of design allows to meet the requirements of the TPA-TCT. An emission wavelength of 1550 nm (whithin the transparency region of silicon) allows 3D mapping of samples. Less than 300 fs in time width and more than 10 nJ of energy per pulse enable efficient two photon excitation. Finally, the laser system presents a standard deviation in average power and pulse- to-pulse amplitude below 1 %, which allows obtaining direct measurements avoiding mathematical corrections, which reduces the derived error in the final data.

Additionally, a pulse management module has been developed to provide specific needs for TPA-TCT. The module includes: First, a pulse selector based on acousto optic modulation technology. This device allows to decrease the repetition rate of the pulsed signal, from 8.0 MHz o single shot, without introducing electronic noise. Second, a variable neutral density filter that allows continuous pulse energy selection from 10 nJ to 10 pJ. Finally, a synchronizing output trigger, a photodetected signal with an amplitude proportional to the energy of the output pulse and an electromechanical shutter, to facilitate the measurement procedure.

A first prototype has been developed and used to carry out validation tests as excitation source in the TPA-TCT.

1.3 Industrial PhD

An important aspect of this thesis is its industrial nature, which means that the lasers that are developed in it must be able to be industrialized and marketable. To achieve an industrialized product, it must pass all the technology readiness levels. Technology readiness levels (TRLs) are a method for estimating the maturity of technologies during the acquisition phase of a program, developed at NASA during the 1970s. The use of TRLs enables consistent, uniform discussions of technical maturity across different types of technology [42]. TRLs are based on a scale from 1 to 9 with 9 being the most mature technology.

The TRLs, as defined by the European Comission are:

TRL 1 – Basic principles observed

TRL 2 – Technology concept formulated

TRL 3 – Experimental proof of concept

TRL 4 – Technology validated in lab

TRL 5 – Technology validated in relevant environment (industrially relevant environment in the case of key enabling technologies)

TRL 6 – Technology demonstrated in relevant environment (industrially relevant environment in the case of key enabling technologies)

TRL 7 – System prototype demonstration in operational environment

TRL 8 – System complete and qualified

TRL 9 – Actual system proven in operational environment (competitive manufacturing in the case of key enabling technologies; or in space)

Typically, doctoral theses that study experimental phenomena or develop solutions to be used in specific applications advance technologically up to the TRL3 level, at most TRL4. Unlikewise, in this thesis, the laser models presented go through all the TRL levels, reflecting the industrial character of the thesis. In addition, development is focused on achieving a new technology, adapted to the applications that is robust, reproducible and marketable at the same time.

Chapter 2

Mode-Locked Fiber Lasers Dynamics

2.1 Propagation of ultra-short pulses in optical fibers

Ultrafast optics is based on an understanding a quantitative description of the propagation of laser light in a dispersive optical medium. In this chapter, the basic wave equation will be explained [43], followed by the theory of pulse propagation in nonlinear dispersive media [44] .

Like all electromagnetic phenomena, pulse propagation through optical fiber is governed by Maxwell's equations:

$$\nabla \cdot D = \rho \tag{2.1}$$

$$\nabla \cdot B = 0 \tag{2.2}$$

$$\nabla \times E = -\frac{\partial B}{\partial t} \tag{2.3}$$

$$\nabla \times H = j + \frac{\partial D}{\partial t} \tag{2.4}$$

In equations (2.1) to (2.4) E and H are the electric and magnetic vectors, respectively. In the same way, D and B are the corresponding electric and magnetic flux densities. Finally, ρ represents the free charges and j the current density. However, there are no free charges in optical fibers, hence the terms implying ρ and j will vanish. The relation between flux densities and electromagnetic fields are generally given by:

$$D = \varepsilon_0 E + P \;\; and \;\; B = \mu_0 H + M \tag{2.5}$$

In equation (2.5), ε_0 and μ_0 are the vacuum electric permittivity and the vacuum magnetic permeability, respectively. M and P are the magnetic and electric polarization, respectively. As we manage an optical medium, M is zero and it is possible to write the following expression using (2.4) and (2.5):

$$\nabla \cdot B = \varepsilon_0 \mu_0 \frac{\partial E}{\partial t} + \mu_0 \frac{\partial P}{\partial t} \tag{2.6}$$

Taking the curl on both sides of equation (2.3) and using the identity $\nabla \times (\nabla \times E) = \nabla(\nabla \cdot E) - \nabla^2$ E it is possible to relate B to E:

$$\nabla(\nabla \cdot E) - \nabla^2 = -\frac{\partial(\nabla \times B)}{\partial t} \tag{2.7}$$

Finally, using equation (2.6), taking into account that there are no free charges ($\nabla \cdot E = 0$) and supposing that the material is homogeneous ($\varepsilon_0 \mu_0 = \frac{1}{c^2}$) the equation above reduces to the wave equation for isolating, polarizable nonmagnetic materials:

$$\nabla^2 E - \frac{1}{c^2} \frac{\partial^2 E}{\partial t^2} = \mu_0 \frac{\partial^2 P}{\partial t^2} \tag{2.8}$$

To obtain the equation that describes pulse propagation through nonlinear media, the following conditions must be taken into account:

· The polarization response of the material is supposed instantaneous. This is valid for nonlinearities based in electronic nature since the electronic response is much faster than the period of light.

· The nonlinearity in P is supposed small enough to be treated perturbatively.

· The optical field maintains the polarization state, so a scalar approximation can be made.

The first of these conditions, allows to expand the induced polarization in a series of powers of the instantaneous electric field:

$$P = P_L + P_{NL} = \varepsilon_0(\chi^{(1)} \cdot E + \chi^{(2)} \cdot E \cdot E + \chi^{(3)} \cdot E \cdot E \cdot E...) \tag{2.9}$$

In equation (2.9), χ^i represents the susceptibility of order i of the medium. The electromagnetic field can be written as a product of a slowly varying component and a plane wave:

$$\hat{E}(r,t) = \frac{1}{2}u_x[E(r,t)e^{i\beta_0 z - i\omega t} + c.c] = \frac{1}{2}u_x[F(x,y)A(z,t)e^{i\beta_0 z - i\omega t} + c.c] \tag{2.10}$$

$$\hat{P}_L(r,t) = \frac{1}{2}u_x[P_L(r,t)e^{i\beta_0 z - i\omega t} + c.c] \tag{2.11}$$

$$\hat{P}_{NL}(r,t) = \frac{1}{2}u_x[P_N L(r,t)e^{i\beta_0 z - i\omega t} + c.c] \tag{2.12}$$

Here, u_x is the unit vector perpendicular to the direction of propagation, which can be dropped due to the assumption that the polarization is preserved during the propagation through the fiber. Also, $E(r,t)$ and $P_{L/NL}(r,t)$

are the slowly varying envelopes of the electric field and linear/nonlinear polarization respectively. In addition, it is convenient to separate the x,y dependence (F(x,y), modal pattern) from that on z,t (A(z,t), propagation). Finally, it is understood that only the real part is physically meaningful and hence the complex conjugate will not be explicitly stated.

Now, from (2.9) it is possible to write an expression for P_{NL} [44]:

$$P_{NL}(r,t) = \varepsilon_0 \varepsilon_{NL}(r,t) E(r,t) \;\; with \;\; \varepsilon_{NL}(r,t) = \frac{3}{4}\chi^{(3)}|E(r,t)|^2 \tag{2.13}$$

In equation (2.13), ε_{NL} refers to the nonlinear contribution to the dielectric constant. Moreover, the spacial and temporal variations of ε_{NL} are supposed to be slow in comparison to the optical wavelength and period. $\chi^{(2)}$ is not considered because the optical fiber has not a crystal structure, and $\chi^{(2)} = 0$ in this kind of systems. With this in mind, the main objective is to find a solution to the equation (2.8). Aiming this purpose, it is useful to apply a Fourier transform to this equation. When applying Fourier transform, the following form is used:

$$\tilde{E}(r,\omega) = \int_{-\infty}^{+\infty} E(r,t) e^{i\omega t}\, dt \;\; and \;\; E(r,\omega) = \int_{-\infty}^{+\infty} \tilde{E}(r,t) e^{-i\omega t}\, dt \tag{2.14}$$

Usually, ε_{NL} is intensity dependent and Fourier transform must apply to it too, however, since a perturbational approach is used (supposing that ε_{NL} is the perturbation) it can be treated as locally constant. After all this, equation (2.8) is re-written:

$$(\nabla^2 - \varepsilon(r,\omega)\frac{\omega^2}{c^2})\tilde{E}(r,\omega) = 0) \tag{2.15}$$

With the dielectric function given by:

$$\varepsilon(\omega) = 1 + \tilde{\chi}^{(1)} + \frac{3}{4}\tilde{\chi}^{(3)} \tag{2.16}$$

Equation (2.15) can be solved by making an Ansatz that is the Fourier transform of equation (2.10). Here, $\tilde{A}(z,\omega)$ is a slow varying function of z and $F(x,y)$ is the modal distribution of the pulse in the fiber. Tha Ansatz is the folowing:

$$\tilde{E}(r,\omega-\omega_0) = F(x,y)\tilde{A}(z,\omega-\omega_0)e^{ik_0 z} \tag{2.17}$$

In equation (2.17) ω_0 is the carrier frequency and k_0 is the wavenumber of ω_0. Some calculations [44], lead to a couple of equations, for $\tilde{A}(z,\omega)$ and $F(x,y)$:

$$\frac{\partial^2 F}{\partial x^2} + \frac{\partial^2 F}{\partial y^2} + [\varepsilon(\omega)\frac{\omega^2}{c^2} - \beta^2(\omega)]F = 0 \tag{2.18}$$

$$2i\beta_0\frac{\partial \tilde{A}}{\partial z} + (\beta^2(\omega) - \beta_0^2)\tilde{A} = 0 \tag{2.19}$$

Owing the assumption that $\tilde{A}(z,\omega)$ is a slowly varying function of z, its second derivative with respect to z is neglected in both equations. The wavenumber $\beta(\omega)$ is determined by solving the eigenvalue equation of the fiber modes, for details see [44]. At this point, one can approximate the dielectric function by:

$$\varepsilon(\omega) = (n(\omega) + \Delta n)^2 \approx n^2 + 2n\Delta n \tag{2.20}$$

In equation (2.20) Δn is given by the nonlinearity n_2 of the refractive index and the absorption $\tilde{a}$ and the gain $\tilde{g}$ of the fiber:

$$\Delta n = n_2|E|^2 + \frac{i\tilde{a}(\omega) - \tilde{g}(\omega)}{2k_0} \tag{2.21}$$

The solution for the modal distribution $F(x,y)$ is unchanged compared to the case without the perturbation, but the eigenvalue solutions are altered by the perturbation:

$$\tilde{\beta}(\omega) = \beta(\omega) + \Delta\beta \;\; with \;\; \Delta\beta = \frac{k_0 \iint_{-\infty}^{+\infty} \Delta n(x,y)|F(x,y)|^2\, dx\, dy}{\iint_{-\infty}^{+\infty} |F(x,y)|^2\, dx\, dy} \tag{2.22}$$

This first order perturbative method is used also in quantum mechanics. Moreover, as only the transversal single-mode case is contemplated here, the modal distribution is the fundamental mode of the fiber HE_{11} given by [44]:

$$F(x,y) = J_0(\kappa\rho) \;\; with \;\; \rho = \sqrt{x^2+y^2} \leq a \tag{2.23}$$

$$F(x,y) = \sqrt{a/\rho} J_0(\kappa\rho) e^{-\gamma(\rho-a)} \;\; with \;\; \rho = \sqrt{x^2+y^2} > a \tag{2.24}$$

In equations (2.23) and (2.24), J_0 refers to the order zero Bessel function. This modal distribution is hard to work with and for practical purposes it is approximated by the Gaussian distribution:

$$F(x,y) = e^{\frac{-(x^2+y^2)}{w^2}} \tag{2.25}$$

In equation (2.25) ω is the width parameter that is obtained fitting the exact distribution to a Gaussian form.

Rewriting equation (2.19) and approximating $\beta^2(\omega) - \beta_0^2 \approx 2\beta_0(\beta(\omega) - \beta_0)$ yields:

$$\frac{\partial \tilde{A}}{\partial z} = i[\beta(\omega) + \Delta\beta - \beta_0]\tilde{A} \tag{2.26}$$

For a final step, one takes the Fourier transform of above equation to arrive at a time-domain representation of the slowly varying envelope function $A(z,t)$. Since generally an analytic expression for $\beta(\omega)$ is not known, it is helpful to expand it in Taylor series:

$$\begin{aligned}\beta(\omega) &= \beta_0 + (\omega - \omega_0)\frac{d\beta}{d\omega}|_{\omega-\omega_0} + \frac{1}{2}(\omega - \omega_0)^2\frac{d^2\beta}{d\omega^2}|_{\omega-\omega_0} + \cdots \\ &= \beta_0 + \beta_0(\omega - \omega_0) + \frac{1}{2}\beta_2(\omega - \omega_0)^2 + \cdots\end{aligned} \tag{2.27}$$

The cubic and higher terms are negligible if the pulse duration is in the ps-range. For femtosecond pulses, the third order must be taken into account. Substituting equation (2.27) into (2.26) and taking the inverse Fourier transform results in:

$$\frac{\partial A}{\partial z} = -\beta_1\frac{\partial A}{\partial t} - i\frac{\beta_2}{2}\frac{\partial^2 A}{\partial t^2} + i\Delta\beta A \tag{2.28}$$

Fiber losses and nonlinear effect are accounted for by the term $\Delta\beta$ and can be evaluated using the equation (2.21), leading to:

$$\frac{\partial A}{\partial z} + \beta_1\frac{\partial A}{\partial t} + i\frac{\beta_2}{2}\frac{\partial^2 A}{\partial t^2} + \frac{\alpha}{2}A = i\gamma|A|^2 A \;\; with \;\; \gamma = \frac{n_2\omega_0}{cS_{eff}} \tag{2.29}$$

In equation (2.29) γ is the nonlinear parameter and S_{eff} the effective area of the optical fiber. This equation is called Nonlinear Schrödinguer Equation, and it is most commonly used to describe the propagation of ps-range optical pulses along an optical fiber, taking into account fiber losses, chromatic dispersion and fiber nonlinearities.

This is the basic propagation equation that is used in this thesis to design our fiber laser cavities. A gain term has been added for making the simulations and it is presented in the next sections.

2.2 Amplification in rare-earth doped fibers

Incident light of the correct wavelength can be amplified in optical fibers through stimulated emission. This is realized by optically pumping the amplifier fiber to obtain population inversion. Depending on the energy level of the dopants, the lasing scheme can be classified as three or four level scheme (see figure 2.1). In either case, the dopants absorb pump photons and reach an excitation stage and then relax rapidly into a lower-energy excited state.

The lifetime of this "high energy state" is usually long (around 10 ms for Erbium and 1 ms for Ytterbium), and the stored energy is used to amplify incident light through stimulated emission. The difference between the three and four level lasing schemes is the level to which the dopant relaxes after stimulated emission. In the case of a three level lasing scheme, it is directly the ground state, whereas in the case of a four level lasing scheme, it is another intermediate state. Erbium presents a three level lasing scheme while ytterbium has a four level lasing scheme.

Pumping creates the necessary population inversion and hence provides the optical gain. Generally speaking and using the appropriate rate equations [45] for a homogeneously broadened gain medium, one can write:

$$g(\omega) = \frac{g_0}{1 + (\omega - \omega_a)^2 T_2^2 + P/P_s} \tag{2.30}$$

In equation (2.30) g_0 is the peak gain value, ω is the frequency of the incident signal, ω_a the atomic transition frequency and P is the optical power of the signal being amplified. The saturation power P_s is mainly influenced

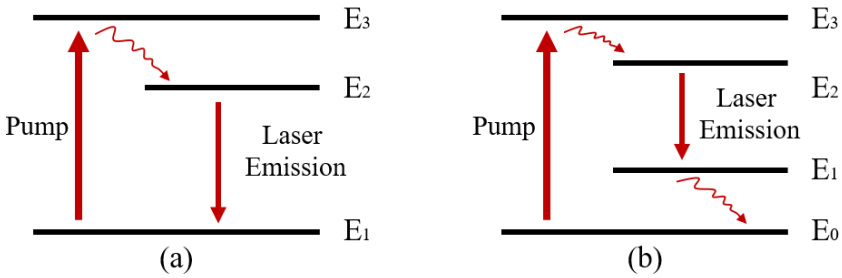

FIGURE 2.1: Illustration of three (a) and four (b) levels laser scheme.The main difference is the way to reach the ground state (E_1 and E_0 respectively) from the excited state (E_2 for both cases).

by parameters such as the fluorescence time T_1 and the transition cross section σ. The parameter T_2 is the dipole relaxation time.

If one neglects the saturation effect for the moment, the equation shows that the gain reduction for frequencies off the transition frequency is governed by a Lorentzian gain profile as to be expected from a homogeneously broadened system. The gain bandwidth $\Delta\nu$ is defined as the full width at half maximum (FWHM) of the gain spectrum $g(\omega)$, given for a Lorentzian spectrum as:

$$\Delta\nu_g = \frac{1}{\pi T_2} \tag{2.31}$$

However, the gain spectrum of a fiber laser is considerably affected by the amorphous nature of the silica and the presence of other co-dopants such as aluminum or germanium, presenting several peaks. It can be clearly seen, that the Lorentzian approximation is not sufficient.

To make a better estimation of the influence of the gain in a doped media, the implications of gain provided by dopants for the nonlinear Schrödinger

equation will be described.

The lifetime of the first upper state is significantly shorter than the lifetime of the level from which stimulated emission takes place. Thus the lasing process can be approximated by a two-level system. The dynamics of a two level system are described by the Maxwell-Bloch equations [45]. The starting point is the wave equation (2.8). The induced polarization $P(r)$ has to be altered to include a third term $P_d(r)$ representing the contributions of the dopants. Using the slowly varying envelope approximation (SVEA) similar to equation (2.12), one obtains:

$$\hat{P}_d(r,t) = \frac{1}{2}u_x[P_d(r,t)e^{(i\beta_0 z - i\omega t)} + c.c.] \tag{2.32}$$

The slowly varying part obeys the Bloch equations [45] which relate the population inversion density $W = N_2 - N_1$ to the polarization and electric field:

$$\frac{\partial P(r,t)}{\partial t} = -\frac{P(r,t)}{T_2} - i(\omega_a - \omega_0)P(r,t) - \frac{i\mu^2}{\hbar}E(r,t)W \tag{2.33}$$

$$\frac{\partial W}{\partial t} = \frac{W_0 - W}{T_1} + \frac{1}{\hbar}Im(E^*(r,t)\cdot P(r,t)) \tag{2.34}$$

In these equations, W_0 is the initial population inversion, μ is the magnetic dipole moment, ω_a is the atomic transition frequency, and $E(r,t)$ is the slowly varying amplitude. Following the same derivation, the nonlinear Schrödinguer equation (2.29) is modified as follows:

$$\frac{\partial A}{\partial z} + \beta_1\frac{\partial A}{\partial t} + i\frac{\beta_2}{2}\frac{\partial^2 A}{\partial t^2} + \frac{\alpha}{2}A = i\gamma|A|^2A + \frac{i\omega_0}{2\varepsilon_0 c}\langle P_d(r,t)\rangle \tag{2.35}$$

The brackets angles denote an averaging over the mode profile $|F(x,y)|^2$. This term is written as g in the equation (2.51) and reflects the gain in the

amplitude of the pulse field throughout its propagation. In summary, the pulse propagation in an optical fiber is governed by a generalized nonlinear Schrödinguer Equation (2.29) including gain parameters if dopants are present in the fiber.

2.3 Mode-Locking

Ultra-short pulses with a duration of a few ps or less can only be achieved by mode-locking the laser. For this purpose, one has to establish a rigid phase relation between the many longitudinal modes which can exist in a laser cavity of a certain length. The principle of mode-locking will be introduced with special emphasis on passive mode-locking using saturable absorber device, as this is the method of choice for the erbium and erbium-ytterbium doped fiber lasers developed in this thesis.

The propagation of electromagnetic pulse in a laser resonator can be described by a superposition of plane waves with different wavelengths. The possible wavelengths of the longitudinal modes in a Fabry-Pérot resonator are given by the condition:

$$n \cdot \lambda_n = 2L \tag{2.36}$$

Here, λ_n is the wavelength of the longitudinal mode, L is the resonator length and n is an integer. In principle, a large number of modes of different frequencies can exist at the same time. These modes will be independent in phase and amplitude. Thus the total electric field in the resonator is given by the sum of the field of all the excited modes:

$$E(z,t) = \sum_n E_n(z,t) = \sum_n E_{0,n} e^{ik_n z - i\omega_n t} \quad with \quad E_{0,n} = |E_n| e^{i\Phi_n} \tag{2.37}$$

In equation (2.37) $E_{0,n}$ is the complex amplitude of the n-th mode and Φ_n is its phase. Assuming an equal amplitude for all modes, the intensity is given by:

$$I(z,t) = E(z,t)E^*(z,t) = |E_0|^2 \sum_{n=1}^{N} \sum_{m=1}^{N} e^{i(\Phi_n - \Phi_m)(n-m)\Omega(\frac{z}{c}-t)} \tag{2.38}$$

Here,

$$\Omega = \omega_{n+1} - \omega n = \frac{\pi c}{L} \tag{2.39}$$

In equations (2.38) and (2.39), Ω is the frequency difference between two neighbouring modes. If all modes have a fixed phase relation, which means that $\Phi_n - \Phi_m = \delta\Phi$, equation (2.38) yields:

$$I(z,t) = |E_0|^2 e^{i\delta\Phi} \sum_{n=1}^{N} \sum_{m=1}^{N} e^{(n-m)\Omega(\frac{z}{c}-t)} \tag{2.40}$$

The second exponential function in equation (2.40) becomes equal to 1 for all terms of the sum if the following condition is fulfilled:

$$\Omega(\frac{z}{c} - t) = 2\pi \cdot j \quad \rightarrow \quad z - ct = 2L \cdot j \;\; being \;\; j = 0, 1, 2, 3... \tag{2.41}$$

The maximum of equation (2.40) undes these condition is:

$$I_{max} = N^2 |E_0|^2 = N^2 I_0 \tag{2.42}$$

One can derive the spatial and temporal distances of consecutive pulses when this conditions are fulfilled:

$$\Delta z = 2L, \qquad \Delta t = \frac{2L}{c} \equiv T \tag{2.43}$$

Where T results the repetition rate of the pulsed mode-locked laser.

That means that through a fixed phase relation between the many modes in the resonator, regular pulses with peak intensity I_{max} will develop, proportional to the sqare of the number of involved modes, as it is seen in figure 2.2.

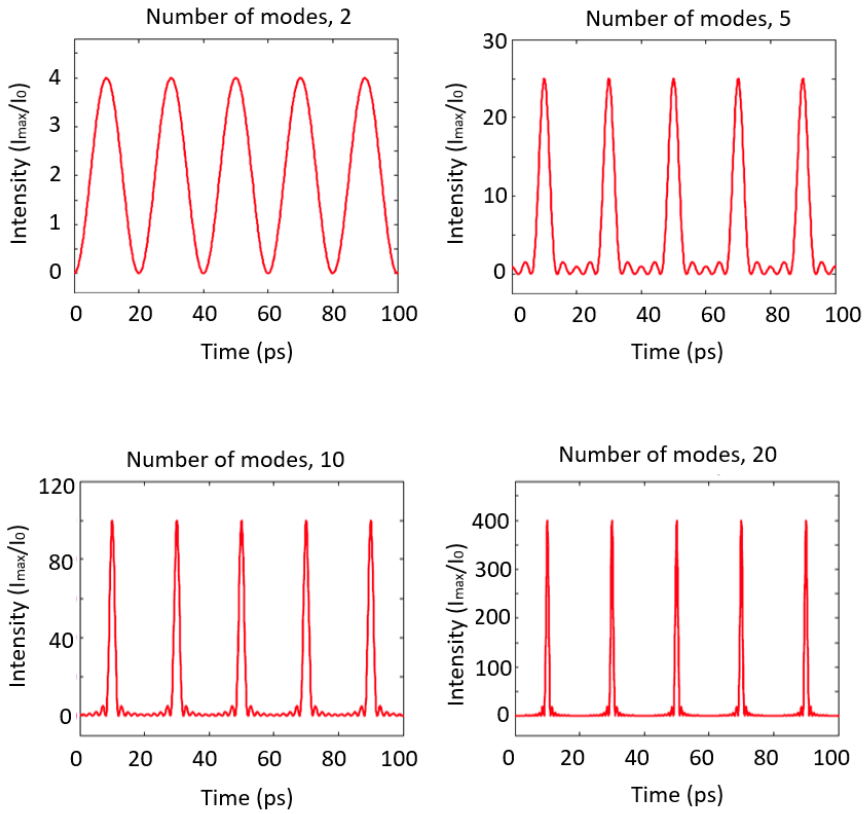

FIGURE 2.2: Superposition of a different number of longitudinal modes with a fixed phase difference. The intensity of these pulses scales quadratically with the number of involved modes.

To calculate the FWHM (full width half maximum) of the pulses, one can assume that at a fixed time t=0 the superposition of N modes is similar to

the interference of N planar waves. Using the geometric series, one arrives at [46, 47]:

$$I(t) = I_0 \frac{sin^2\left(\frac{N\Omega}{2}t\right)}{sin^2\left(\frac{\Omega}{2}t\right)} \tag{2.44}$$

Using equation (2.44) one can derive the FWHM of the pulses:

$$\Delta T = \frac{T}{N} \tag{2.45}$$

So the pulse width decreases with the number of superposed modes and it is proportional to the revolution time of the laser cavity.

This rigid phase relation between superposing modes can be achieved by a modulation of the gain of the resonator (or the losses respectively) with the difference frequency Ω of adjacent modes. All mechanisms to achieve a mode-lock rely on that principle (see figure 2.3).

Through the loss modulation, the electromagnetic field in the resonator acquires an additional time dependence:

$$\begin{aligned} E_n(z,t) &= \left[E_{0,n} + E_n^{mod} \cdot cos(\Omega t)\right] e^{ik_n z - i\omega_n t} \\ &= \left[E_{0,n} e^{-i\omega_n t} + \frac{1}{2} E_n^{mod}\left(e^{-i\Omega t} + e^{i\Omega t}\right) e^{-i\omega_n t}\right] e^{ik_n z} \\ &= \left[E_{0,n} e^{-i\omega_n t} + \frac{1}{2}\left(e^{i\omega_{n+1} t} + e^{-i\omega_{n-1} t}\right)\right] e^{ik_n z} \end{aligned} \tag{2.46}$$

Equation (2.46) shows that the time dependence induces sidebands in every mode whose frequencies coincide with the one of the neighboring modes. As this principle is valid for the total bandwidth, a phase synchronization between all longitudinal modes is reached. There are various possibilities to achieve this time dependence of the electromagnetic field. They can be

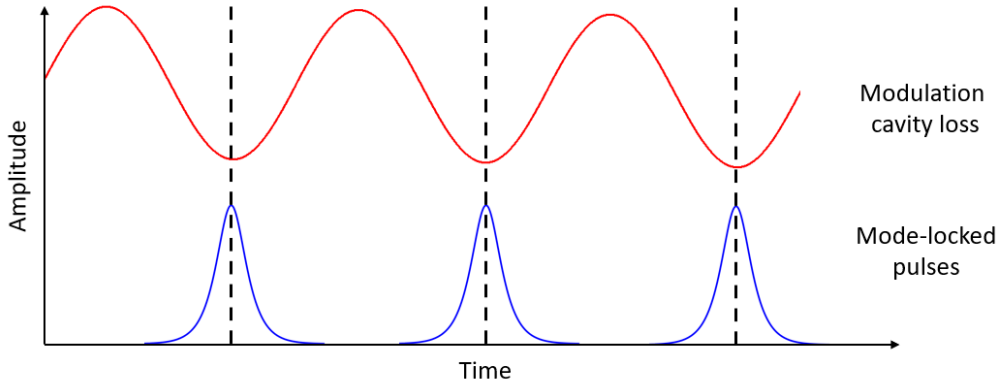

FIGURE 2.3: Schematic illustration of active mode-locking through modulation of cavity losses [44]

categorized by the method of how the gain modulations are accomplished. If an actively driven device, for instance a switch or amplitude modulator is used, one speaks of active mode-locking, if a passive device (a saturable absorber, for instance) is used, one speaks of passive mode-locking.

2.3.1 Active Mode-Locking

This very common form of mode-locking requires an actively driven element in the laser cavity, either modulating the amplitude (AM mode-locking) or the phase (FM mode-locking) of the propagating light. To ensure phase synchronization, the amplitude/phase must be modulated with a frequency equal to the harmonic of the mode spacing. Active mode-locking can be understood in both time and frequency domains. An amplitude modulation of a sinusoidal signal creates modulation sidebands as is well known through, for example, AM radio transmission. In time domain, the picture is that the modulator creates cavity losses. As the laser emits more light during minimum loss, this intensity difference will accumulate during successive round trips leading to a mode-locked behavior

after reaching a steady state (see figure 2.3). The cavity loss introduced by a modulator can be written as:

$$\alpha = \alpha_c + \alpha_m \left[1 - cos(\omega_m t)\right] \tag{2.47}$$

Here, α_c are the regular cavity losses and α_m is the additional loss introduced at frequency ω_m.

2.3.2 Passive Mode-Locking

Besides the ability to model dispersion, gain, losses, nonlinearities etc. in fibers, one important component is still missing to model mode-locked lasers. This is the nonlinear component used to make mode-locked lasing more favorable than CW lasing. For a laser to favor lasing mode with short pulses, an element or a combination of elements have to be present in the cavity, which introduce a higher loss at low power, so that a short pulse with higher peak power experiences a stronger net gain.

One possibility is to use a SESAM (Semiconductor Saturable Absorber Mirror) as in this thesis. A SESAM consists of a Bragg-mirror on a semiconductor wafer like GaAs, incorporating materials with an intensity dependent absorption. The saturable absorber layer consists of a semiconductor material with a direct bandgap slightly lower than the photon energy. Often GaAs/AlAs is used for the Bragg mirrors and InGaAs quantum wells for the saturable absorber material. During the absorption electron-hole pairs are created in the film. As the number of photons increases, more electrons are excited, but as only a finite number of electron-hole pairs can be created, the absorption saturates. The electron-hole pairs recombine non-radiatively, and after a certain period of time they are ready to absorb photons again. Key parameters of the SESAM when designing mode-locked lasers are the recovery time, the modulation depth of absorption, the bandwidth, the saturation intensity and the non-saturable losses.

Generally the Bragg stack can be chosen to be either anti-resonant or resonant. SESAM based on resonant Bragg stacks can have quite large modulation depths, but with the limited bandwidth of the resonant structure. Anti-resonant SESAM can have quite large bandwidths (>100nm), but at the expense of a smaller modulation depth. A larger modulation depth can be obtained from an anti-resonant design at the expense of higher intrinsic losses. In solid state lasers where the single pass gain is low, the unsaturable losses of the SESAM must also remain low, but in fiber lasers where the single pass gain is much higher, unsaturable losses are less important.

The recovery time should ideally be as small as possible. Recovery times on the order of the pulse duration will cause asymmetric spectra if the pulse is chirped when it interacts with the SESAM, and hence strongly affect the pulse dynamics inside the cavity. Even larger recovery times can limit the obtainable pulse duration from the laser. This time, a fast SESAM is used. For an extensive overview of SESAMs [48, 49]. For an extensive theoretical and analytical analysis of mode-locking with saturable absorbers see [46, 47].

For fast saturable absorbers with recovery times much faster than the pulse length, the loss can be modeled by:

$$q = \frac{q_0}{1 + \frac{|A|^2}{P_{SA}}} \tag{2.48}$$

For SESAM where the recovery time is of the order of the pulse length or more, one cannot suppose that it works instantly. A more appropriate model of the SESAM is:

$$\frac{\partial q(t)}{\partial t} = -\frac{q - q_0}{\tau_{SA}} - q\frac{|A|^2}{E_{SA}} \tag{2.49}$$

In equations (2.48) and (2.49), $A(z,t)$ is the slow varying component of the electromagnetic field, q_0 is the non-saturated but in principle saturable

loss, P_{SA} is the saturation power, E_{SA} is the saturation energy and τ_{SA} is the recovery time. In the limit $\tau_{SA} \to 0$ equation (2.49) approaches to (2.48)

The differential equation can be numerically integrated to give $q(t)$, and from $q(t)$ the reflectance from the SESAM can be calculated as:

$$R(t) = 1 - q(t) - l_0 \tag{2.50}$$

Here, l_0 is the intrinsic insertion loss. Reflection of the slowly varying electric field can then be calculated as $A(t)\sqrt{R(t)}$. The saturation energy can be calculated as the product of the saturation fluence and the effective area of the SESAM.

A general tendency of mode-locked lasers with saturable absorbers of finite recovery times is that the laser may tend to Q-switch mode-lock (i.e. emit a mode-locked pulse train which is highly amplitude modulated on a nanosecond time scale and hence resemble a nanosecond pulse with a mode-locked pulse train underneath the pulse envelope). The tendency to Q-switch mode-lock is increased if the modulation depth is high. To avoid Q-switched mode-locking, the spot size on the SESAM can either be decreased, or the intra cavity average power increased (by either decreasing the output coupling or by increasing the pump power). However, the limit is set by the damage threshold of the SESAM. If the peak intensity of the pulse is increased above the damage threshold of the SESAM (typically $300MW/cm2$), the SESAM may be permanently damaged, and a small spot burned on the surface.

There are other methods of passive mode-locking but they are not contemplated in this thesis since a SESAM is used on the fiber mode-locked lasers.

2.4 Split-Step Fourier Transform Method

Aiming a proper design of the cavity, several numerical simulations have been done. They are based on the nonlinear Schrödinguer equation. The method that has been employed is the Split-step Fourier transform method that is briefly explained in this section.

As it has been said, this is a convenient method for solving the nonlinear Schrödinger equation in which the third order dispersion, β_0, and the gain, g, have been included:

$$\frac{\partial A}{\partial z} + \beta_1 \frac{\partial A}{\partial t} + i\frac{\beta_2}{2}\frac{\partial^2 A}{\partial t^2} - \frac{\beta_3}{6}\frac{\partial^3 A}{\partial t^3} + \frac{\alpha - g}{2}A = i\gamma|A|^2 A \tag{2.51}$$

This method is based on the assumption that dispersion and nonlinear effects act independently over a short piece of fiber. It is useful to write equation (2.51) formally as:

$$\frac{\partial A}{\partial z} = \left(\hat{D} + \hat{N}\right) A \tag{2.52}$$

Where $\hat{D}$ is the differential operator counting for dispersion and absorption in a linear medium and $\hat{N}$ is the nonlinear operator governing all nonlinear effects on pulse propagation. They are given by:

$$\hat{D} = -\beta_1 \frac{\partial A}{\partial t} - i\frac{\beta_2}{2}\frac{\partial^2 A}{\partial t^2} + \frac{\beta_3}{6}\frac{\partial^3 A}{\partial t^3} - \frac{\alpha - g}{2} \tag{2.53}$$

$$\hat{N} == i\gamma|A|^2 \tag{2.54}$$

Propagation over a small distance h is carried out in three steps. First the pulse propagates over half the distance with only dispersive effects. Then, in the middle of the section, nonlinearity is included after which the pulse propagates again half the distance.

Mathematically, this results in:

$$A(z+h,t) \approx exp\left(\frac{h}{2}\hat{D}\right) exp\left(\int_z^{z+h} \hat{N}(z')\,dz\right) exp\left(\frac{h}{2}\hat{D}\right) A(z,t) \quad (2.55)$$

The exponential operator can be readily evaluated in the Fourier domain. For the dispersive operator $exp\left(\frac{h}{2}\hat{D}\right)$, this yields:

$$exp\left(\frac{h}{2}\hat{D}\right) A(z,t) = FFT_t^{-1} exp\left(\frac{h}{2}\hat{D}(i\omega)\right) F_t A(z,t) \quad (2.56)$$

Here $\hat{D}(i\omega)$ is obtained replacing the differential operator $\partial/\partial t$ by $i\omega$. As $\hat{D}(i\omega)$ is just a number in Fourier space, the evaluation of equation (2.56) is fairly straightforward.

Chapter 3

GHz-Range Passively Mode-Locked Fiber Lasers

The theoretical model presented in chapter 2 is adapted to design GHz range passively mode-locked fiber lasers. The modeled cavities of the lasers are configured by a highly doped and polarization- maintaining single fiber of a single type. For different pulse repetition rates, ranging from one GHz to ten GHz, gain parameters and pump threshold for a stable mode-locked laser emission are studied. Pulse time width, spectral width and SESAM properties are defined to achieve stable emission. To experimentally validate the theoretical model, 1.0 GHz and 2.2 GHz laser cavities have been built up and amplified. A stable and robust operation for both frequencies was obtained and the experimental measurements have been found to match the theoretical predictions. Enhanced environmental stability has been achieved using a cavity temperature control system and an antivibration enclosure, ending in a robust and marketable prototype.

3.1 Theoretical Model

Laser mode-locking is the best technique to achieve ultra-short pulses with a temporal width of a few ps or less. For this purpose, one must establish

a rigid phase relation among the many longitudinal modes which can exist in a laser cavity of a certain length. When this length is short (< 0.2 m), gain conditions for laser emission, which imply high values for both pump absorption and emission cross section, are difficult to meet. Additionally, low and anomalous net dispersion values are required to achieve a solitonic regime, which is needed in this kind of lasers. There is no consolidated theoretical model to predict the necessary parameters for a stable mode-locking emission in ultra-high frequency cavities (1.0-10.0 GHz). The aim of this work is to provide a method to predict the requirements that a laser cavity must meet to achieve a stable passively mode-locked emission regime in all-fiber laser cavities of short cavity length (20.0 cm-2.0 cm).

In order to reach passive solitonic mode-locked stable emission an option is to use a SESAM as the saturable element inside the cavity. The SESAM considered in our model and used to experimentally assemble the laser is consider a fast type one, with a recovery time of 2 ps, a modulation depth of 37 % and a saturation fluence of 40 $\mu s/cm^2$. For a detailed theoretical and analytical analysis of SESAM use in the development of mode-locked lasers see [47–50].

Considering the gain conditions that the laser cavity is expected to need, and since the required emission wavelength is located in the telecommunications band C, a fiber doped with Erbium and Ytterbium has been chosen for the theoretical model. This double doping is performed to achieve higher pump absorption (> 300 dB/m) through the ytterbium [51], to improve the efficiency of the erbium emission, located around 1550 nm.

Figure 3.1 shows the laser architecture used in the theoretical model and the experimental set up used to compare and validate the results of the theoretical model. It is a mode-locked, polarization maintaining (PM, as the model works with a single polarization), Fabry– Pérot threshold fiber cavity. The active fiber has been directly connectorized to minimize transitions and polarization changes inside the cavity.

A laser diode (LD, 915 nm / 980 nm) was used as pump[1]. The light from the LD was inserted into the laser cavity through a dichroic mirror (DM) coated on the FC/PC connector of the common port of a standard single-mode 915/1550 nm polarizer wavelength division multiplexer (PWDM), which couples the pump to the laser cavity. A second FC/PC connector attached directly to the active fiber of the cavity is coated with a DM that has a reflectance of 99 % at 1550 nm, and a transmittance of more than 90 % at $900 - 1000$ nm. The DM is positioned between the two flat connectors. The active fiber is a highly Erbium and Ytterbium co doped PM fiber (OFS YPC23401) of length L with an anomalous dispersion of approx. 16 $ps/nm/km$ at 1550 nm. The end of the active fiber is attached to another FC/PC connector. A Batop InGaAs SESAM with a modulation depth, saturation fluence and recovery time of 37 %, 30 $\mu J/cm^2$, and 2 ps, respectively, was butt coupled to the FC/PC connector.

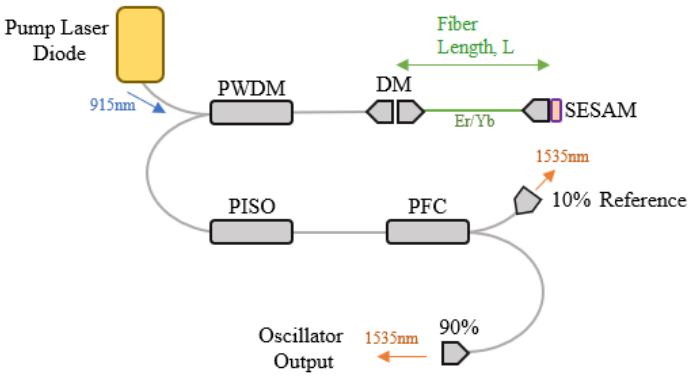

FIGURE 3.1: Oscillator internal structure. PWDM: polarizer wavelength division multiplexer; DM: dichromic mirror; SESAM: semiconductor saturable absorber mirror; PISO: polarizer isolator; PFC: polarizer fiber coupler.

The laser light (1550 nm) emitted from the cavity passes through the DM

[1]915 nm pumping was used in long cavities (1.0 GHz and 2.0 GHz) because the absorption at 980nm was too high and the pump light was completely absorbed in the first third of the cavity, causing a signal re-absorption and a negative gain regime.

and is extracted from the 1550 nm port of the PWDM. A PM single mode polarizer isolator (PISO) was fusion-spliced to the 1550 nm port of the WDM to protect the cavity from back-reflections and guarantee its long term stability. Finally, a 90:10 standard single-mode PM polarizer fiber coupler (PFC) was fusion-spliced to the output port of the isolator, allowing multiple measurements to be carried on simultaneously. This experimental setup enables an easy modification of the cavity to go through a full study of different fiber lengths, thus different repetition rates (10 cm/10.0 GHz, 4.7 cm/2.2 GHz and 1.0 cm/10.0 GHz) [2].

Real and accessible elements have been used to build the theoretical model. As a result, the modeled cavities are easy to manufacture so that they can evolve into a commercial laser prototype as simple as possible.

In order to numerically model the emission properties of our fiber laser, pulse propagation in the laser cavity is computed by solving the Non-Linear Schrödinger Equation (NLSE) ((3.1)) using a standard symmetrized split-step Fourier method algorithm [44]

$$\frac{\partial}{\partial z}A(z,T) = (\hat{L}+\hat{N})A(z,T) \tag{3.1}$$

$$\hat{L} = -\frac{\alpha}{2} + \frac{g}{2} - \frac{i\beta_2}{2}\frac{\partial^2}{\partial^2 T} + \frac{\beta_3}{6}\frac{\partial^3}{\partial^3 T} \tag{3.2}$$

$$\hat{N} = i\gamma \mid A(z,T) \mid^2 \tag{3.3}$$

(3.1), is a crucial equation in a fiber transmission system. It describes the propagation of the slow-varying envelope $A(z,T)$ of a single polarization of the scalar electric field of an optical pulse normal to its propagation axis.

[2] The oscillator is built using a Fabry-Pèrot structure. This means that the length of the fiber and the length of the cavity are different concepts and are related to each other as $Length_{cavity} = 2Length_{Fiber}$

z is the spatial coordinate along the fiber length and T is a group velocity moving-frame time defined as $T = t - \beta_1 z$, with t being the absolute time and β_1 being the inverse of the group velocity. $\hat{L}$ is a linear operator that accounts for gain, losses and dispersion of the optical fiber and $\hat{N}$ is a nonlinear operator that governs the effect of fiber nonlinearities on pulse propagation. Regarding the $\hat{L}$ and $\hat{N}$ operators, α is the fiber loss coefficient, g is the signal gain (dependent on pump power and wavelength), and β_n are the n-order group velocity dispersion parameters. In (3.3), we have only considered self-phase modulation (SPM) through the nonlinear parameter γ of the fiber. More complex nonlinear effects are neglected in the simulations. In [52] it is described the complete mathematical process to correctly model a solitonic passive mode-locked laser.

The key point to characterize the conditions for a stable mode-locked emission is the gain equation. To apply it in a more realistic scenario, a dependence in z-position has been considered. From [52] we can extract the following:

$$g(\lambda, z) = \Gamma N_t \sigma_{em}(\lambda) \frac{\frac{P_p(z)}{P_P^{th}} - \frac{\sigma_{abs}(\lambda)}{\sigma_{em}(\lambda)}}{1 + \frac{P_p(z)}{P_P^{th}}} \frac{1}{1 + \frac{P_S}{P_{sat}^*}(z)} \tag{3.4}$$

In (3.4), Γ and N_t are the estimated overlap factor between mode field and erbium dopant distribution and the total ion density, respectively. Parameters $\sigma_{abs}(\lambda)$ and $\sigma_{em}(\lambda)$ represent the wavelength-dependent absorption and emission cross-sections of the active fiber. P_S denotes the average pulse power, calculated as $P_S = E_P / T_R$, with E_P being the energy of the pulse and T_R being the cavity round-trip time. P_{sat}, P_P^{th} and P_{sat}^* are the intrinsic saturation power of the active medium, the pump power threshold (the pump power for which the ground and upper populations are equal) and the effective saturation power of the fiber. The mathematical expression used to characterize P_{sat}, P_P^{th} and P_{sat}^* and its usage to describe passive mode-locked

lasers emitting in a solitonic regime is elaborated in detail in [52]. (3.4) relies on a quasi-two level system valid to describe erbium doped systems. The ytterbium co-doping leads to a significant increase in the conversion efficiency of the erbium fibers, which is caused by a decrease in the erbium ion clustering [53]. The theoretical model has been adapted using the erbium/ytterbium co-doped fiber pump wavelength absorption value given by the manufacturer and increasing accordingly the cross-section (absorption and emission) values of the fiber to match the high conversion efficiency given by the ytterbium.

Regarding the SESAM effect in the numerical calculation, it was evaluated as an insertion loss dependent on the pulse intensity as done in [54]. The equation describing the temporal response of the intensity dependent losses in the SESAM, $q(t)$ is the following:

$$\frac{\partial q(A(z,t))}{\partial t} = -\frac{q - q_0}{\tau_{SA}} - q\frac{|A(z,t)|^2}{E_{SA}} \tag{3.5}$$

In (3.5), $A(z,t)$ is the slow varying component of the electromagnetic field of the signal, q_0 is the modulation depth, E_{SA} the saturation energy, and τ_{SA} the recovery time.

Table 3.1 shows the values used in the simulations of this work to adapt the theoretical model to GHz repetition-rate cavities.

The performance of the oscillator has been completely simulated and the results experimentally validated. As an example, figure 3.2 shows the calculated stable mode-locked pulse formation in our laser system corresponding to the laser architecture described in figure 3.1 for the 1.0 GHz cavity (top) and for the 2.2 GHz cavity (bottom). Evolution of both the spectra and the time full width at half maximum (FWHM) of the output pulses are depicted in the insets. Stability of both parameters is reached after few hundreds of round trips, when the initial random noise input is

TABLE 3.1: Simulation Parameters

Parameter	Value
Resolution in z	0.3125 cm
Resolution in λ	0.3 nm
Resolution in t	31 fs
SESAM non-saturable losses	15 %
SESAM recovery time (τ_{SA})	2 ps
SESAM saturation fluence	40 $\mu J/m^2$
SESAM modulation depth (ΔR)	37 %
Pump wavelength	915 nm / 980 nm
Signal wavelength	1535 nm
Active fiber pump absorption at 915 nm	355 dB/m
Active fiber pump absorption at 980 nm	600 dB/m
Effective area of the laser mode (A_{eff})	60.8 μm^2
Average second-order dispersion (β_2)	-0.015 ps^2/m
Average third-order dispersion (β_3)	0 ps^3/m
Average nonlinear parameter (γ)	2.7 $(W * km)^{-1}$

mode-locked into a stable pulse. Pulse width is 2.1 ps for the 1.0 GHz cavity and 1.1 ps in the 2.2 GHz case. As the length of the active fiber of the cavity changes, so does the net dispersion of the oscillator, which leads to different resulting pulses. According to the spectral width obtained, the Fourier transform of the 1.0 GHz cavity gives a minimum pulse of 1.3 ps and the 2.2 GHz cavity, a minimum pulse of 1.0 ps, obtained from a spectral FWHM of 2.0 nm and 2.5 nm respectively. According to this, the obtained results are consistent with the expected case.

A 10.0 GHz cavity (of 1.0 cm fiber length) was tested under the same pumping conditions, modeling also the co doped Erbium/Ytterbium fiber. The algorithm did not converge because the short active length of the cavity did not provide a proper positive gain regime. From this point onwards, some modifications were required to reach the proper emission regime. The first one was to model a 980nm pump to exploit the fact that the absorption of

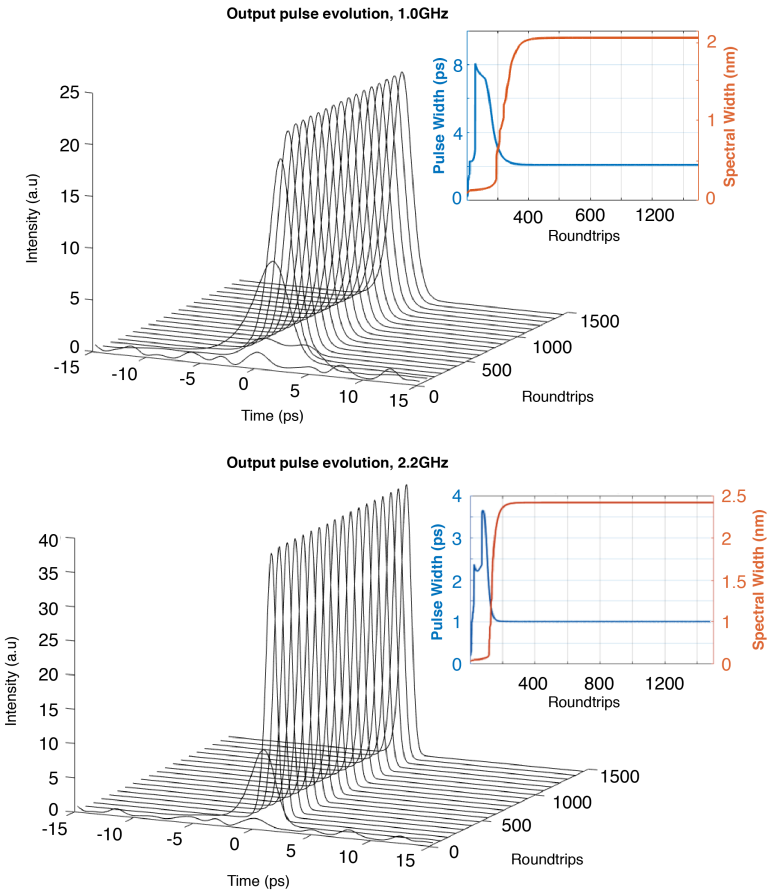

FIGURE 3.2: Calculated stable mode-locked pulse formation regime corresponding to the setup described in figure 1. (top) 20.8 cm cavity, 1.0 GHz rep. rate. (bottom) 9.6 cm cavity, that corresponds with 2.2 GHz rep. rate

the active media is higher for this wavelength (355 dB/m at 915 nm versus 600 dB/m at 980 nm). With a cavity absorbing more pump power, the required gain conditions should be easier to reach. The convergence test that contemplates these conditions can be seen in Figure 3.3 (top). As the image shows, a 980 nm pump wasn't enough to achieve a convergence in the algorithm. To reach a theoretical convergence, the gain of the cavity must be improved either by increasing the pump power or by increasing the emission cross-section of the active media.

In Figure 3.3 (top) a pulse evolution for 10.0 GHz can be observed. Despite the simulation converging, the values of pump power ($> 1\ W$) are out of the experimental possibilities as the SESAM can't hold such a high pump power and there is no commercial fiber matching the emission cross-section requirements. However, these simulations show that a 10.0 GHz cavity is buildable if the architecture adapts to its necessities.

The following is a full analysis for different frequencies, to study and predict the ideal conditions for mode-locked emission and transfer them to real prototypes. Fixing the laser architecture (same SESAM, same active fiber, same dichroic mirror), convergence at different lengths of the cavity has been studied, those being 20.8 cm (1.0 GHz), 9.6 cm (2.2 GHz), 4.0 cm (5.0 GHz) and 2.0 cm (10GHz). For each of these frequencies, a complete sweep has been performed by varying the pumping power and recording key parameters: spectral width, temporal width, and average power.

Figure 3.4 shows the spectral width as a function of the pump power at convergence of the simulations. When the convergence gives a near-to-zero spectral bandwidth, there is no stable mode-locking emission. Stable emission starts when the width curve becomes monotonous and shows a smooth evolution. To estimate the pump power threshold for stable mode-locked emission for each of the frequencies the pump power where the slope of the derivative is 45 ^{o} has been used, being: 112 mW@1.0 GHz, 142 mW@2.2 GHz, 257 mW@5.0 GHz and 693 mW@10.0 GHz.

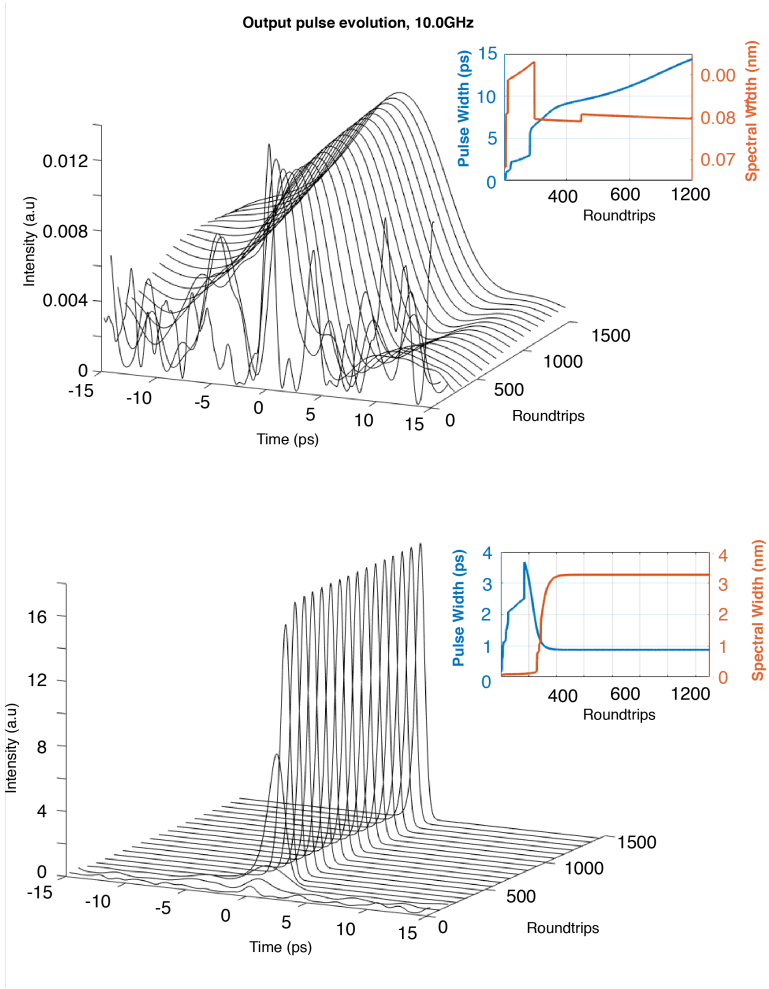

FIGURE 3.3: Calculated mode-locked pulse formation regime for a 1.0 cm cavity. (top) 980 nm pump wavelength, gain conditions and pump power same as those for 1.0 GHz and 2.2 GHz simulations ($\sigma_{em} = 51\ pm^2$) (bottom) 980 nm pump wavelength, emission cross-section three times higher than in the 1.0 GHz and 2.2 GHz simulations($\sigma_{em} = 150\ pm^2$).

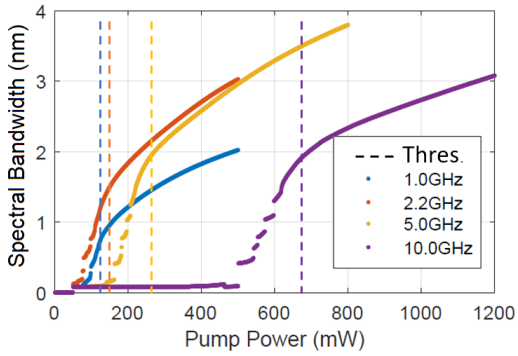

FIGURE 3.4: Spectral bandwidth after the convergence of the algorithm for different frequencies of the cavity. The threshold power for stable mode-locking emission is represented by a vertical dotted line.

Figure 3.5 shows temporal width (top) and average output power (bottom) as a function of the pump power after the convergence of the simulation for different frequencies of the cavity. For all frequencies the pulse time width at convergence is similar, about 2 ps. This can be easily explained by considering the key factors that determine the duration of the output pulses in mode-locked cavities which are both the net dispersion and three SESAM parameters: relaxation time (τ_{SA}), fluence and modulation depth (ΔR). However, they do not affect the pulse width as the SESAM is the same for all cases. On the other hand, to calculate the net dispersion of the cavity, the group velocity dispersion of the fiber (D) can be estimated as $D = -16\ ps/nm/km$. Despite the difference in relative value between the lengths of the cavities, from 20.8 cm to 2.0 cm, the net value of the dispersion barely changes (3.4 fs/nm for 20 cm and 0.32 fs/nm for 2.0 cm), resulting in pulses of similar temporal width.

Looking at the average output power, it is observed that for the higher frequency cavities (5.0 GHz and 10.0 GHz), the net gain is lower, so the efficiency is smaller. This can also be seen in figure 4.12, in which the emission threshold for high frequency cavities is also higher, 110 mW for 1.0

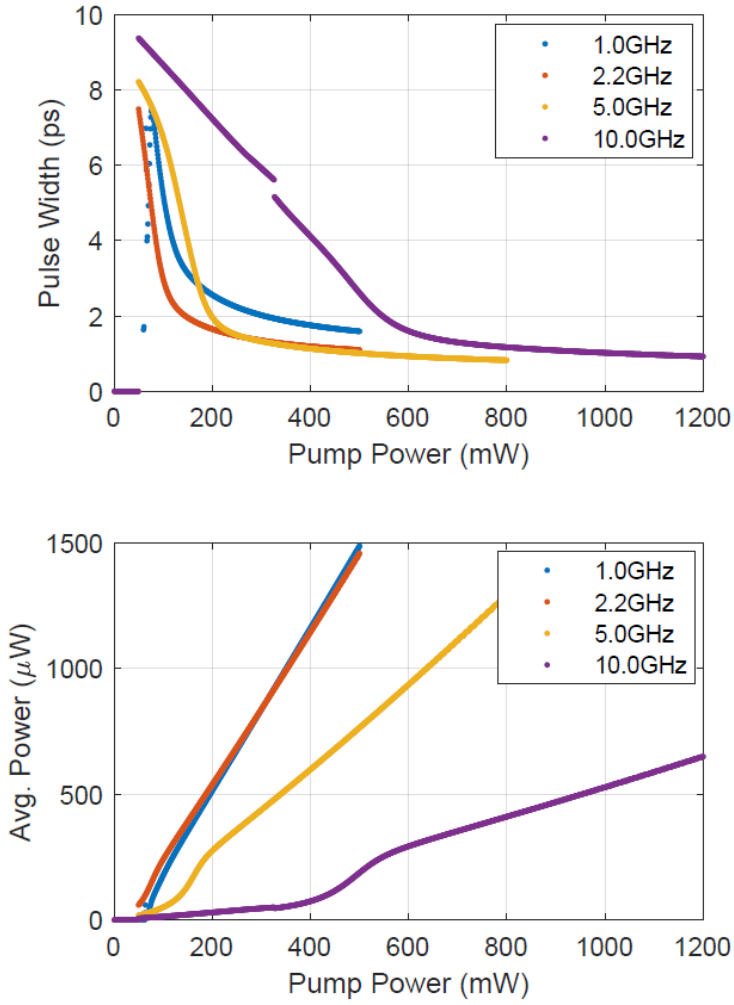

FIGURE 3.5: Temporal width (top) and Average Output Power (bottom) as a function of the pump power after the convergence of the algorithm for different frequencies of the cavity.

GHz and more than 600 mW for 10.0 GHz.

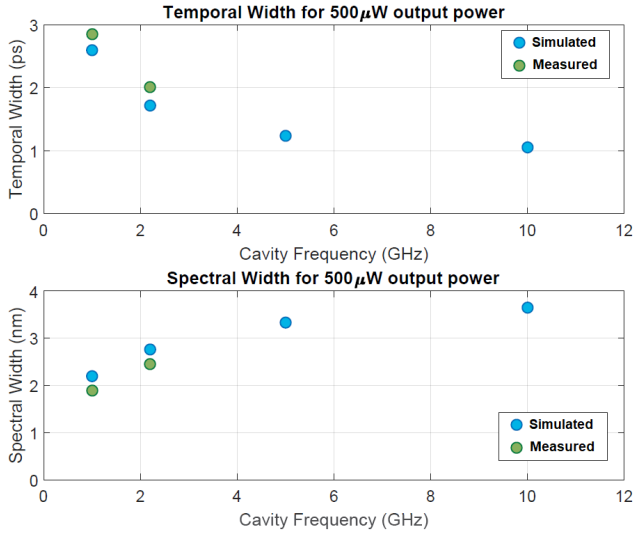

FIGURE 3.6: (top) Blue : Temporal width for different frequencies when the cavity average power output is 500 μW. Green : Measured temporal width after the amplification stage. (bottom) Spectral width for different frequencies when the cavity average power output is 500 μW. (bottom) Spectral Width for different frequencies when the cavity average power output is 500 μW.

The target applications of this work need an average output power greater than the obtained for the cavities (50-1000 μ W). To achieve the correct power specification (>100 mW) by amplification while maintaining a correct signal to noise ratio (SNR) (>27 dB), the seed average power to the amplifier must be in the order of magnitude of hundreds of µW. Figure 3.6 illustrates a comparison between the simulated temporal and spectral width of each cavity for those conditions in which they emit 500 µW of output average power and the measured temporal and spectral width using an autocorrelator and a spectrum analyzer respectively. The sensitivity of the autocorrelator was not high enough to measure signals with an

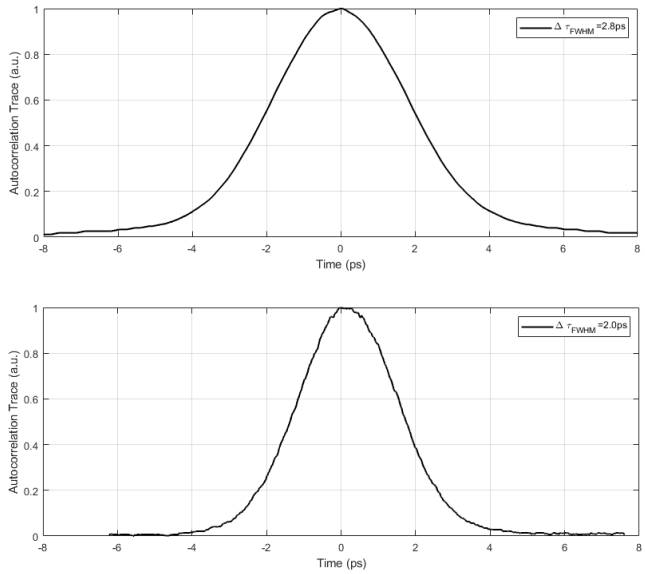

FIGURE 3.7: Autocorrelation traces measured using a Femtochrome FR-103XL autocorrelator. (top) For 1.0 GHz cavity when its average power output is 500 μW. (bottom) For 2.2 GHz cavity when its average power output is 500 μW.

average power of less than 1 mW at high frequencies. To obtain the autocorrelation traces, the pulses were measured after the amplification stage. Corresponding autocorrelation traces are shown in figure 3.7. The value of temporal width at FWHM for 1.0 GHz and 2.2 GHz cavities are 2.8 ps and 2.0 ps respectively. To obtain the values of temporal width, a deconvolution factor of 0.648 has been applied, assuming a $sech^2$ pulse shape.

There are two main reasons why the simulated values may differ from the measured ones. On one hand, due to the dispersion introduced through the fiber of the amplifier, the temporal pulse width increases from the oscillator to the amplification stage. On the other hand, dispersion resulted from Gires-Tournois interferometers (intrinsic to the SESAM functioning) has not been taken into account in the calculations. In long cavities, with a maximum frequency of several hundreds of megahertz, the dispersive effect of the SESAM is neglected. Once the cavity length is sufficiently short its value must be considered. The SESAM used to build the cavities in this work has a dispersion value that is strongly dependent on the wavelength from 2.74 fs/nm at 1525 nm to -2.74 fs/nm at 1560 nm, being 0.73 fs/nm at 1535 nm.

3.2 Experimental Results

In order to verify the validity of the theoretical study and achieve the implementation of a prototype of stable emission at GHz-range frequency, cavities of 1.0 GHz, 2.2 GHz and 10.0 GHz have been built. Furthermore, in order to perform measurements with a wider dynamic range and to meet the power needs of the target application, the output from the laser cavities has been amplified with a fiber amplifier (see figure 3.9).

3.2.1 Oscillator

Figure 3.8 (top) shows the measured optical spectrum (blue line) corresponding to a cavity with a repetition rate of 1 GHz and 140 mW of pump

power, where the red line shows the theoretical predicted spectrum. In the legend box, spectral FWHM (both measured and simulated) are shown. Figure 3.8 (bottom) shows the measured optical spectrum (blue line) corresponding to a cavity with a repetition rate of 2.2 GHz and 180 mW of pump power. Again, the red line shows the theoretical predicted spectrum. The high stability of this laser optical spectrum during long term stability measurements ($< 0.3\ dB/nm$ in a 4 h long MAX HOLD vs MIN HOLD measurement) relies on the all-PM-fiber cavity.

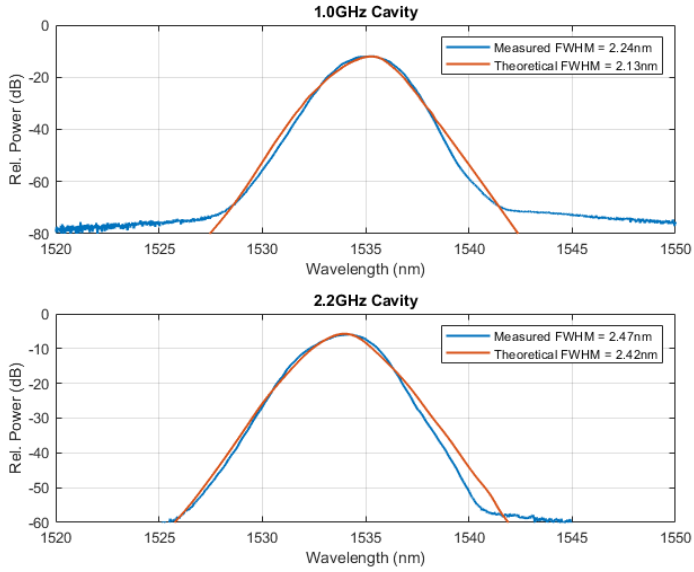

FIGURE 3.8: Experimental and simulated output optical spectrum of the mode-locked fiber oscillator in logarithmic scale for 1.0 GHz cavity (top) and 2.2 GHz cavity (bottom).

Same tests have been performed using the same laser architecture for 5.0 and 10.0 GHz cavities. As predicted by our simulations the required gain conditions were not reached. To have the conditions for an adequate gain regime, the pumping power should be increased to levels higher than the SESAM damage threshold, or a greater gain in the fiber should be achieved by making a non-commercial fiber design. High fundamental frequency

fiber mode-locked lasers (10 to 20 GHz) have been previously demonstrated using carbon nanotubes as a saturable absorbent [33]. However, in this work, the focus is getting optimized, robust, compact and repeatable GHz all-fiber lasers using commercial components.

3.2.2 Amplifier

After the oscillator stage a co doped Erbium/Ytterbium double cladding PM fiber amplifier has been included. Fig. 3.9 shows the amplification stage. A 976 *nm* laser diode (PD) delivering a maximum output power of 8 *W* was used as a pump. Light delivered from the PD was introduced into the first clad of the active fiber through the pump input of the power combiner (PC). This stage is shared for all cavities of different repetition rates.

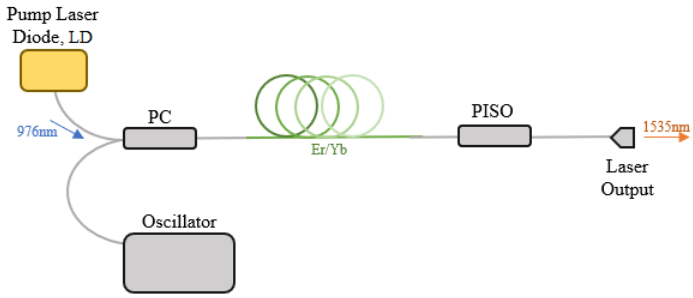

FIGURE 3.9: Fiber Amplifier structure.

The seed signal coming from the oscillator is introduced in the core of the active media through the main input of the PC. The PC is spliced to 1.5 m of double clad co doped Erbium/Ytterbium PM fiber (Nufern PM-EYDF-6/125-HE). A PM single mode isolator was fusion-spliced to the output of the active fiber to protect the cavity from back-reflections and guarantee its long term stability.

The performance of the setup to amplify the oscillator output signal has been analyzed. Figure 3.10 shows average power of the laser signal at the output of the amplifier vs. current driving the pump laser diode. As it can be seen in figure 3.10, the amplifier performance in terms of power is similar for 1.0 GHz and 2.2 GHz frequency inputs.

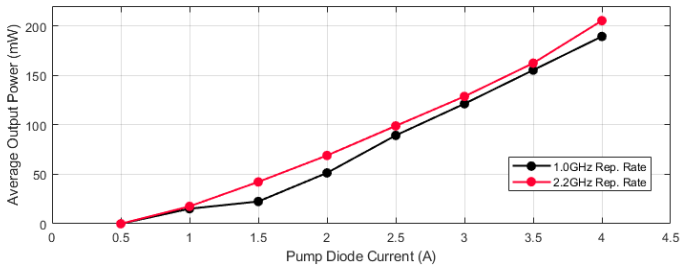

FIGURE 3.10: Amplifier output power vs pump diode current. 200 mW of output average power are reached at 4 A current of pump diode (at 4 A the pump diode gives 5 W of continuous wavelength signal at 976 nm). In black, amplified average output power for 1.0 GHz seed. In red, amplified average output power for 2.2G Hz seed.

It is possible to evaluate the gain factor in terms of power of the amplifier, using equation (3.6). The final product will have 100 mW of output power, which the value used for P_{out} in both cases. For the 1.0 GHz seed, $P_{in} = 185$ μW and for 2.2 GHz, $P_{in} = 355$ μW. The pulse energy is 18.5 pJ and 16.1 pJ respectively for 1.0 GHz and 2.2 GHz cavities.

$$\begin{aligned} Gain_{1.0GHz} &= \frac{P_{out}}{P_{in}} = 540 \\ Gain_{2.2GHz} &= \frac{P_{out}}{P_{in}} = 282 \end{aligned} \tag{3.6}$$

The long term stability of the laser working in a > 100 mW average power output regime has been studied. Figure 3.11 shows on the left ordinate axis a record of the average laser output power and on the right axis a record of

the calorimeter measuring head temperature, both measurements taken at 5-second intervals. The observable temperature variations are caused by uncontrolled environmental changes around the measuring head, specifically, the variation after 45 h happens because there was an increase in laboratory activity due to the end of the test. A standard deviation on the output average power of < 0.25 % is obtained. The high long term stability indicates that there is no SESAM degradation over time due to the high-absorption fiber chosen in the cavity that prevents undesired Q-switch laser modes and thermal damage caused by the pumping power in the SESAM. In short cavities, uncontrolled Q-switching instabilities can also cause permanent thermal damage in the SESAM leading to an unstable behavior [55]. For this reason, during the experiments the damage threshold of the SESAM (1 mJ/cm^2) was neither overcome by the pumping power nor by the power of the laser signal.

The all-PM design of both oscillator and amplifier forces the laser to work in a single-polarization regime which enhances the overall power stability. Similar curves have been obtained for both, 1.0 GHz cavity and 2.2 GHz cavity. The one shown in figure 3.11 corresponds to 2.2 GHz rep. rate.

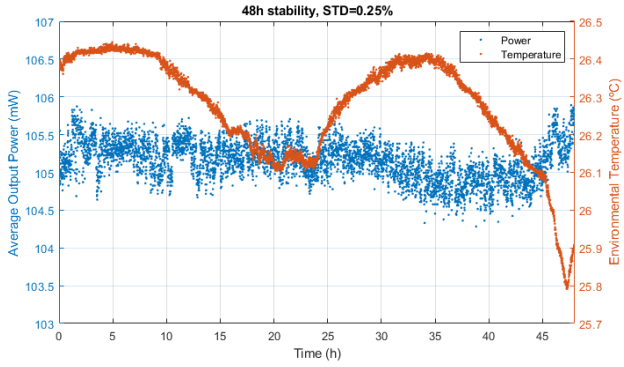

FIGURE 3.11: Stability of laser signal at the output of the amplifier for 48 hours.

The amplifier structure has been numerically simulated for the 1.0 GHz

seed using the pulse propagation engine described in section III but changing the clad pump absorption from 355 dB/m to 10 dB/m, the core signal absorption from 30 dB/m to 37 dB/m and the lengths of active and passive fibers. All the characterizing parameters (temporal width, average output power and spectral width) have been obtained theoretically and measured in the laboratory. The comparison between them can be seen in Table 3.2.

TABLE 3.2: Simulation Comparison

Parameter	**Theory**	**Measured**
Temporal Width FWHM (ps)	2.58	2.59
Spectral Width FWHM (nm)	1.55	1.52
Average Output Power (mW)	102.82	105.3

The very small differences between measured and simulated values indicate that the theoretical values of fiber length (1.5 m) and net dispersion (0.024 ps/nm) used in the simulation are an accurate approximation to the real values of these parameters. The oscillator output pulse from the previous simulation was employed as the initial seed in the amplifier stage. For the sake of completeness, a simulation of the output oscillator pulse through the amplifier stage in comparison with the oscillator output pulse is shown in figure 3.12. The temporal width stretching of the pulse after the amplification stage is due to the dispersion introduced by the amplifying fiber, and was estimated by experimental results, obtaining a value interval of 12-16 ps/nm/km.

Finally, the optical spectra at the output of the amplifier for different values of the pump current is shown in figure 3.13, for 1.0 GHz (top) and 2.2 GHz (bottom) signal seeds, respectively. As it is shown, the curve shape remains unchanged. This means that the peak power of the amplified pulses remains below the threshold of nonlinear effects. SNR is higher for higher frequencies (27 dB for 1.0 GHz and $>$ 40 dB for 2.2 GHz). The energy of the pulses at the input of the amplifier is similar (18.5 pJ for 1.0 GHz and 16.1 pJ for 2.2 GHz). Taking this into account the SNR improvement

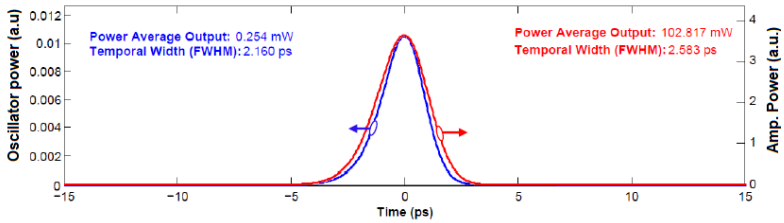

FIGURE 3.12: The blue line represents the oscillator output pulse; the red line represents the amplified oscillator output pulse.

must be caused by the increase in the frequency. The higher repetition rate implies less time of the active media being pumped with no signal going through, which translates into less amplified spontaneous emission (ASE) energy that can be observed in figure 3.13 (top) at $\sim 1543\ nm$.

From the point of view of the spectral domain, mode-locked-lasers are, indeed, optical frequency combs. Frequency tones of the comb are not seen in the spectra represented in fig. 3.13 because the spectrum analyzer resolution of 50 pm is insufficient to resolve tones of an FSR of 8 pm (1.0 GHz) or 18 pm (2.2 GHz).

To visualize the optical spectrum of the comb with detail, a Brillouin optical spectrum analyzer (BOSA) has been used. BOSAs are equipment that reach resolutions up to 0.08 pm, far better than regular optical spectrum analyzers [56]. Figure 3.14 (top) shows a 0.1 nm span, 0.08 pm resolution measurement of the optical spectrum at the output of the amplifier for the 2.2 GHz laser architecture. The 18 pm free spectral range between harmonics corresponds with the 2.2 GHz repetition rate, measuring $> 50\ dB$ SNR of spurious free spectrum between two consecutive tones. Figure 3.14 (bottom) shows the same measurement with a 2.0 nm span.

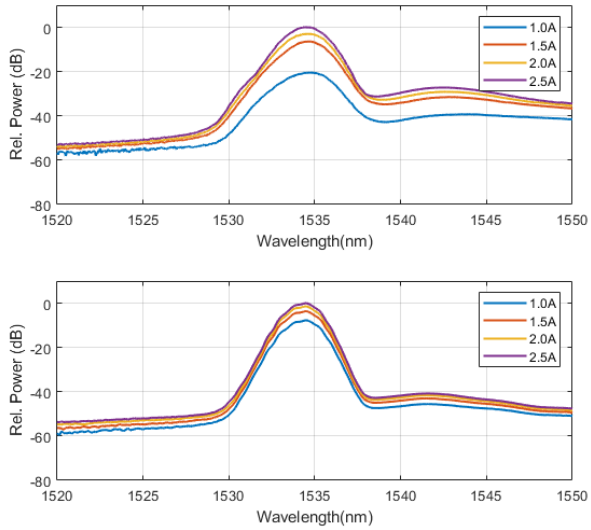

FIGURE 3.13: Spectra at the output of the amplifier for different values of the current applied to the LD. 2.2 A corresponds with 100 mW average output power.

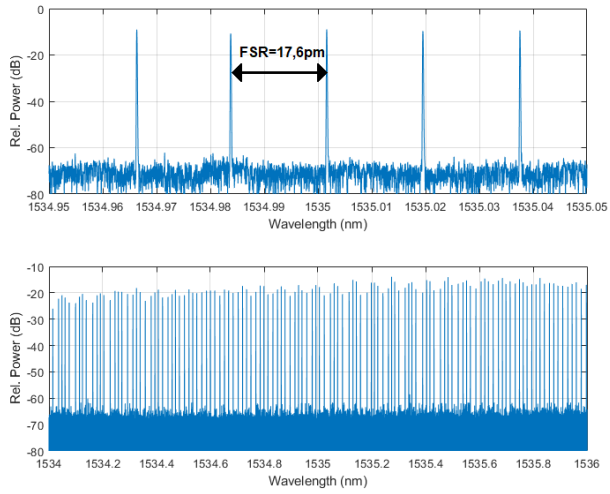

FIGURE 3.14: Optical spectrum of the 2.2 GHz amplified signal measured with a Brillouin Optical Spectrum Analyzer (BOSA). (top) Span of 0.1 nm and resolution of 0.08 pm. (bottom) Span of 2 nm and resolution of 0.08 pm.

3.2.3 Amplifier: Radio Frequency Domain

Radio frequency (RF) measurements of the photo detected oscillator output were carried out for both 1.0 GHz and 2.2 GHz frequencies. Figure 3.15 (A) shows the RF spectrum of the photo detected fundamental harmonic of the mode-locked laser (MLL) oscillator output corresponding to a setup with a FSR of 0.999 GHz, with a signal to noise ratio (SNR) of 65 dB at 500 kHz offset from the fundamental frequency.

Figure 3.15 (B) shows the RF spectrum of the photodetected fundamental harmonic of the mode-locked laser (MLL) oscillator output corresponding to a setup with a FSR of 2.231 GHz, a SNR of 76 dB at 500 kHz offset from the fundamental frequency. Figure 3.15 (C,D) shows a 25 GHz spanned radio frequency spectrum of both photo detected oscillator signals.

These measurements have been reproduced after the amplifier stage. As it can be observed in figure 3.16 (A,B), the RF spectra has a signal to noise

ratio (SNR) of $> 110\ dB$ at 500 kHz offset from the fundamental frequency. Figure 3.16 (C,D) shows the corresponding RF spectra with 25 GHz span. Figure 3.16 shows that this laser (at both repetition rates) has a very low phase noise, and it's free of spurious frequencies within the FSR between harmonics of the fundamental frequency. The signal-noise relation in the RF measures is better than the oscillator one because the higher power output allows to take advantage of the entire dynamic range provided by the measurement system consisting of photo detector plus spectrum analyzer.

These measurements were carried out with an Agilent electric spectrum analyzer (N9020A-526-EA3-B25-P26-PFR-N9075A-2FP-N9068A-2FP).

3.3 Prototype

Once the laser is working properly, the next step is to implement an optimal commercial mechanical design. The mechanical structure is organized by levels, one for the optical elements and the other for the system electronic control. A global sight of this structure is illustrated in figure 3.17.

As the target applications are focused on PADC and photonic radars, the laser must be stable regardless of the environmental conditions. A chest (figure 3.18) has been implemented to introduce the laser cavity and control its temperature with an accuracy of 0.1 ^{o}C using a Peltier cell. The chest is mounted on a platform with low frequency anti-vibration components (2-20 Hz), to further improve the resistance and stability of the equipment, since it is possible that as a photonic radar the laser is implemented inside transport means (Normative: MIL-STD-810 Rev. G-CHG-1).

The temperature control allows to optimize the stability of the output power and the temporal jitter, obtaining a drift in frequency lower than 15 kHz, as figure 3.19 shows. To analyze the frequency drift, a MAX HOLD measurement has been done. This measurement keeps always the maximum intensity value for each frequency. The width of RF spectrum corresponds

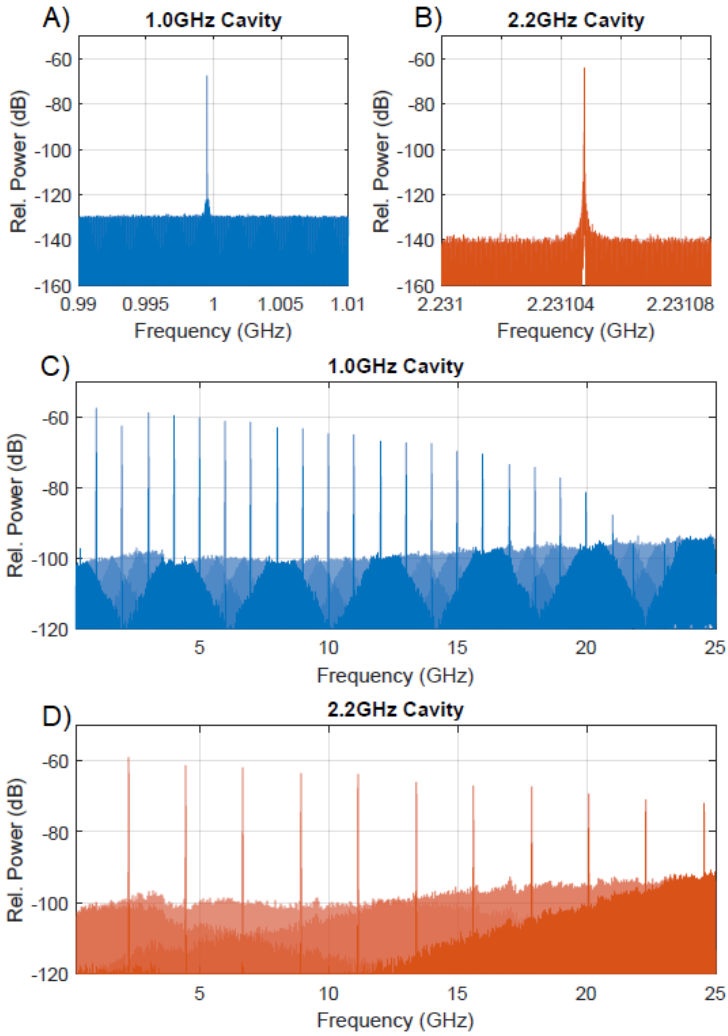

FIGURE 3.15: A,B: RF spectra of the photo detected fundamental harmonic of the mode-locked oscillator output corresponding to setups of 1.0 GHz and 2.2 GHz pulse repetition rates. A: fundamental harmonic, bandwidth of 1 MHz and 2 Hz resolution. B: fundamental harmonic, bandwidth of 10 MHz and 2 Hz resolution. C,D: corresponding RF spectra with 25 GHz span and 6.2 MHz resolution.

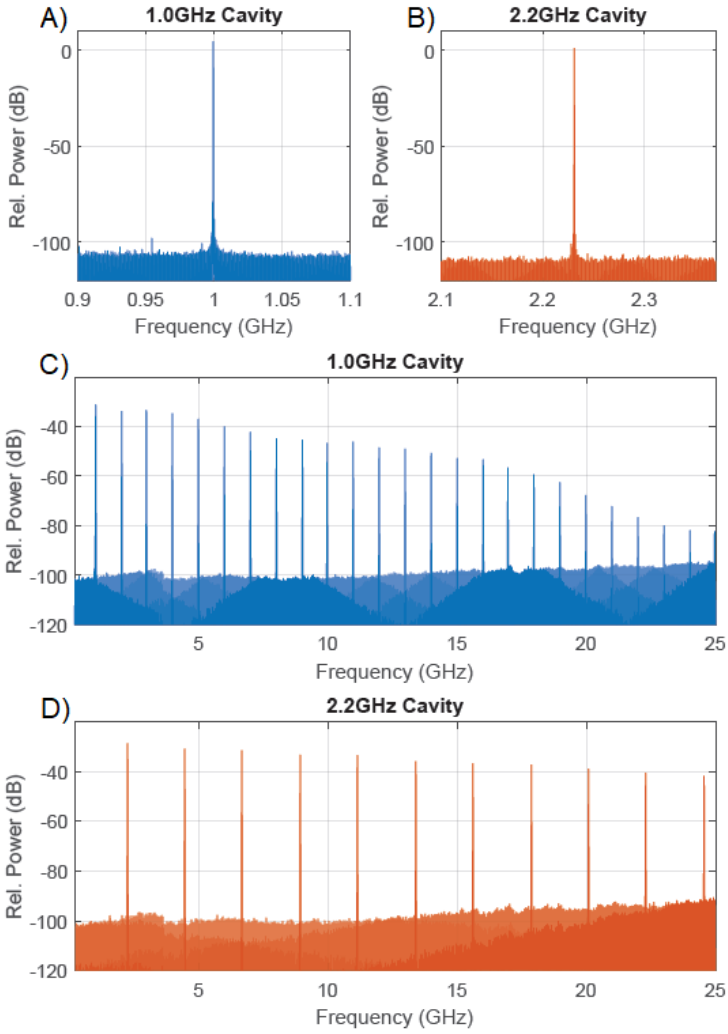

FIGURE 3.16: A,B: RF spectra of the photodetected fundamental harmonic of the mode-locked amplified laser with 100 mW of average power output corresponding to setups of 1.0 GHz and 2.2 GHz pulse repetition rates. A: bandwidth of 500 kHz and 2 Hz resolution. B: bandwidth of 500 kHz, 2 Hz resolution. C,D: corresponding RF spectra with 25 GHz span and 6.2 MHz resolution.

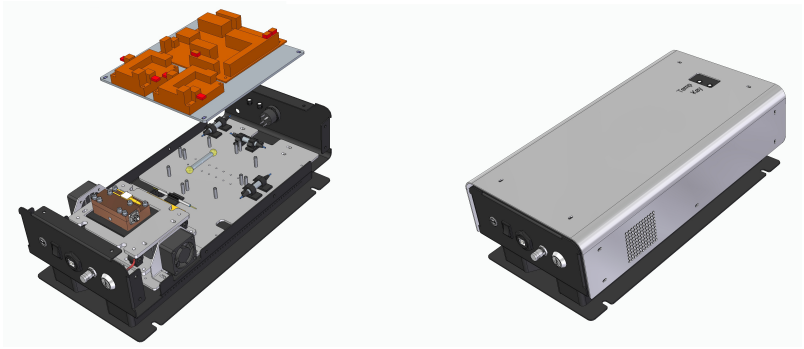

FIGURE 3.17: Left: Fiber optic laser structure situated in a compact layout. Right: closed structure. Output elements are situated in the back of the laser.

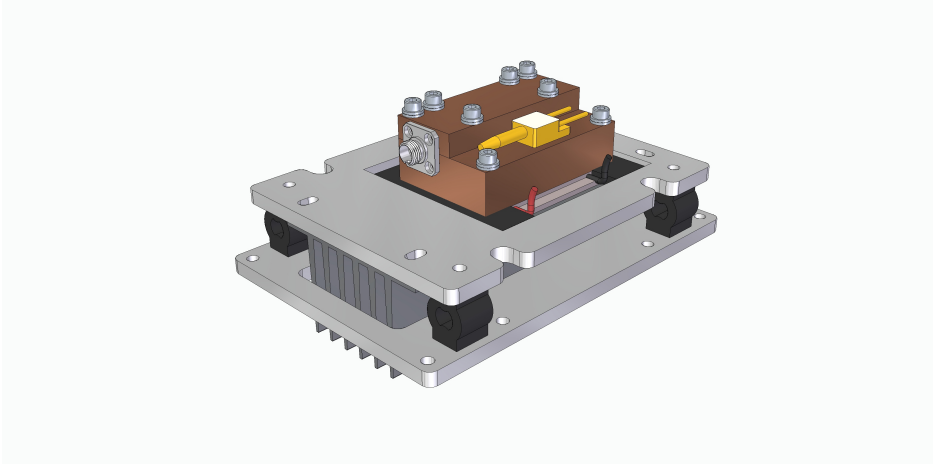

FIGURE 3.18: Temperature control and antivibration mechanical design to enhance the stability (average power and frequency drift) of the laser cavity

to the frequency drift of the laser signal. The cavity is controlled in temperature (0.1 ºC accuracy), minimizing the length changes due to thermal expansion ($< 0.05\ \mu m$). The control over the thermal expansion implies a controlled frequency drift ($< 15\ kHz$).

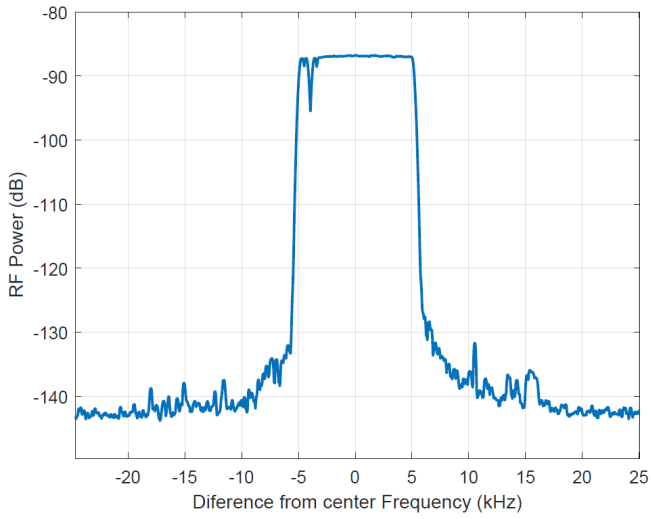

FIGURE 3.19: MAX HOLD measure of the amplified signal during 2 h of continuous emission. In the X axis the frequency drift from 2.2311 GHz is represented

The temperature control system allows to set the temperature of the cavity, controlling the laser emission frequency in a range of Fundamental Freq $\pm 300\ kHz$ selection. A central frequency emission curve for different stabilization temperatures is shown in figure 3.20 with measured drifts < 20 kHz for range [23-30] ºC.

From the need for a high frequency fiber laser that could be used as a source in applications of PADC and photonic radar and with the aim of making an optimal design of the laser cavity, a theoretical model based on the solution of the NLSE has been crafted. Using this theoretical model, a complete study has been made for cavities of 1.0, 2.2, 5.0 and 10.0 GHz based on an architecture manufactured with accessible components. By

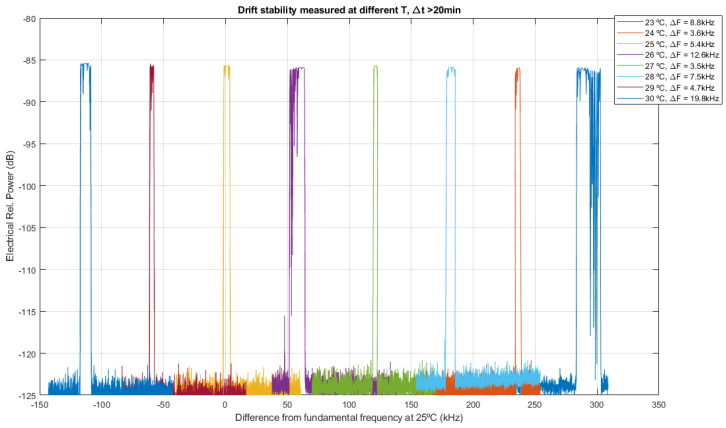

FIGURE 3.20: MAX HOLD measure made for different thermalization temperatures

recording values of interest (temporal width, average power and spectral width) the convergence conditions for stable laser emission solutions have been obtained.

The 1.0 and 2.2 GHz cavities have been implemented using a fully reliable ready-for-industrialization laser architecture. In order to reach the necessary specifications in PADC and photonic radar and to achieve measurements with a better dynamic range, an amplifying stage was added increasing the power up to 100 mW. The system has been completely characterized: optical spectra, RF spectra, pulse width, spectral stability and power output-power pump curves for each one of the frequencies. The spectra and pulse width obtained were consistent with the values obtained from the theory.

The higher frequency cavities (5.0 and 10.0 GHz) could not be built because the convergence occurred for pumping powers that were above the damage threshold of the SESAM. However, the consistency of the results for short cavities indicates that higher frequencies are feasible if adequate conditions are achieved. Some options would be using a pumping wavelength

that is better absorbed in the active fiber of the cavity (980 nm instead of 915 nm), using fibers with more absorption capacity and therefore more gain or a combination of both. The model offers the adequate parameters to build a correct laser architecture for 5.0 GHz and 10.0 GHz.

Compared to previous works on GHz-rate fiber frequency combs, we have achieved a stable cavity with enhanced spectral and power stability and durability for 1.0 GHz and 2.2 GHz. This relies on the singularities of our cavity: all-PM configuration and single type fiber cavity have been specially selected to not reach the thermal damage threshold of the SESAM as well as to engineer control on temperature and vibration.

Finally, a mechanical layout has been built to correct the instabilities caused by environmental changes: immunity to vibrations and temperature variations. For this, a copper chest has been built that has been assembled on a TEC system. Both parts, the TEC system and the chest, are located on an anti-vibration platform. This, together with the all fiber configuration make the laser a robust system suitable for PADC and photonic radar applications.

Chapter 4

Single-shot to MHz-Range Ultra-Short Fiber Laser System

This chapter addresses the design and development of low repetition rate ultrafast fiber lasers from single shot to tens of megahertz. However, reducing the fundamental repetition rate of a mode lock fiber lasers below the megahertz range and achieving stable emission is complicated. For this reason, a laser system is proposed, with a pulse selection module based on acousto-optic modulation that allows the repetition rate to be reduced without altering the other optical properties of the laser. In particular, a system developed to fulfil the specific optical excitation requirements of the Two-Photon Absorption Transient Current Technique, TPA-TCT, is described. The system is composed of three modules: a pulsed laser source, a pulse management module and a dispersion management module. Such modules are designed to provide the following configurability of the properties of the pulsed signal delivered at the output of the complete system: variation of the pulse energy between 10 nJ and 0.1 pJ, variation of the pulse repetition rate from 8.0 MHz to single shot and variation of the pulse duration between 300 and 600 fs. Besides, the system provides analysis elements such as reference signals, real-time measurement of pulse repetition rate and energy, autocorrelation of the pulse in the sample plane and

electro-mechanic commutation of the pulsed signal with response time below 2 ms.

4.1 Laser System

The system consists of three modules (see the block diagram in figure 4.1). The LPS module is the source of laser pulses, with a repetition rate of 8.2 MHz, central emission wavelength of 1550 nm and a pulse width below 300 fs. The LPM module is used to select the energy of the pulses (from below 10 pJ to above 10 nJ measured at the system output), the repetition rate of the pulsed signal (from 8.2 MHz to single shot) and to arbitrarily commute the laser emission at a response time of $\sim$ 1 ms. The D-SCAN module comprises a motorized time-domain compressor to select the temporal duration of the pulses in the range of 300 to 600 fs. Pulse characterization is performed preferably at the fundamental repetition frequency of the pulses (8.2 MHz). Once characterized, pulse energy, pulse repetition rate and pulse width can be tuned independently without altering other light properties.

4.2 Laser Pulse Source (LPS)

The laser pulsed source is composed of several stages, as shown in figure 4.2. First, a mode-locked fiber optic laser is used as seed to provide ultra-stable high quality pulses, of fundamental repetition rate of 8.2 MHz, FWHM duration of $<$ 300 fs and pulse energy of 1.5 nJ. The standard deviation of the average emission power achieved is less than 0.2 %. The chirped pulse amplification (CPA) technique [57, 58] is used to amplify the high quality signal avoiding unwanted nonlinear effects. The light delivered by the seed propagates in a stretcher stage through 40 meters of dispersion compensating fiber, stretching the temporal duration of the pulses up to more than 50 ps. To reach the energy levels required by the target application (TPA-TCT), $E_p > 10$ nJ, the output signal of the stretcher stage

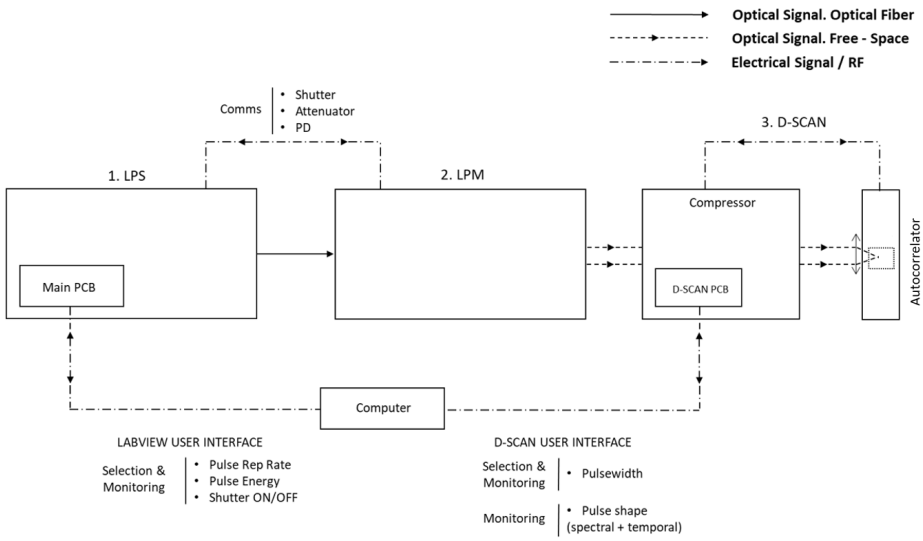

FIGURE 4.1: 1. LPS: Laser Pulse Source; 2. LPM: Laser Pulse Management Module; 3. D-SCAN: Compression module and characterization of the laser pulse by dispersion scanning. PCB stands for printed circuit boards, PD for photodetector.

is amplified through two stages. A first core-pumping amplification is carried out with an erbium-doped fiber to achieve a high quality signal with the necessary signal to noise ratio (SNR) for a proper noise free high power amplification. Then, with a clad-pumping amplification using an erbium-ytterbium codoped fiber, pulses of more than 150 nJ energy are obtained.

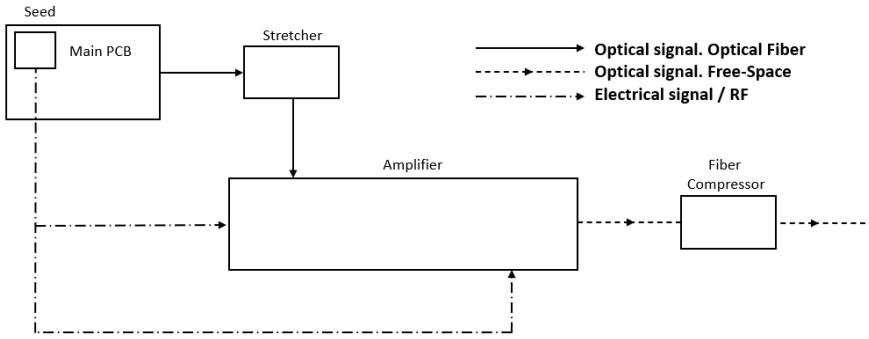

FIGURE 4.2: Fiber laser structure.

Once the pulses have the appropriate energy, they are compressed down to the femtosecond range avoiding unwanted nonlinear effects using a photonic band-gap hollow core fiber. The final laser output provides pulses of energy $E_p > 30$ nJ and duration $\Delta\tau_{FWHM} < 300$ fs . The properties of the pulsed signal after each stage are shown in table 4.1.

4.2.1 Oscillator

When designing the oscillator, the needs of the target application and the technical limitations of some elements that form the later stages of the laser have to be considered. On the one hand, the oscillator must provide a pulsed signal at 1550 nm, with high pulse-to-pulse stability in phase and in amplitude, high signal to noise ratio and sufficient energy per pulse for a subsequent noise-free amplification up to the level of the order of 10 nJ. On the other hand, the limited rise/fall time (80 ns) of the acousto-optic

Stage	E_p **(nJ)**	f **(MHz)**	P_{avg} **(mW)**	$\Delta\tau$ **(ps)**
Seed	1.54	8.2	12.6	0.219
Stretcher	0.61	8.2	5.0	51.7
Preamplifier	3.48	8.2	28.6	53.6
Amplifier	150.0	8.2	1230.0	51.4
Compressor	30.7	8.2	252.0	0.239

TABLE 4.1: Pulsed signal properties after the different stages of the laser pulse source (LPS).

modulator used in a later stage for pulse repetition rate down conversion, conditions the oscillator to work at repetition rates below 10 MHz. At a repetition rate of 10 MHz, the output average power of the oscillator for a noise-free amplification has been determined experimentally to be > 1 mW. Such low repetition rates are not common in fiber-optic passively mode-locked cavities, which are typically several tens or hundreds of MHz, since for their correct operation the net dispersion of the cavity must be close to zero which is easier to achieve the shorter the length of the cavity. Besides, the oscillator is designed to reach a stable emission regime autonomously (self-starting). Taking all this into account, three different setups for the optical cavity of the oscillator have been designed and tested (see figure 4.3).

All three configurations have been designed solving the non-linear Schrödinger equation (NLSE) with the split-step Fourier method [44, 59]. The mathematical development of the simulations used in the laser design process that we discuss in this work is explained in detail in [52]. From a theoretical point of view, the three configurations were viable. Configurations a) and b) had a lower pumping power threshold than configuration c): $\sim$ 80 mW in configuration a) and b) and $\sim$ 250 mW in configuration c). Uncontrolled pulse behavior of pumping power higher than 80 mW happened frequently in configurations a) and b). Configuration c), despite being more demanding in terms of pumping power, had a cavity net dispersion

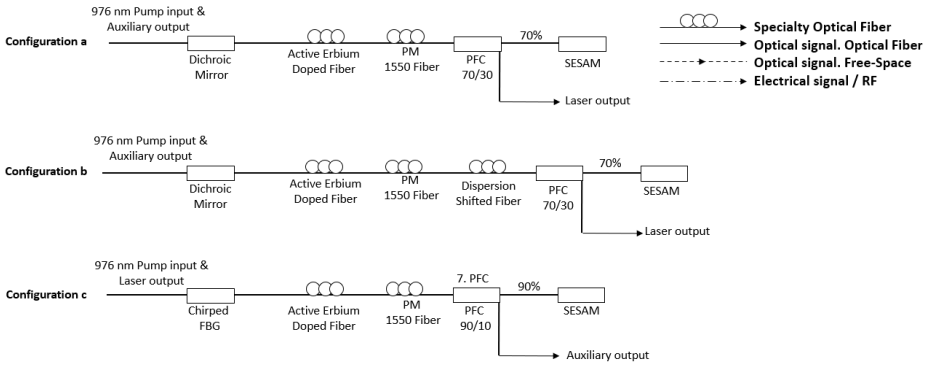

FIGURE 4.3: Different oscillator architectures that designed and tested. PM: Polarization Maintaining, PFC: Polarizer Fiber Coupler, SESAM: Semiconductor Saturable Absorber Mirror, FBG: Fiber Bragg Grating.

value closer to zero ($D_{net} = 0.012$ ps/nm).

The three cavities were tested experimentally. The mirrors of configuration a) are a SESAM (Semiconductor Saturable Absorber Mirror) and a dichroic mirror with reflectivity > 99 % in the 1500-1600 nm band and transmission > 99 % at pump wavelength. The active medium is a 60 cm length erbium-doped fiber with an estimated dispersion value of ~ 16 ps/nmkm and an emission band centered in 1550 nm. To extract the pulses and ensure that only a single polarization oscillates in the cavity, a 70/30 polarizing fiber coupler (PFC) is used. To obtain the required frequency (<10MHz), the cavity length has to be longer than 10.4 m, which, according to the Fabry-Pèrot configuration of the cavity, corresponds to a repetition rate lower than 10 MHz. This is achieved by adding meters of passive fiber (PM1550-XP, Coherent) with an estimated dispersion per meter of ~ 12 ps/nmkm. Configuration a) meets all the required specifications but presents a very unstable self-starting. To obtain a stable solitonic emission regime, a net anomalous dispersion close to zero is necessary. The excessive length of the cavity causes a net dispersion value of 0.13 ps/nm which is too high, resulting in an unstable and not easily repeatable emission regime. Stable

Parameter	Target	Conf. a	Conf. b	Conf. c
Emission Center Wavelength (nm)	1550	1560	1560	1550
Power Output (μW)	>1000	550	600	>12000
Repetition Rate (MHz)	<10	13.5	10.0	8.2
Net Dispersion (ps/nm)	<0.04	0.99	0.02	0.01
Self-Starting Consistency	Yes	No	No	Yes

TABLE 4.2: Oscillator target specifications and values obtained with each configuration.

emission is only achieved when the PM1550-XP fiber length is reduced down to 7.7 m or below, which corresponds to a $D_{net} = 0.1$ ps/nm and a pulse repetition rate of 13.5 MHz.

Configuration b) attempts to achieve an adequate dispersion regime introducing two meters of dispersion shifted fiber (PM2000D, Coherent). The dispersion value of this fiber is -50 ps/nmkm. Despite solving the dispersion mismatch, the small core diameter of the dispersion shifted fiber (Mode field diameter of 3-4 μm for PM2000D vs 9-10 μm for PM1550-XP) causes high losses in splices with the PM1550-XP ($> 95\%$), and a positive gain regime is not achievable.

In configuration c), the dispersion compensating fiber is removed and the dichroic mirror is replaced by a chirped fiber Bragg grating (CFBG). The CFBG has a reflectivity of 10 % centered at 1550 nm and introduces a dispersion of -0.120 ps/nm. The normal dispersion introduced by the CFBG induces the cavity to emit in a stable solitonic mode-locked regime. To compensate for the losses introduced by the low reflectivity of the grating, the PFC ratio has been modified to 90/10. In this configuration, the output with the highest average power is the output from the CFBG itself. The specifications obtained from the output of each of the settings are shown in table 4.2

Configuration c) is the one that best meets the specifications required by the TPA-TCT and by the technical limitations of later stages of the laser.

The results obtained with configuration c) and its complete characterization follow.

Figure 4.4 shows the laser setup of the passively mode-locked, polarization maintaining (PM), Fabry-Pérot cavity fiber laser. A 976 nm butterfly laser diode (LD) delivering a maximum output power of 300 mW is used as pump. The light delivered from the LD is launched into the linear cavity using a polarization maintaining wavelength division multiplexer (PWDM), a chirped fiber Bragg grating acts as reflector of the laser cavity, with a reflectance of 7 % at 1550 nm and a transmittance of 99 % at 976 nm. Besides, the CFBG introduces a normal dispersion of -0.120 ps/nm. To keep a high-quality solitonic pulsed regime, the net dispersion of the cavity must be anomalous (> 0) and close to 0. The CFBG is selected to compensate the dispersion introduced by the optical fibers in the cavity. Taking into account both dispersive elements, the net value is estimated to be $+0.010$ ps/nm from subsequent simulations. The laser cavity is composed of an active and a passive fiber, the length of which are calculated to obtain a repetition rate of 8.2 MHz. The active fiber is an erbium-doped PM fiber of 80 cm length (EFS 7/125, Coherent) and the passive fiber is a PM1550-XP fiber of 10 m length (Coherent). After the passive fiber, a 90/10 polarizing fiber coupler (PFC) is placed to have access to a 10% auxiliary output for synchronous measurements and security checks. A Batop InGaAs SESAM with modulation depth, saturation fluence and recovery time of 37 %, 30 μJ/cm^2 and 2 ps respectively, is introduced as second reflector at the end of cavity using a FC/PC connector. The laser output is the 1550 nm port of the polarizing wavelength division multiplexer (PWDM), which is connected to a polarizer isolator (PISO) to protect the laser cavity from back reflections that can cause instabilities and damage the laser.

Figure 4.5 (top) shows the measured optical spectrum corresponding to a cavity with a repetition rate of 8.2 MHz and pump power of 210 mW. The spectral bandwidth is 20.4 nm @10 dB. The optical spectrum was stable in long-term measurements, <0.3 dB/nm in a 4 h long MAX HOLD (Optical

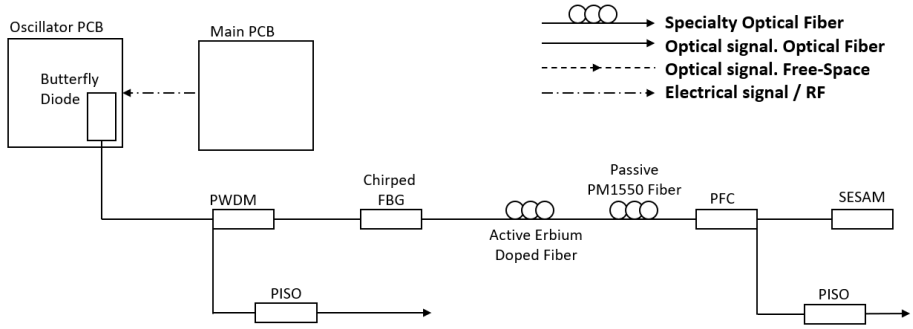

FIGURE 4.4: Oscillator structure. PCB: Printed Circuit Board, PWDM: Polarizing Wavelength Division Multiplexer, FBG: Fiber Bragg Grating, PISO: Polarizing Isolator, PFC: Polarizing Fiber Coupler, SESAM: Semiconductor Saturable Absorber Mirror.

spectrum analyzer keeping the higher signal value for each wavelength over time) vs MIN HOLD (Optical spectrum analyzer keeping the lower signal value for each wavelength over time) spectral measurement. The average output power was also very stable in long-term measurements, $<$ 0.5 % in a 4 h long average output power measurement . The pulse has been characterized with an autocorrelator (Femtochrome FR-103XL). The pulse shape and the FWHM temporal width (219 fs), both simulated and measured, are shown in figure 4.5 (bottom). The pulse width value is calculated from the autocorrelation trace assuming a $sech^2$ shape of the pulse. The average output power is 12.6 mW and the pulse energy is $E_p =$ 1.54 nJ.

4.2.2 Stretcher

The target application requires pulses of energy above 10 nJ. The fundamental repetition rate of the oscillator is 8.2 MHz, therefore, the target average power at the system output is 82 mW. Considering the losses introduced in the compression stage (>70 %), a gain of 20 dB is needed

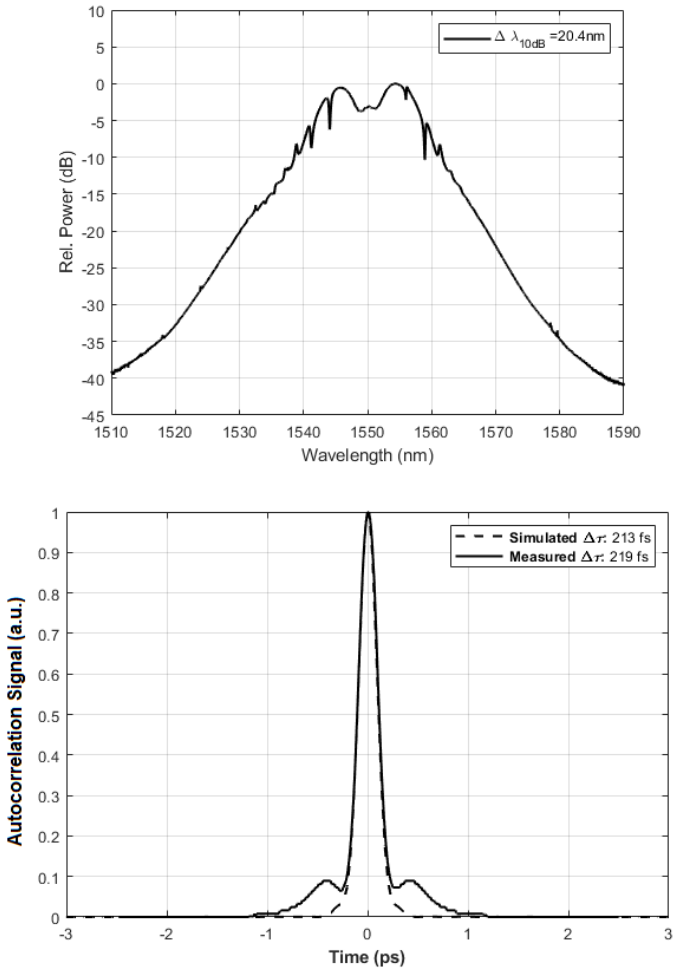

FIGURE 4.5: Oscillator optical spectrum (top) and autocorrelation trace (bottom).

(from 12.6 mW at the oscillator output to 1230 mW at the amplifier output). To achieve these values avoiding unwanted nonlinear effects that would worsen the temporal coherence of the pulse and the shape of the spectrum, the the chirped pulsed amplification (CPA) technique is used. The CPA technique consists in stretching the pulse before going through the amplifying stages in order to decrease the peak power of the pulses thus avoiding unwanted nonlinear effects during the amplification process. Once the power requirement is achieved, the pulse is recompressed through a linear medium. This technique is explained in detail in [60, 61].

The fibers in the oscillator and amplifier stages have anomalous dispersion. To form the stretcher, 40 m of a dispersion shifted fiber with a normal dispersion $D = -50$ ps/nmkm is selected (Nufern, PM2000D). Being stretched with normal dispersion, the pulse is compressed throughout the subsequent stages of the laser. In this way, the final compression stage is easier to construct, since the pulse at the output of the main amplifier is partially compressed. On the other hand, the pulse leaves the oscillator having suffered an anomalous net dispersion. When it propagates in a normal dispersion fiber, it crosses a zero of suffered net dispersion. At this point, a minimum of temporal width is reached and, consequently, a maximum in peak power that causes a spectral broadening due to self-phase modulation (SPM). The spectrum is coherently broadened up to a bandwidth of 40 nm @10dB, supporting a transform limited pulse width of < 300 fs in subsequent compression stages.

Figure 4.6 (top) shows the measured optical spectrum after a length of dispersion shifted fiber, $L_{PM2000D} = 40$ m. Spectral bandwidth @10 dB of 40.0 nm is shown in the legend. The autocorrelation trace and the FWHM temporal width (51.7) are shown in figure 4.6 (bottom). The average power output is 5.2 mW due to the losses in the fiber and the coupling between the core of the oscillator output fiber and the dispersion shifted fiber ($MFD_{PM1550-XP} = 8\ \mu m$ and $MFD_{PM2000D} = 4\ \mu m$). Pulse energy is $E_p = 0.61$ nJ.

Pulse evolution through the stretcher stage has been simulated solving

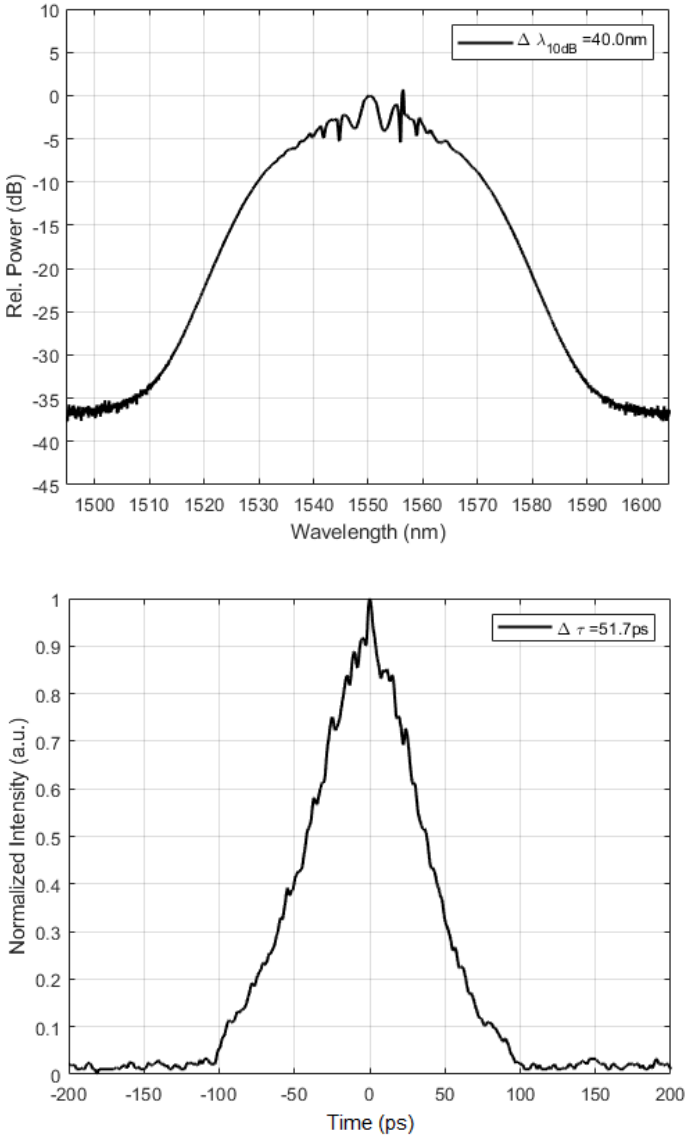

FIGURE 4.6: Optical spectrum at the output of the stretcher stage (top) and autocorrelation trace (bottom).

the Non-Linear Schrödinger Equation (NLSE) using a split-step Fourier based method that is developed in deep detail in [52]. The optical pulse obtained from the oscillator simulation has been introduced into 40 m of PM2000D. In figure 4.7, the theoretical results are compared to the autocorrelator traces obtained from the real pulses. The oscillator output pulse (figure 4.7,top) was employed as the initial seed in the stretcher stage. The small differences between measured and simulated values (< 3 % in the FWHM) indicate that the theoretical value for net dispersion in PM2000D fiber of - 60 ps/nm used in the simulation is an accurate approximation to the real value of the parameter.

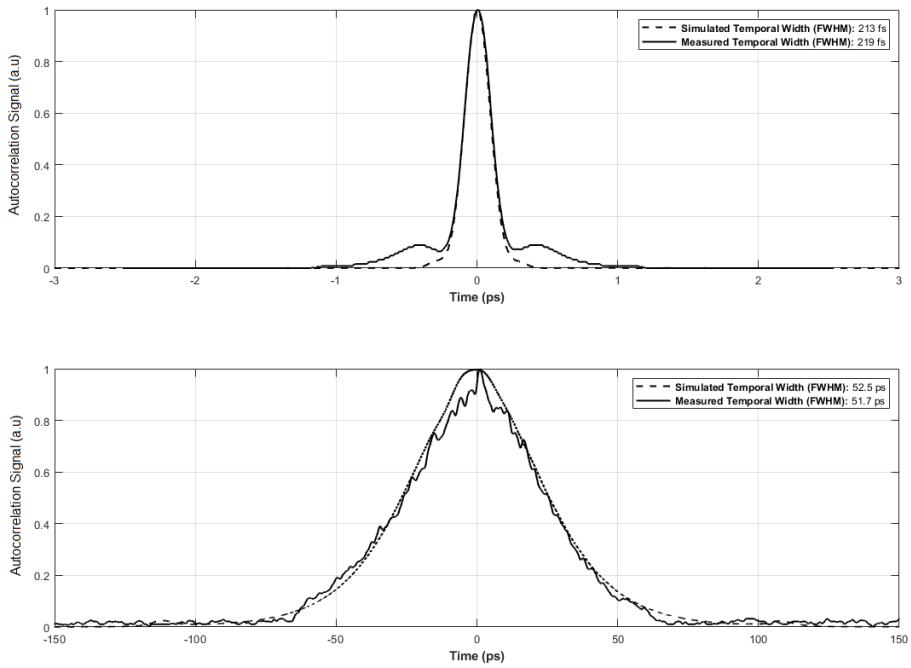

FIGURE 4.7: Simulated and measured autocorrelation traces of the input pulse to the stretcher (top) and the output pulse from the stretcher (bottom).

4.2.3 Amplifier

After the stretcher, a double stage amplifier is included, with the goal of providing an energy per pulse of > 10 nJ at the output of the full system. The structure of the complete amplifier is illustrated in figure 4.8.

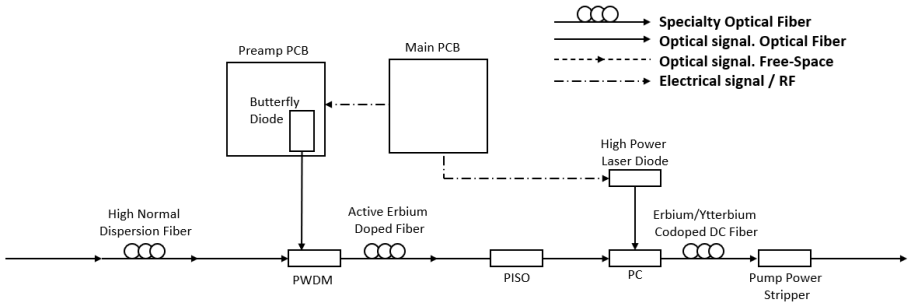

FIGURE 4.8: Amplifier structure. PCB: Printed Circuit Board, PWDM: Polarizing Wavelength Division Multiplexer, PC: Power Combiner, DC: Double Clad, PISO: Polarizing Isolator.

The first stage is based in core-pumping amplification using 50 cm of erbium-doped fiber (Coherent EFS 7/125). A 976 nm butterfly diode that emits a maximum power of 300 mW is used as a pump. The objective of this first stage is to achieve a power gain of around 10dB while maintaining a noise-free spectrum and stable pulsed emission. The spectrum and the autocorrelation trace are shown in figure 4.9. The average output power is 28.6 mW, the spectral bandwidth @10dB is 29.0 nm and the pulse duration at FWHM is 53.6 ps.

The second stage is based in clading-pumped amplification. The objective of this second stage is to achieve a power gain of around 15 dB. As an active medium, an erbium-ytterbium codoped double clad fiber - has been chosen (Coherent PM-EYDF-12/130). Double doping makes it possible to take advantage of the higher absorption efficiency that ytterbium has at 976 nm but using the erbium emission band centered at 1550 nm, which allows building a more efficient system to amplify signals at this wavelength.

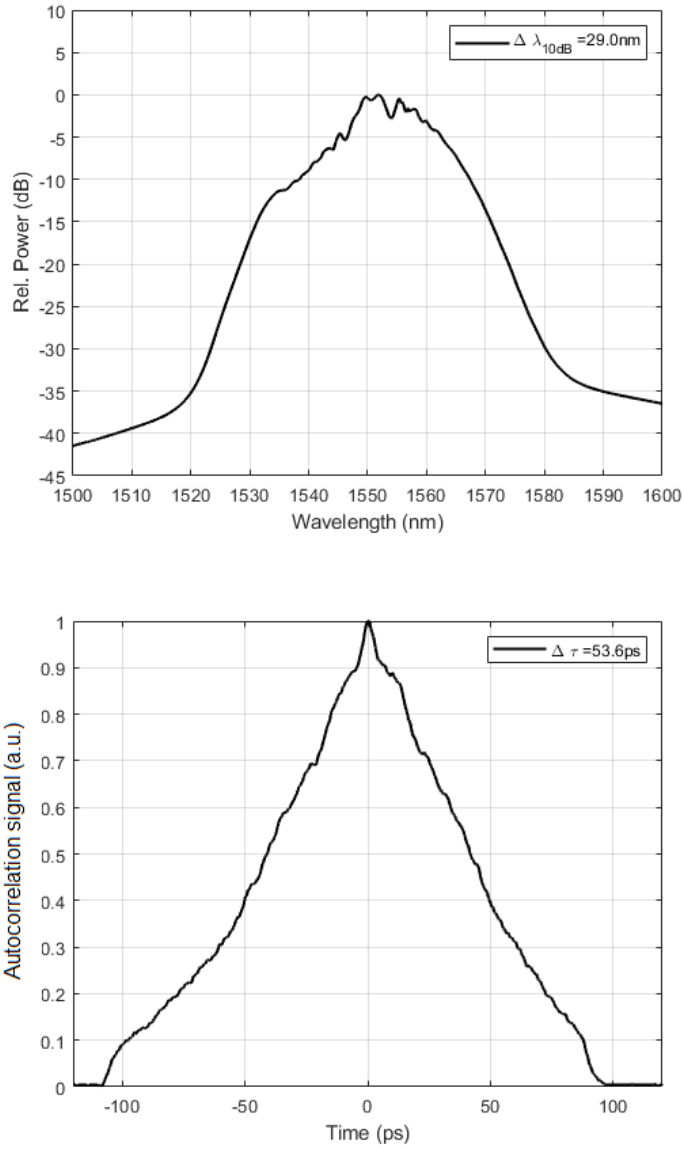

FIGURE 4.9: Optical spectrum of the first stage of the amplifier (top) and autocorrelation trace (bottom).

For pumping, a temperature stabilized 18 W diode has been used, which emits precisely at 976 nm thanks to wavelength stabilization provided by a volume Bragg grating placed at the output of the laser diode. During the experimentation process it was observed that a small variation in the wavelength of the diode due to changes in the environment temperature ($\sim 0.2 - 0.5$ nm) entailed a large instability (> 5 % in std. deviation during 4 h) of the pulse energy. Codoped fibers with erbium and ytterbium have a very sharp absorption peak centered at 976 nm, so small variations in the emission wavelength of the pump diode can translate into high instabilities of the energy of the pulse. After stabilizing the emission wavelength of the diode with the Bragg grating, this value was reduced to below 1 %.

A longer length, despite decreasing the pump power required, induced undesired non-linear effects. The desired power is achieved with 90 cm of active fiber and 4.4 W of pumping power. The spectrum and the pulse structure are shown in figure 4.10. The average output power is 1230 mW, the spectral bandwidth @10dB is 40.1 nm and the pulse duration at FWHM is 51.4 ps.

4.2.4 Fiber Compression

After the amplifying stage, a compression stage is implemented to compress the pulse without non-linear effects. The proposed solution is to use a photonic band-gap hollow core fiber (PBG-HC). The air core has a very low non-linear index so it avoids unwanted non-linear effects for the peak powers that are handled in this work (up to 100 kW). The photonic crystal structure is designed to obtain a flat dispersion curve with a value of $< +100$ ps/nmkm at 1550 nm.

The structure of the laser (oscillator, stretcher and amplifier) is entirely constructed with polarization maintaining elements. Hence, input to the PBG-HC fiber is linearly polarized. However, the PBG-HC fiber introduces different dispersion for each polarization mode, preventing the pulse to be compressed to its Fourier limit. This effect is known as polarization mode

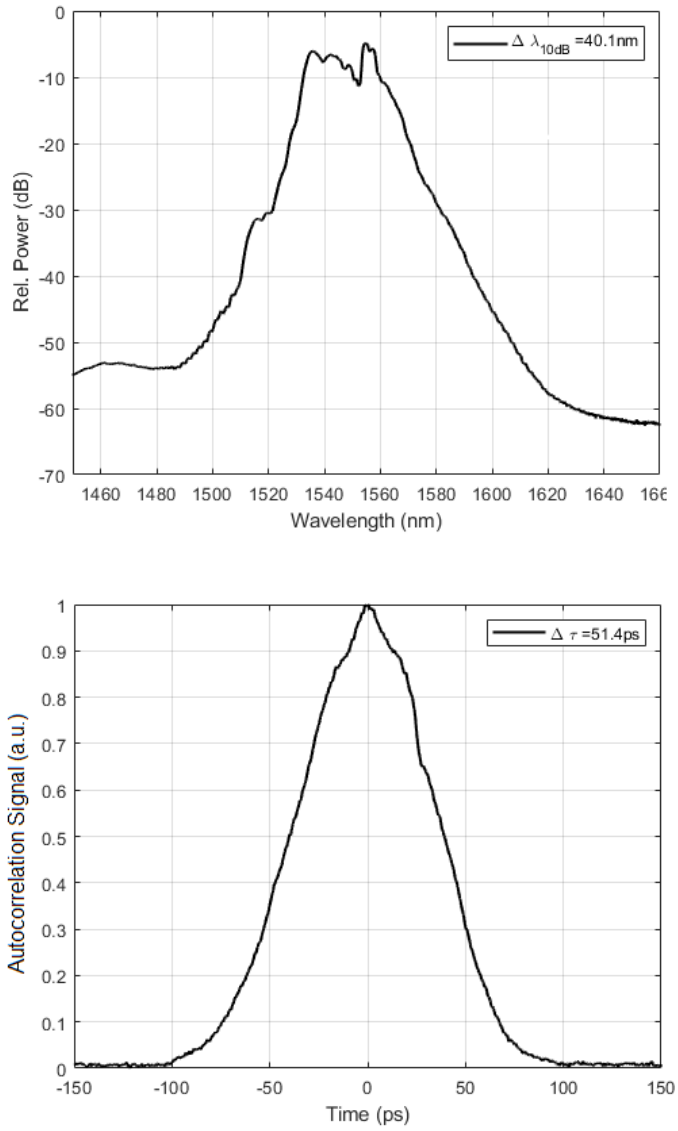

FIGURE 4.10: Optical spectrum at the output of the second amplifying stage (top) and autocorrelation trace (bottom).

dispersion (PMD) [62–64]. The solution implemented in this work is to introduce a Faraday rotator mirror at the end of the PBG-HC fiber. Faraday rotator mirrors take the output beam from a single-mode fiber and rotate the polarization state by 90 degrees before sending it back through the same fiber. By doing so, a Faraday mirror functions as a phase conjugate mirror and cancels out any birefringent effects the beam experienced along the forward path [65, 66]. To implement the Faraday mirror, a free space stage consisting of a polarizing beam splitter and a half wave plate is set up. This solution allows the linearly polarized light to be introduced directly into the PBG-HC fiber and to obtain the laser output with the polarization state rotated 90 degrees. The detailed design is shown in figure 4.11.

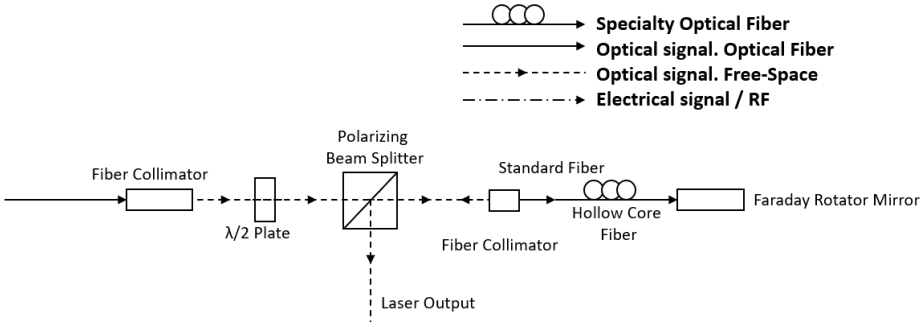

FIGURE 4.11: Optimized compressor design.

The compressor is composed of 19 m of PBG-HC fiber with anomalous dispersion of + 100 ps/nmkm and a fiber pigtailed Faraday rotator mirror (Thorlabs, MFI-1550). The spectrum and the autocorrelation trace at the output of the compressor are shown in figure 4.12. The average output power is 252 mW, the spectral bandwidth is 34.0 nm @10dB and the pulse duration at FWHM is 239 fs.

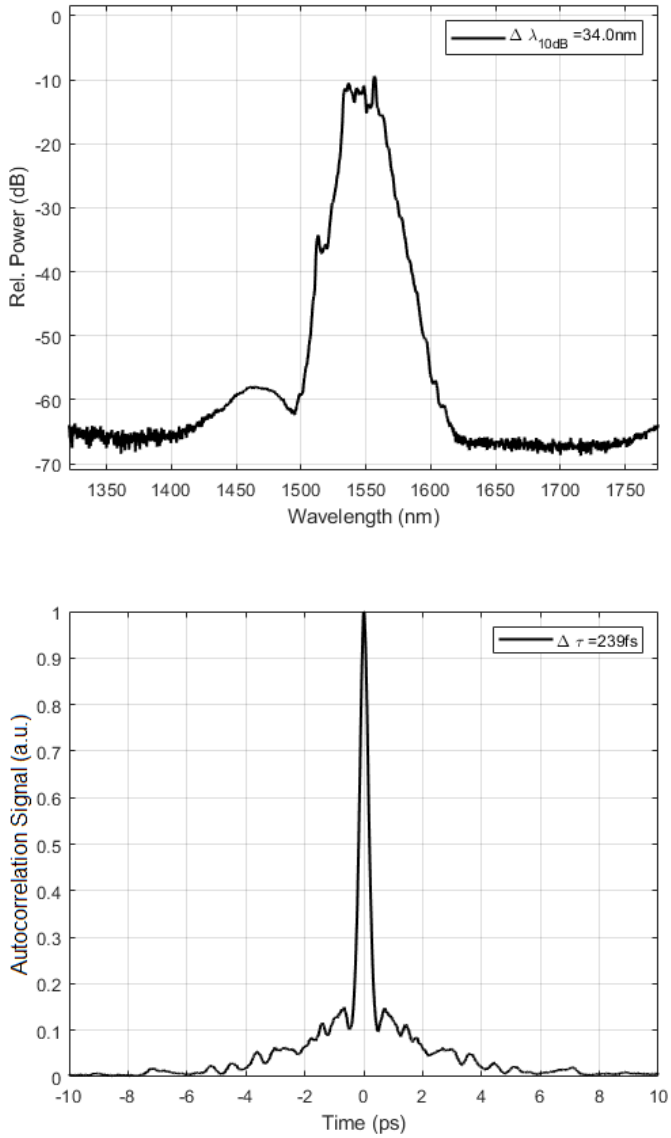

FIGURE 4.12: Compressor output optical spectrum (top) and and autocorrelation trace (bottom).

4.3 Laser Pulse Management Module (LPM)

This stage allows selecting the energy of the pulses (from less than 10 pJ to more than 10 nJ measured at the output of the system), selecting the pulse repetition rate of the laser source and arbitrarily commuting the emission of the laser at a response time of $\sim$ 1 ms. It is composed of four main elements: first, a pulse picker is included to arbitrarily select the repetition rate of the equipment from 8.2 MHz to single shot. It is based in the switching effect of an acousto-optic modulator, of a high cutoff frequency (> 10 MHz) and rise / fall times ($10 - 90\%$) < 80 ns. Time referenced to a TTL sync signal, the acousto-optic modulator down-converts the fundamental repetition frequency of the pulse train to sub-multiple frequencies of the fundamental one. Second, a variable neutral density filter with an optical density between 0 and 4.0 is used to vary the energy of the pulses. The automatic selection of the pulse energy is carried out through a motorized electromechanical enclosure. Third, a highly sensitive InGaAs photodiode is incorporated as a monitor. Its function is to convert part of the optical beam into an electrical signal to provide pulse count, reading of energy and peak power of the pulses in real time. Last, an electromechanical shutter with a response time of < 1 ms to close and open the output of the laser beam is included. Shuttering or opening is performed automatically in synchronous reference with the optical pulse train. A scheme of the pulse management module is shown in figure 4.13.

The properties of the pulse through the different stages of the LPS and LPM are shown in table 4.3. The resulting pulse meets optimal spectrum, dispersion, and duration conditions for the operation of the dispersion management module.

The power stability at room temperature of the signal at the output of the complete system has been analyzed, measuring its value every five seconds during 15 hours. A standard deviation of 0.352 % is obtained, which is below the targeted stability (1 % standard deviation) for reliable TPA-TCT. The output power stability measurement is shown in figure 4.14.

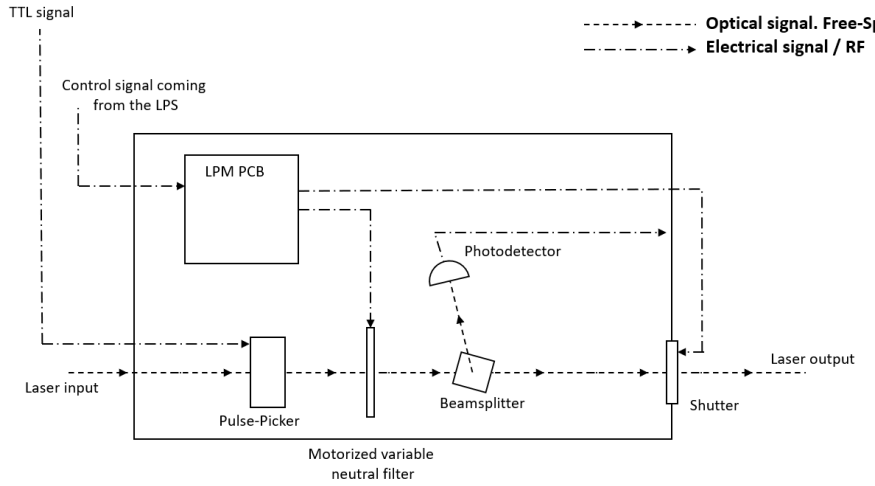

FIGURE 4.13: Pulse Management Module internal structure.

Stage	E_p **(nJ)**	f **(MHz)**	P_{avg} **(mW)**	$\Delta\tau$ **(ps)**	$\Delta\lambda$ **(nm)**
Seed	1.54	8.2	12.6	0.219	20.4
Stretcher	0.61	8.2	5.0	51.7	40.0
Preamplifier	3.48	8.2	28.6	53.6	29.0
Amplifier	150.0	8.2	1230.0	51.4	40.1
Compressor	30.7	8.2	252.0	0.239	34.0
LPM	10.98-0.02	8.2-one shot	90.0 to 0.09	0.300-0.600	34.0

TABLE 4.3: Pulse main properties along the different stages of the system

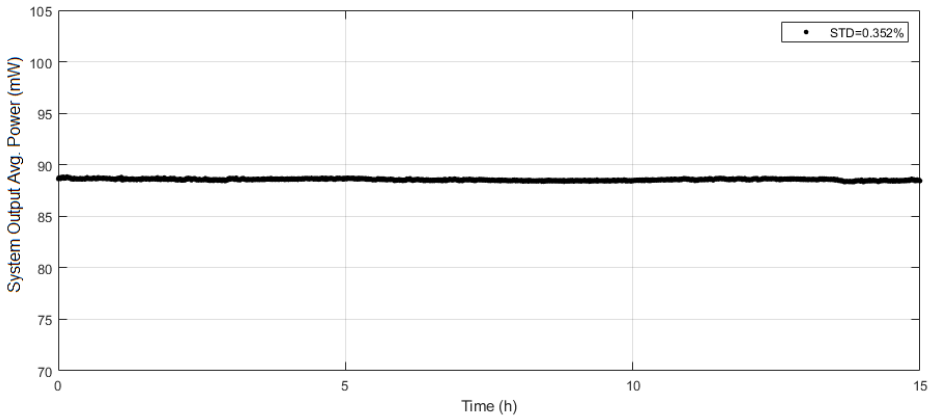

FIGURE 4.14: Average power of the output of the complete system as function of time, at room temperature.

The photodetector inside the pulse management module provides a real-time electric replica of the output of the laser system. As illustrated in figure 4.15, the detected signal provides information on the repetition rate once the signal has passed through the pulse picker.

The shutter offers a fast response of less than 2 ms. Figure 4.16 shows the shutter control signal and the pulse train detected at its output. When the control signal goes from 5 V to 0 V, the shutter is commanded to shut. Since the response time is less than 2 ms, it blocks completely the pulse train of 500 Hz repetition rate. The shutting command is synchronized with a reference signal inside the pulsed laser source so the control signal goes from 0 to 5 V just after a pulse passing thorough, so there is no possibility of half pulse passing the shutter window as long as the period of the pulsed signal is > 2 ms.

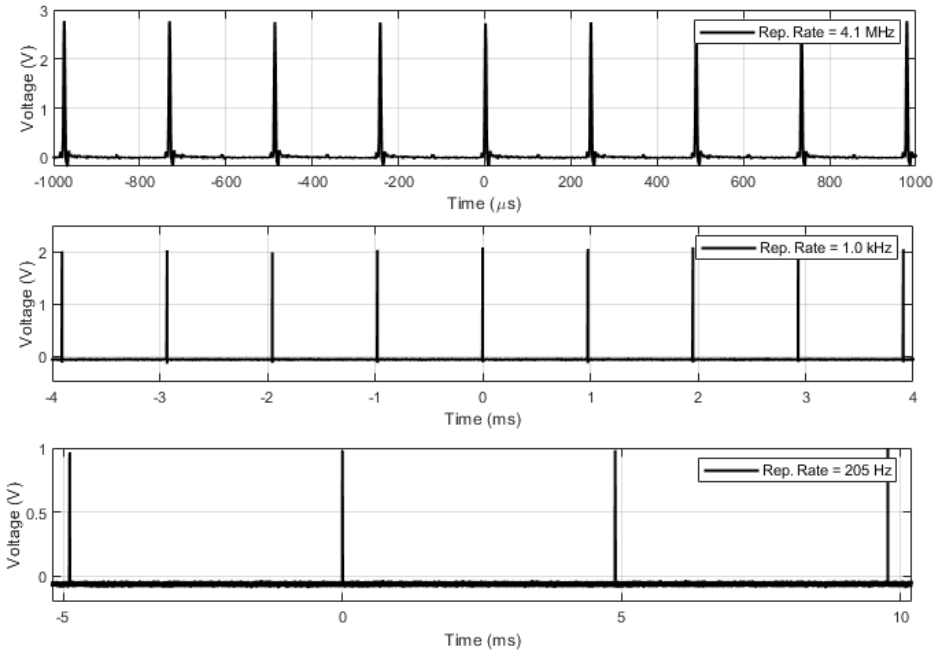

FIGURE 4.15: Oscilloscope traces of the photodetected signal at the output of the laser system at different repetition rates achieved using the pulse picker. Top: pulse picker dividing the laser repetition rate by 2. Mid: pulse picker dividing the laser repetition rate by 8200. Bottom: pulse picker dividing the repetition rate by 40000.

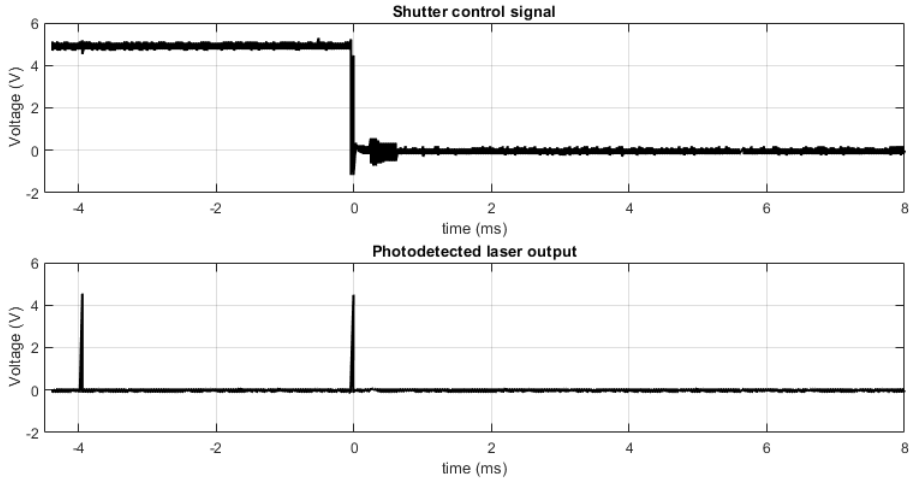

FIGURE 4.16: Oscilloscope traces of the shutter control signal (top) and the photodetected signal at the output of the laser system (bottom).

4.4 Dispersion Management Module

This stage is designed to tune and measure the pulse duration, from 300 to 600 fs. It is composed of two elements: a free space compressor and an autocorrelator. The free space compressor designed and tailored by SPHERE Photonics works by inserting dispersion of normal type in the optical path through a high precision motor to stretch or compress the pulse duration. The transmission bandwidth of the dispersive material is large enough to not affect any other property of the pulsed signal than the pulse duration. The pulse duration is measured using a Femtochrome autocorrelator (FR-103TPM/1100). The autocorrelator is designed to perform the measurement at the sample plane, which is especially convenient since this gives the information of the pulse profile at the actual point of the semiconductor under test where the two-photon excitation happens.

To optimize the dynamic range of the compressor and achieve a dispersive match between the fiber stretcher stage, the fiber compression stage and

the free-space dispersion management module, a study of the pulse length in relation to the length of the dispersive fiber of the fiber stretcher has been made for different insertion lengths of the dispersive material of the free-space dispersion management module. Figure 4.17 shows the temporal duration of the pulse with respect to the removed length of fiber PM2000D in the stretcher.

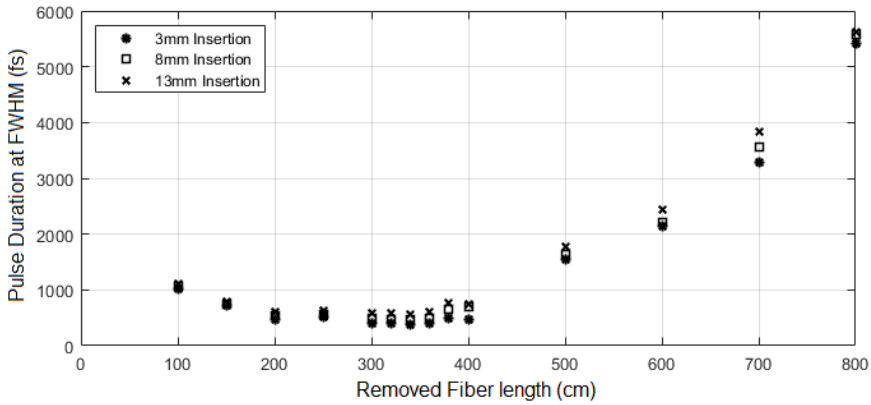

FIGURE 4.17: Pulse temporal duration vs length of PM2000D fiber removed in the stretcher from an initial value of 40 m. Asterisk: Minimum insertion length of dispersive material, 3 mm. Squares: Intermediate insertion length of dispersive material, 8 mm. Crosses: Maximum insertion length of dispersive material, 13 mm.

Taking into account the results of the study, the fiber length of the stretcher has been configured so that the duration of the pulse at the laser output is minimal. Figure 4.18 shows the autocorrelation traces obtained in the minimum configuration for different insertion lengths of the dispersive element, 3, 8 and 13 mm.

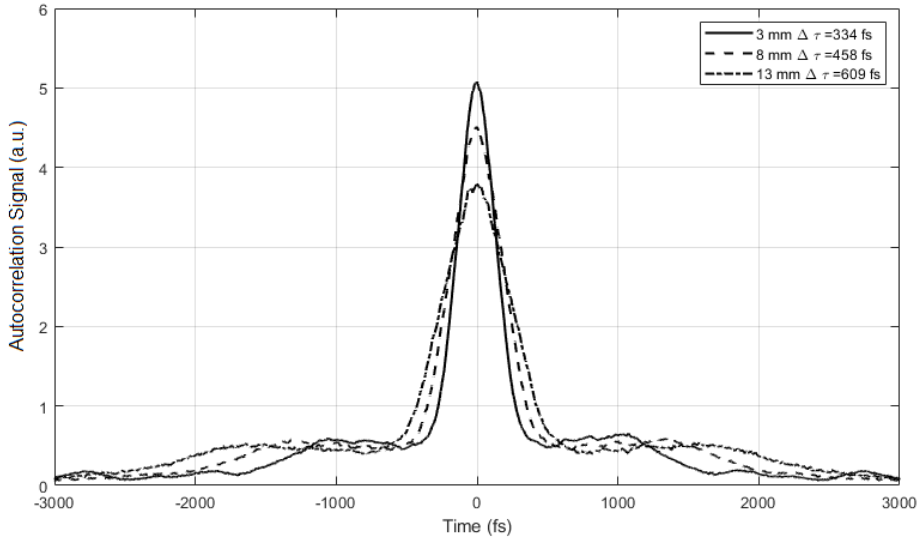

FIGURE 4.18: Autocorrelation traces of the laser output after the pulse management module for different insertion lengths of the dispersive element.

4.5 Application in TPA-TCT

One of the benefits of TPA-TCT is the true three dimensional resolution for testing silicon detectors. With conventional TCT with red, or near infrared (< 1200 nm) light, it is only possible to fully resolve the tested device by changing the illumination direction in different measurement configurations. TPA- TCT provides resolution along the beam propagation direction and thus allows for a three-dimensional scan of the device in a single measurement setup. The diagram of the measurement set up is shown in figure 4.19.

Figure 4.20 (top) shows a measurement of the charge generated in a silicon detector when irradiated with the laser source described in previous sections. The charge signal is integrated over 10 ns, as a function of the sensor position along the beam propagation direction (z-axis). The z-values are

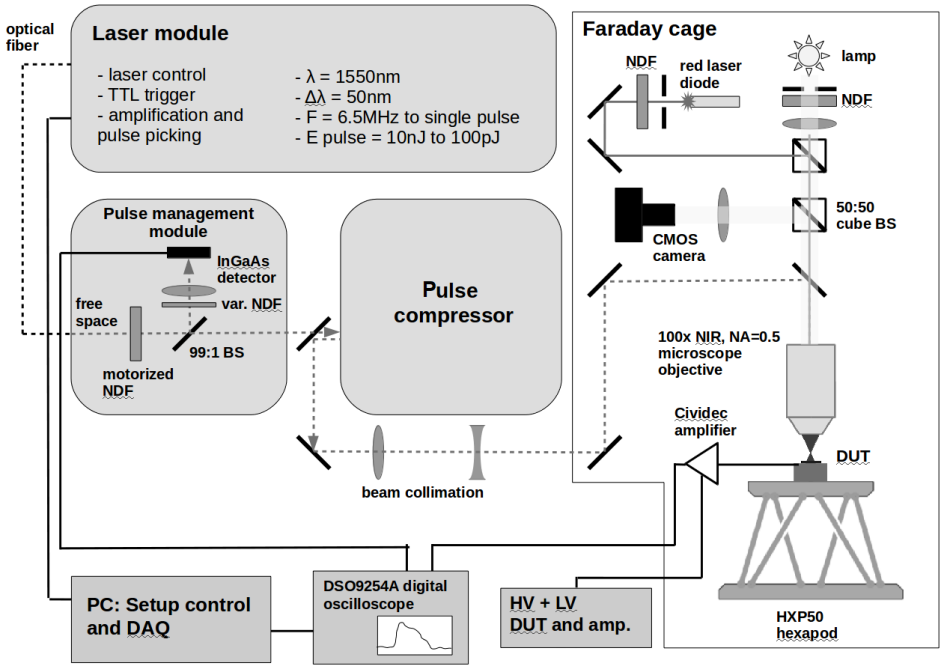

FIGURE 4.19: TPA-TCT measurement setup diagram.

corrected for the refraction of the beam due to the refractive index of silicon and the resulting shift of the position of the focal point. The zero value on the horizontal axis is arbitrarily set to the rising edge of the graph. The sensor is illuminated from the top, whereas the z-value indicates the position of the motion stage.

Therefore, moving from z = 0 to higher values, the focal point of the laser moves from the top of the device to the back side. For every recorded waveform a baseline subtraction is done. Except this, no background correction is performed. The signal vanishes quickly when the focal point of the laser beam is not inside the detector anymore. This indicates that no contribution of single photon absorption is measured. It is important to note that no resolution could be obtained in this way for conventional TCT.

The amount of charge generated by two photon absorption depends quadratically on the beam irradiance. Figure 4.20 (bottom) shows a measurement of the integrated signal as a function of the energy per laser pulse (laser power). The pulse energy is varied by changing the orientation of the neutral density filter inside the laser power management module. For this measurement a 210 microns thick silicon detector was biased at 200 V. The focal point remained at a constant position in the center of the detector. The measured values are fitted to the quadratic function $Q = p_0 P_2$. The data is compatible with a purely quadratic function, indicating again that no contribution from single photon absorption can be observed. The last three data points at high pulse energies are excluded from the fit because for these measurements an increase of the charge collection time was observed. An increase of the collection time hints at the formation of an electron-hole plasma inside the sensor. For more detailed information about these measures and their implementation, see [7].

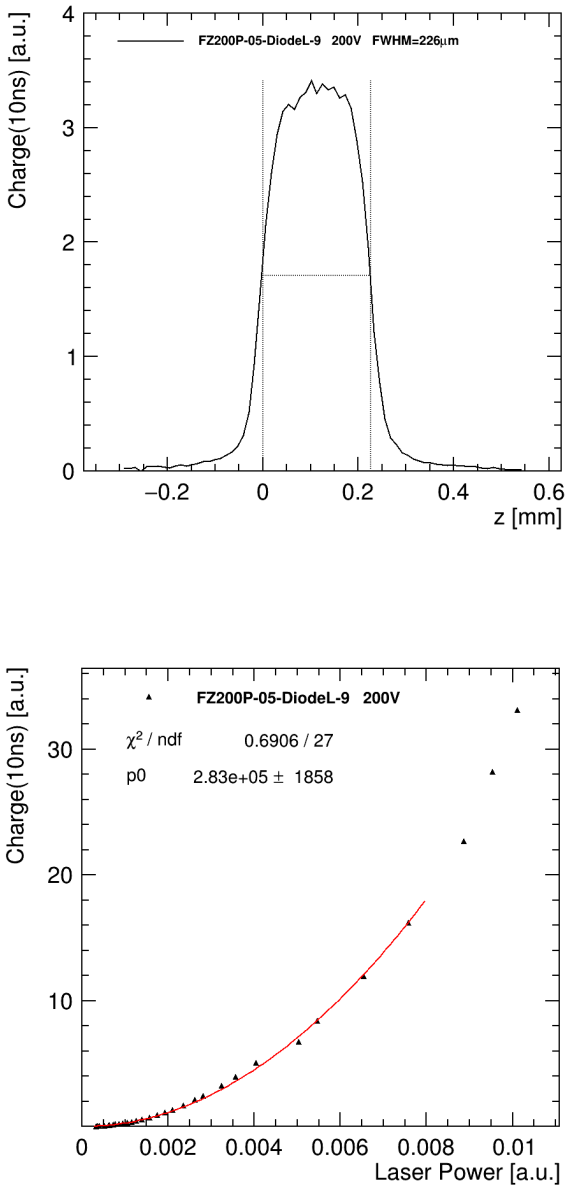

FIGURE 4.20: Signal measurement as function of the sensor position along the beam propagation direction (top). Integrated signal as function of energy per pulse (bottom).

4.6 Conclusion

The complete laser system developed in this works stem from the need of a configurable light source to be used as a scanning element in TPA-TC techniques. The pulse provided fulfills the demanding requirements to be used as a TPA generator. It is also thoroughly explained how the combination of the D-Scan and the pulse management module allows to tune the key parameters such as pulse energy, repetition rate and time pulse width.

To achieve the appropriate laser source an architecture design based on the CPA technique has been chosen in an all-fiber configuration that uses hollow core photonic crystal fibers as the compressive element. The manufacturing process has been extensively described above and the main properties that demonstrate and ensure the laser operation in the experimental framework described by this work are a central emission wavelength of 1550 nm, time pulse width of 239 fs, pulse energy above 10 nJ, fundamental repetition rate of 8.2 MHz and a standard deviation in the power average power below 1%.

Finally, the laser system was used in CERN laboratories to carry out a proof of concept of the TPA-TCT in a silicon detector, which demonstrated its viability as a light source in this novel technique.

Chapter 5

Future Work

The development and results of this thesis work raise a set of new ideas and proposals which could be carried out in the near future.

The properties of fiber lasers presented in Chapter 3 are adequate for low power applications. However, the most promising applications from the point of view of commercial prospects, such as long distance photonic communications [67, 68], optical wireless communications [9] and PADC [8], need of fiber lasers delivering higher peak power, higher average power and shorter pulses. In that sense, the concepts and techniques studied in this volume for ultra-short cavities should be extended to implement high power amplifier stages using fibers of dispersion and nonlinear coefficient allowing to broaden the spectrum and compress the pulse during the amplification process. Working in this direction, we are currently building a prototype to achieve an emitting beam with the following characteristics: 1535 nm central wavelength of emission, <100 fs pulses, > 1.0 W Average power, and > 1 GHz of repetition rate, with promising results.

To further improve telecommunication applications, it is also important to shift the central wavelength of laser emission towards longer wavelengths. Therefore, a logical next step would be to achieve an emission wavelength around 1550 nm. Due to the relationship between absorption and gain in the core of active fibers, these tend to emit at shorter wavelengths the

shorter the active fiber is. The cavities that emit naturally at gigahertz ratios are only a few centimeters long (10.34 cm at 1 GHz rep. Rate and 4.7 cm at 2.2 GHz rep. Rate) so the central wavelength of emission is shifted towards short wavelengths, in this case, 1535 nm [69]. To achieve an emission at longer wavelengths, the most direct solution is to act on the reflection function of one of the mirrors, forcing the cavity to emit at the desired wavelength. A first approximation is to use a resonant SESAM whose reflection spectrum is sharper around 1550 nm (RSAM) [70]. On the other hand, it is also possible to act on the reflectance spectru of the second mirror of the cavity, aiming a reflectance band of 1550 ± 10 nm.

Although being very versatile, the laser presented in chapter 4 can be improved in order to provide an all fiber structure and shorter pulses. This would increase its applicability to the TPA-TCT. The all fiber structure will simplify the measurement system reducing the number of optical elements between the laser output and the sample. The shorter pulses will produce an increase in the efficiency of the two photon absorption, increasing the dynamic range of the system. To achieve shorter pulses it is needed to maintain the pulse-to-pulse coherence through the stretching and amplification stages so that the pulse can be compressed down to the Fourier-transform limit. One proposal that is currently being researched at FYLA is to replace the fiber stretcher with a pair of chirped Bragg gratings [71]. In addition, these gratings can be temperature controlled to adjust the net dispersion of the system. This setting is known as TPSR (Tuneable Pulse Stretcher Reflector) [72]. This stretching stage is expected to maintain the pulse-to-pulse coherence better than the stretching produced by the PM2000D fiber. In this configuration, splices between different fibers (PM2000D spliced to PM1550-XP) are avoided and the total optical path traveled by the pulse is much shorter (40 m vs 1-2 m). In addition, the tuneability of the TPSR moves the system towards the all-fiber solution, since this configuration replaces the free space compressor and can be calibrated to achieve variations in pulse duration between 100 and 300 fs.

Another update that is being investigated to achieve a more robust system is to include a fiber pigtailed pulse-picker. This will allow to control the repetition rate of the equipment after the amplification stage and also, by modifying the power of the control RF signal, to modify the losses introduced by the pulse-picker. This results in a variation of the pulse energy at the output of the laser. These improvements will make it possible to eliminate the free space pulse management module (LPM), resulting in a more compact, robust and portable system.

Chapter 6

Publications

6.1 Publications related with this thesis work

6.1.1 Journals

[1] Héctor Muñoz-Marco, Javier Abreu-Afonso, Gaia Sardiello, and Pere Pérez-Millán. "Theoretical and experimental comprehensive study of GHz-range passively mode-locked fiber lasers". Applied Optics Vol. 59, Issue 23, pp. 6817-6827 (2020). Chosen as Editor's Pick in nº of August 2020.

[2] Moritz Wiehe , Marcos Fernández García , Michael Moll , Raúl Montero, F. R. Palomo, Ivan Vila, Héctor Muñoz-Marco, Viorel Otgon, and Pere Pérez-Millán. "Development of a Tabletop Setup for the Transient Current Technique Using Two-Photon Absorption in Silicon Particle Detectors". IEEE Transactions on Nuclear Science, Vol. 68, No. 2, February 2021.

[3] Héctor Muñoz-Marco, Moritz Wiehe, Azahara Almagro-Ruiz, Michael Moll, Raúl Montero, F.R. Palomo, Iván Vila, Marcos Fernández-García, and Pere Pérez-Millán. "1550 nm Femtosecond Fiber Laser System of Configurable Properties for the Two-Photon Excitation of Transient Current in Semiconductor Detectors". Journal of Lightwave Technologies, submitted february 2021.

6.1.2 Conference Proceedings

[1] H. Muñoz-Marco, M. Brotóns-Gisbert, V. Otgon, X. Navajas-Alba, J. Abreu-Afonso, P. Pérez-Millán. "Highly stable femtosecond laser of pulse repetition rates in the MHz and GHz range". Ultrafast Science and Technology Spain (USTS), Madrid (Spain) November 2015

[2] H. Muñoz-Marco, V. Otgon, X. Navajas-Alba, S. Torres-Peiró, J. Abreu-Afonso, P. Pérez-Millán. "Short and long-term highly stable 1GHz fiber laser comb". COST International Training School on Fiber Lasers and Optical Fiber Technology. Prague, (Czech Republic). August 2016

[3] P. Pérez-Millán, J. Abreu-Afonso, S. Torres-Peiró, V. Otgon, H. Muñoz-Marco, J. Pérez-Vizcaíno. "Industrialization of Ultrafast Optical Fiber Lasers".Ultrafast Science and Technology Spain (USTS). Salamanca (Spain). November 2017

[4] Héctor Muñoz-Marco, Javier Abreu-Afonso, Pere Pérez-Millén. "1GHz All-Fiber Laser Frequency Comb". International Conference in Advanced Optoelectronics and Lasers (CAOL), Sozopol, (Bulgaria). September 2019

6.1.3 Patents

[1] "A Mode-Locked Fiber laser System". EP17382560.5. US2020/0235546. Priority date: 08/08/2017

6.2 Other Publications

6.2.1 Journals

[1] Jean-Christophe Delagnes, Romain Royon, Jérôme Lhermite, Giorgio Santarelli, Héctor Muñoz-Marco, Dia Darwich, Romain Dauliat, Raphael Jamier, Philippe Roy and Eric Cormier. "High-power, widely tunable ps source in the visible based on four wave mixing in optimized photonic crystal fibers.". Optics Express Vol. 26, Issue 9, pp. 11265-11275 (2018)

[2] Paul Robert, Coralie Fourcade-Dutin, Romain Dauliat, Raphael Jamier, Hector Muñoz-Marco, Pere Pérez-Millán, John M. Dudley, Philippe Roy, Hervé Maillotte, and Damien Bigourd. "Spectral correlation of four-wave mixing generated in a photonic crystal fiber pumped by a chirped pulse". Optics Letters Vol. 45, Issue 15, pp. 4148-4151 August (2020)

[3] Benjamín Alonso, Salvador Torres-Peiró, Rosa Romero, Paulo T. Guerreiro, Azahara Almagro-Ruiz, Héctor Muñoz-Marco, Pere Pérez-Millán and Helder Crespo. "Detection and elimination of pulse train instabilities in broadband fibre lasers using dispersion scan". Scientific Reports, No. 10, Article number: 7242. April 2020.

6.2.2 Conference Proceedings

[1] V. Otgon, H. Muñoz-Marco, S. Torres-Peiró, X. Navajas-Alba, J. Abreu-Afonso, P. Pérez-Millán. "Fiber Lasers. Focused on Customer R+D Needs and Perspectives". COST MP1401 Annual Conference and 2nd MC meeting, Zadar (Croatia), April 2016

[2] V. Otgon, H. Muñoz-Marco, S. Torres-Peiró, X. Navajas-Alba, J. Abreu-Afonso, P. Pérez-Millán. "Láseres de Fibra Óptica. I+D Enfocado a las Perspectivas y Necesidades del Cliente Industrial". 5º Congreso de Óptica Aplicada. Yuriria (México). June 2016

[3] V. Otgon, X. Navajas-Alba, H. Muñoz-Marco, S. Torres-Peiró, J. Abreu-Afonso, P.Pérez-Millán. "Arbitrary Filtering Module Applied To A Supercontinuum Fiber Laser". COST International Training School on Fiber Lasers and Optical Fiber Technology. Prague, (Czech Republic). August 2016

[4] P. Pérez-Millán, J. Abreu-Afonso, S. Torres-Peiró, V.Otgon, H. Muñoz-Marco. "Supercontinuum Based Solutions Focused On Industrial Customer Needs". ICTON. Girona (Spain). July 2017

[5] H. Muñoz-Marco, J. Abreu-Afonso, V.Otgon, R. Dauliat, R. Jamier, P. Roy, P. Pérez-Millán. “Synchronus Interferometric Measurement of Dispersion Applied to Customization Of Supercontinuum Sources”. IWG2 COST Technical Meeting. Vienna (Austria). February 2018

[6] H. Muñoz-Marco, J. Abreu-Afonso, V. Otgon, R. Dauliat, R. Jamier, P. Roy, P. Pérez- Millán. “Synchronous interferometric broadband measurement of dispersion applied to manufacturing optimization of microstructured optical fibers”. SPIE Photonics Europe. Strasbourg (France). April 2018

[7] Benjamín Alonso, s. Torres-Peiro, Rosa Romero, Paulo Tiago Guerreiro, Azahara Almagro, Héctor Muñoz-Marco, Pere Pérez-Millán and Helder Crespo. "Detecting and quantifying pulse train instabilities with self-calibrating d-scan". Frontiers in Optics, Washington, D.C., United States, January 2020

[8] Coralie Fourcade-Dutin, Paul Robert, Romain Dauliat, Raphael Jamier, Héctor Muñoz-Marco, Pere Pérez-Millán, John M. Dudley, H. Maillotte, Philippe Roy and Damien Bigourd. "Spectral Distributions of Chirped Pulsed Four-Wave Mixing in a Photonic Crystal Fiber Measured by Dispersive Fourier Transform Method". Osa Nonlinear Photonics, Washington, DC, United States, July 2020

[9] Benjamín Alonso, S. Torres-Peiro, Rosa Romero, Paulo Tiago Guerreiro, Azahara Almagro, Héctor Muñoz-Marco, Pere Pérez-Millán and Helder Crespo. "Experimental quantification of pulse train instabilities using dispersion scan". International Conference on Ultrafast Phenomena, Washington, D.C., United States, November 2020

[10] Azahara Almagro-Ruiz, Salvador Torres-Peiró, Héctor Muñoz-Marco, Romain Dauliat, Raphael Jamier, Rosa Romero, Paulo T. Guerreiro, Marina Cunquero, Gustavo Castro, Pablo Loza-Álvarez, Helder Crespo, Philippe Roy, Pere Pérez-Millán. "Few-cycle all-fiber temporally coherent supercontinuum sources". Photonic West, Online, March 2021

6.2.3 Patents

[1] "Light Inspection System And Method of The Surface And Inside Of A Sample".US16/622.456, EP3324173131. Priority date: 03/07/2017

[2] "An all-fiber configuration system and method for generating temporally coherent supercontinuum pulsed emission". US2020/0343681, JP2020-75909, EP19382313.5. Priority date: 25/04/2019

Bibliography

1. Thomsen, C. L., Madsen, D., Keiding, S. R., Thøgersen, J. & Christiansen, O. Two-photon dissociation and ionization of liquid water studied by femtosecond transient absorption spectroscopy. *J. Chem. Phys.* **110** (1999).
2. Udem, T., Holzwarth, R. & Hansch, T. W. Optical frequency metrology. *Nature* (2002).
3. Jepsen, P. U., Jacobsen, R. H. & Keiding, S. R. Generation and detection of terahertz pulses from biased semiconductor antennas. *Journal Optical Society of America B* **13** (1996).
4. Paulsen, H. N., Hilligsøe, K. M., Thøgersen, J., Keiding, S. R. & Larsen, J. J. Coherent anti-Stokes Raman scattering microscopy with a photonic crystal fiber based light source. *Optics letters* **28** (2003).
5. Hartl, I. *et al.* Ultrahigh resolution optical coherence tomography using continuum generation in a air-silica microstructure optical fiber. *Optics letters* **26** (2001).
6. Fernández-García, M. *et al.* High resolution 3D characterization of silicon detectors using a Two Photon Absorption Transient Current Technique. *Nuclear Instruments and Methods in Physics Research A* (Sept. 2019).
7. Wiehe, M. *et al.* Development of a Tabletop Setup for the Transient Current Technique Using Two Photon Absorption in Silicon Particle Detectors. *IEEE Transactions on Nuclear Science* (Dec. 2020).
8. Valley, G. C. Photonic analog-to-digital converters. *Opt. Exp.* **15,** 1955–1982 (Mar. 2007).

9. Hirata, A. *et al.* 120-GHz-band millimeter-wave photonic wireless link for 10-Gb/s data transmission. *IEEE Transactions on Microwave Theory and Techniques* **54** (May 2006).
10. Yao, J., Zeng, F. & Wang, Q. Photonic generation of ultrawideband signals. *Journal of Lightwave Technologies* **25** (Nov. 2007).
11. Weigl, P., Kasenbacher, A. & Werelius., K. Dental applications. *Top. Applied Physics* **96** (2004).
12. Tünnermann, A., Limpert, J. & Nolte, S. Ultrashort pulse fiber lasers and amplifiers. *Top. Applied Physics* **96** (2004).
13. Breitling, D., Föhl, C., Dausinger, F., Kononenko, T. & Konov, V. Drilling of metals. *Top. Applied Physics* **96** (2004).
14. Tünnermann, A. *et al.* The renaissance and bright future of fibre lasers. *Journal of Physics B* **38** (2005).
15. Limpert, J., Röser, F., Schreiber, T. & Tunnermann, A. High-Power Ultrafast Fiber Laser Systems. *IEEE J. Selected Top. in Quantum Electron* **12** (2006).
16. Digonnet, M. J. F. *Rare-Earth-Doped Fiber Lasers and Amplifiers. Revised and Expanded* 1st ed. (CRC Press, 2001).
17. Fermann, M. E., Galvanauskas, A., Sucha, G. & Harter, D. Fiber-lasers for ultrafast optics. *Applied Physics B* **65** (1997).
18. Nelson, L. E., Jones, D. J., Tamura, K., Haus, H. A. & Ippen, E. P. Ultrashort-pulse fiber ring lasers. *Applied Physics B* **65** (1997).
19. Haus, H. A. Mode-Locking of Lasers. *IEEE Journal Selected Top. in Quantum Electron* **6** (2000).
20. Laghezza, F., Scotti, F., Ghelfi, P., Bogoni, A. & Pina, S. Jitter-limited photonic analog-to-digital converter with 7 effective bits for wideband radar applications. *Proc. Radar Conf.,* 1–5 (2013).
21. Gherman, T. & Romanini, D. Mode-locked cavity-enhanced absorption spectroscopy. *Optics Express* **10,** 1033–1041 (Sept. 2002).
22. Liu, X., Lægsgaard, J. & Turchinovich, D. Monolithic highly-stable femtosecond fiber lasers for applications in biophotonics. *IEEE J. Sel. Topics Quantum Electron* **18,** 1439–1450 (July 2012).

23. Unruh, J. R. *et al.* Two-photon microscopy with wavelength switchable fiber laser excitation. *Optics Express* **14,** 9825–9831 (Oct. 2006).
24. Lee, Y. M., Tu, R. Y., Chiang, A. C. & Huang, Y. C. Average-power mediated ultrafast laser osteotomy using a mode-locked Nd:YVO4 laser oscillator. *J. Biomed. Opt.* **12,** 060505 (Nov. 2007).
25. Ogusu, M., Inagaki, K., Ohira, T., Ogura, I. & H.Yokoyama. Wavelengthdivision multiplexing of two-mode injection-locked Fabry–Prot lasers using optically harmonic modelocked master laser. *Electron. Lett* **37,** 889–890 (July 2001).
26. Oehler, A. E. H., Zeller, S. C., Weingarten, K. J. & Keller, U. "Broad multiwavelength source with 50 GHz channel spacing for wavelength division multiplexing applications in the telecom C band. *Opt. Lett.* **33,** 2158–2160 (Sept. 2008).
27. Auston, D. H. Picosecond optoelectronic switching and gating in silicon. *Appl. Phys. Lett.,* 101–103 (1975).
28. Lawton, R. A. & Andrews, J. R. Optically strobed sampling oscilloscopes. *IEEE Trans. Instrum. Meas.,* 56–60 (Mar. 1976).
29. Low, A. J. & Carroll, J. E. 10ps optoelectronic sampling systems. *Solid-State and Electron Devices,* 185–190 (1978).
30. Leonberger, F. J. & Moulton, P. High-speed InP optoelectronic switch. *Appl. Phys.,* 712–714 (1979).
31. III, C. H. C., Diadiuk, V., Yao, I., Leonberger, F. J. & Williamson, R. C. InP optoelectronic switches and their high-speed signal-processing applications. *Proc. SPIE,* 164–168 (1983).
32. Byunand, H. *et al.* Compact, stable 1 GHz femtosecond Er-doped fiber lasers. *Appl. Opt.* **49,** 5577–5582 (Oct. 2010).
33. Martinez, A. & Yamashita, S. Multi-gigahertz repetition rate passively modelocked fiber lasers using carbon nanotubes. *Opt.Exp.* **19,** 6155–6163 (Mar. 2011).
34. Sobon, G., Sotor, J. & Abramski, K. M. All-polarization maintaining femtosecond Er-doped fiber laser mode-locked by Graphene saturable absorbers. *Laser Phys. Lett.* **9,** 581–586 (May 2012).

35. He, W., Pang, M. & Russel, P. S. Wideband-tunable soliton fiber laser modelocked at 1.88 GHz byoptoacoustic interactions in solid-core PCF. *Optics Express* **23** (Sept. 2015).
36. Thapa, R., Nguyen, D., Zong, J. & Chavez-Pirson, A. All-fiber fundamentally mode-locked 12 GHz laser oscillator based on an Er/Yb-doped phosphate glass fiber. *Optics Letters* **39,** 1418–1421 (Mar. 2014).
37. Bates, A. G. & Moll, M. A comparison between irradiated magnetic Czochralski and Float Zone silicon detectors using transient current technique. *Nuclear Instruments and Methods in Physics Research A,* 113–124 (Dec. 2005).
38. Eremin, V., Strokan, N., Verbitskaya, E. & Li, Z. Development of transient current and charge techniques for the measurement of effective net concentration of ionized charges (neff) in the space charge region of p-n junction detectors. *Nuclear Instruments and Methods in Physics Research A,* 388–398 (1996).
39. Kramberger, G., Cindro, V., Mandic, I., Mikuz, M. & Zavrtanik, M. Determination of effective trapping times for electrons and holes in irradiated silicon. *Nuclear Instruments and Methods in Physics Research A,* 645–651 (2002).
40. Fink, J. *et al.* TCT characterization of different semiconductor materials for particle detection. *Nuclear Instruments and Methods in Physics Research A,* 227–233 (2006).
41. DeSalvo, R., Said, A. A., Hagan, D. J., Stryland, E. W. V. & Sheik-Bahae, M. Infrared to Ultraviolet Measurements of Two-Photon Absorption and n2 in Wide Bandgap Solids. *IEEE Journal of quantum electronics* **32** (Aug. 1996).
42. Mihaly, H. From NASA to EU: the evolution of the TRL scale in Public Sector Innovation. *The Innovation Journal* (Sept. 2017).
43. Griffiths, D. J. *Introduction to electrodynamics* 4th ed. (Cambridge University Press, 2017).
44. Agrawal, G. P. *Nonlinear Fiber Optics* 4th ed. (Academic, 2007).
45. Millioni, P. & Eberly, J. *Lasers* (Wiley, 1988).

46. Hönninger, C., Paschotta, R., Morier-Genoud, F., M.Moser & U.Keller. Q-switching stability limits of continuous-wave passive mode locking. *IEEE J. Selected Top. In Quantum Electron* **16** (1999).
47. Kärtner, F. X., der Au, J. A. & Keller, U. Mode-Locking with Slow and Fast Saturable Absorbers - What's the Difference? *IEEE J. Selected Top. In Quantum Electron.,* 159–168 (1998).
48. Keller, U. *et al.* Semiconductor Saturable Absorber Mirrors (SESAM's) for Femtosecond and Nanosecond Pulse Generation in Solid-State Lasers. *IEEE J. Quantum Electron.,* 435–445 (1993).
49. Brovelli, L. R. & Keller, U. Design and operation of antiresonant Fabry-Perot saturable semiconductor absorbers for mode-locked solidstate lasers. *J. Opt. Soc. Am. B,* 311–322 (1995).
50. Hönninger andC., R. P., Morier-Genoud, F., Moser, M. & Keller, U. Q-switching stability limits of continuous-wave passive mode locking. *J. Opt. Soc. Am. B,* 46–56 (1999).
51. Philipps, J., T.Töpfer, H.Ebendorff-Heidepriem & D.Ehrt, R. Energy transfer and upconversion in erbium-ytterbium doped fluoride phosphate glasses. *Applied Photonics B,* 233–236 (2002).
52. Brotons-Gisbert, M. *et al.* Comprehensive Theoretical and Experimental Study of Short- and Long-Term Stability in a Passively mode-locked Solitonic Fiber Laser. *Journal of Lightwave Technology* (2015).
53. Kiritchenko, N. V. *et al.* Effect of ytterbium co-doping on erbium clustering in silica-doped glass. *Laser Physics* (Jan. 2015).
54. Villanueva, G. E., Ferri, M. & Pérez-Millán, P. Active and passive mode-locked fiber lasers for high-speed high-resolution photonic analog to digital conversion. *IEEE J. Quantum Electron.* **48,** 1443–1452 (Nov. 2012).
55. Mayer, A., Phillips, C. & Keller, U. Watt-level 10-gigahertz solid-state laser enabled by self-defocusing nonlinearities in an aperiodically poled crystal. *Nature Communications* (Nov. 2017).
56. Domingo, J. M. S., Pelayo, J., Villuendas, F., Heras, C. D. & Pellejer, E. Very high resolution optical spectrometry by stimulated Brillouin scattering. *IEEE Photonics Technol. Lett.* **17,** 855–857 (2005).

57. Maine, P., Strickland, D., Bado, P. & Pessot, M. Generation of Ultrahigh Peak Power Pulses by Chirped Pulse Amplification. *IEEE Journal of quantum electronics* **24** (Feb. 1988).
58. Strickland, D. & Mourou, G. Compression of amplified chirped optical pulses. *Optics Communications* **56** (Dec. 1985).
59. Sinkin, O. V., Zweck, J. & Menyuk, C. R. Optimization of the Split-Step Fourier Method in Modeling Optical-Fiber Communications Systems. *Journal of lightwave technology* **21** (Jan. 2003).
60. Galvanauskas, A. Mode-Scalable Fiber-Based Chirped Pulse Amplification Systems. *IEEE Journal on selected topics in quantum electronics* **7** (Aug. 2001).
61. De Matos, C. J. S., Kennedy, R. E., Popov, S. & Taylor, J. R. 20-kW peak power all-fiber 1.57-mm source based on compression in air-core photonic bandgap fiber, its frequency doubling, and broadband generation from 430 to 1450 nm. *Optics Express* **30** (Feb. 2005).
62. Shibata, N., Tateda, M., Seikai, S. & Uchida, N. WAVELENGTH DEPENDENCE OF POLARISATION MODE DISPERSION IN ELLIPTICAL-CORE SINGLE-MODE FIBRES. *Electronics Letters* **17** (Aug. 1981).
63. Okamoto, K. & Hosaka, T. Polarization-dependent chromatic dispersion in birefringent optical fibers. *Optics Letters* **12** (Apr. 1987).
64. Tzolov, V. P. & Fontaine, M. Theoretical analysis of birefringence and forminduced polarization mode dispersion in birefringent optical fibers: A fullvectorial approach. *Journal of Applied Physics* **77** (Jan. 1995).
65. Imeshev, G., Hartl, I. & Fermann, M. An optimized Er gain band all-fiber chirped pulse amplification system. *Optics Express* **12** (Dec. 2004).
66. Herda, R. *et al.* Environmentally Stable Mode-Locked Fiber Laser With Dispersion Compensation by Index-Guided Photonic Crystal Fiber. *IEEE Photonic Technology LettersS* **20** (Feb. 2008).
67. Capmany, J. *et al.* Microwave Photonic Signal Processing. *Journal of Lightwave Technologies* **31** (Feb. 2013).
68. Clark, J. & Lanzani, G. Organic photonics for communications. *Nature Photonics* **4** (July 2010).

69. Cho, Y. G. *et al.* Emission properties of the Er3+: I-4(11/2) -> I-4(13/2) transition in Er3+- and Er3+/Tm3+-doped Ge-Ga-As-S glasses. *Journal of non-crystalline solids* **278** (Dec. 2000).
70. Griebner, U., Richter, W. & Steinmeyer, G. Resonant saturable absorber mirrors for dispersion control in ultrafast lasers. *IEEE journal of quantum electronics* **43** (Feb. 2007).
71. Michailovas, A., Rusteika, N., Smirnov, V. & Vasilyeu, R. Efficient Ultrafast Fiber Laser Using Chirped Fiber Bragg Grating And Chirped Volume Bragg Grating Stretcher/Compressor Configuration. *COMPONENTS AND PACKAGING FOR LASER SYSTEMS II* **9730** (2016).
72. Zhi, Y., Qianglong, L., Feng, L. & Xiaojun, Y. Pulse duration tunable fiber CPA system based on thermally dispersion tuning of chirped fiber bragg grating. *Optik* **127** (2016).

List of Figures

List of Tables